Fabrication and Characterization of Nanostructured Oxides for Energy Storage

Qian Chen

A dissertation
submitted in partial fulfillment of the
requirements for the degree of

Doctor of Philosophy

University of Washington
2014

Reading Committee:
Jiangyu Li, Chair
Mark E. Tuttle
Stuart B. Adler

Program Authorized to Offer Degree:
Mechanical Engineering

University of Washington

Abstract

Fabrication and Characterization of Nanostructured Oxides for Energy Storage

Qian Chen

Chair of the Supervisory Committee:

Professor Jiangyu Li

Mechanical Engineering

Materials for energy storage have become increasingly important in the modern world as alternatives to petrochemical energy sources. Although technology such as lithium-ion batteries and solid oxide fuel cells are in commercial use, improvements must still be made to increase widespread adoption. To this end, nanostructured materials have emerged as potentially impactful solutions, as they can greatly improve the performance of the energy storage device. One goal of this dissertation was to fabricate nanostructured materials through solution-based processing, electrospinning, and controlled annealing for lithium-ion battery electrodes. This project resulted in the formation of porous fibers from inexpensive, nontoxic materials that can be used as high capacity electrodes. Another component of this dissertation was to deposit thin film noble metals and metal oxides via sputtering for metal-air battery cathodes. The results from these experiments indicate that nanostructured thin films could have improved catalytic activity compared to polycrystalline bulk structures, and also were lower cost due to the decrease in material used.

The other major portion of this dissertation was to study the fundamental behavior of nanostructured materials for energy storage at a localized level using electrochemical strain microscopy, a technique that is still in its infancy. The measured responses using electrochemical strain microscopy tended to be difficult to interpret, as they contained many different chemical and mechanical contributions. A series of experiments were devised to distinguish among the different mechanisms, comparing differing responses from Vegard strain, ferroelectric behavior, and electrostrictive effects. Given this framework, inhomogeneous lithium iron phosphate was characterized using electrochemical strain microscopy. From these results, it was found that nanocrystalline particles had higher lithium ion diffusivity as compared to microcrystalline particles, which correlates with macroscopic electrochemical performance. Furthermore, this technique could be applied to measure local lithium ion concentration in samples at different states of charge. Electrochemical strain microscopy was also applied to study samarium doped ceria, a solid oxide fuel cell electrolyte. In this case, the measured behavior was found to be due to the motion of small polarons, supporting the space-charge model of mixed ionic and electronic conductivity in nanostructured electrolytes. Electrochemical strain microscopy was found to be a strong and versatile technique that can fundamentally characterize local behavior of ions, vacancies, electrons, and holes in an energy storage material, and can guide future research in this area.

Acknowledgments

I would like to thank first and foremost my family for their support over the years.

I would like to thank the members of the multifunctional materials lab for their help in my research, and for providing mental and emotional support over the past few years.

I'd like to convey my gratitude to my advisor, Jiangyu Li, for all of his advice over the years, and to my committee, Mark Tuttle, Stuart Adler, and Guozhong Cao for teaching me elements of their expertise, and for their time in reading and evaluating my work.

I'd also like to thank the group from AERB third floor for many of the moments of intentional and unintentional hilarity over the past few years, and for providing much needed breaks from research.

To the researchers at JPL, especially Andrew Kindler, I thank for sharing their expertise in electrochemistry and the Ph.D. process. From them I've learn more in a few conversations than I could have in hours of reading about electrochemistry, and about life philosophy.

I'd also like to acknowledge the support of NASA Office of the Chief Technologist's Space Technology Research Fellowship NNX11AN45H.

Table of Contents

Chapter 1 Introduction

Chapter 2 Synthesis of $LiFePO_4$ Fibers through Electrospinning

Chapter 3 Electrochemical Strain Microscopy: Distinguishing Mechanisms

Chapter 4 Electrochemical Strain Microscopy of $LiFePO_4$

Chapter 5 Electrochemical strain microscopy of doped ceria as an electrolyte for solid oxide fuel cells

Chapter 6 Deposition and Characterization of Cathode Catalysts for Metal-Air Batteries

Chapter 7 Conclusions and Future Work

Table of Figures

1 Introduction

1.1 Motivation

In this modern and highly power consuming world, the demand for energy storage systems continues to increase. This demand requires energy storage solutions that can fulfill a wide variety of different applications, ranging from small batteries in consumer electronics to large systems for grid storage. For each of these applications, the current energy storage technology leaves much to be desired. In consumer electronics, batteries are often seen as the heaviest, costliest, and least environmentally-friendly component [1]. In order to reduce the weight and volume of consumer devices, increasing the energy and power densities of batteries is crucial. As renewable power sources become of more interest as petroleum prices increase, the development of grid-level storage and regulation also becomes a priority. Here, the requirements for energy storage focus more on price and long cycle lives rather than on density [2], allowing for the possibility of low power systems [3, 4]. Energy storage solutions are also being sought for electric and hybrid electric vehicles to alleviate the demand for fossil fuels in transportation and reduce environmental pollution. For that application, the emphasis is on reliable batteries that have high energy and power densities and long cycle lives [5, 6]. Although lithium-ion and nickel-metal hydride batteries are used today in commercially sold vehicles, their performance and cost, along with safety concerns, are considered significant limitations to wider adoption of electric vehicles [7-9].

Energy storage systems are not only necessary on this world, but are also crucial for the future of space exploration. Many functions on spacecraft and on the International Space Station depend solely on electrical energy to power its lights, run life-support systems, energize its computers, and conduct scientific studies [10]. Fuel cells based on hydrogen have been utilized in a variety of space applications, particularly in space shuttles, and can be combined in the future with solar cells to convert water to hydrogen and oxygen and back again to water to serve as a safe and plentiful energy source. In recent years, thermoelectric devices have been used to generate renewable energy for use in the Mars Rovers, but power generated by these elements must be regulated and stored for long-term use. In space applications, batteries must not only fulfill the terrestrial requirements of high energy density and long cycle life, but also must be tolerant of temperatures ranging from -40°C to 40°C, and be resistant to radiation damage [11-13]. Improvements in energy storage would increase the lifetimes of spacecraft and enable a wider reach for space exploration.

In order to meet the goals for such a wide variety of applications, many different forms of energy storage solutions have to be developed. These solutions require improving the current state-of-the-art batteries and fuel cells and also developing thus far uncommercialized metal-air systems. There is no expectation of a one size fits all solution to these diverse applications, but in all of these technologies, the adoption of nanostructured material architectures has the potential to transform the field [14]. Nanostructured materials, due to the greater influence of surface effects, have unique mechanical and electrical properties not found in bulk [15]. For lithium-ion batteries, nanostructured electrode materials allow for reactions that cannot occur in the bulk and can accommodate lithium ion intercalation without mechanical degradation [16, 17]. In addition, the distances that electrons and ions must travel decrease in nanostructured materials, leading to faster transport rates, and thereby, potentially faster charging and discharging. Nanostructured materials are also important as catalysts and electrolytes in fuel cells and metal-air batteries [15]. For many fuel cell and metal-air systems, platinum-based catalysts are used to facilitate the oxygen reduction reaction. Dispersing nano-sized platinum or platinum alloy particles onto nanostructured carbon can increase the catalytic activity while reducing the amount of expensive elements used [18, 19]. In these systems, the electrolyte, a solid ion conductor, can also be enhanced by turning toward nanostructured materials for its components [20]. The ionic conductivity of nanostructured electrolytes can be markedly higher compared to their bulk counterparts, due to changes in defect chemistry and conductivities at grain boundaries and surfaces compared to that of the bulk [21, 22].

One of the early goals in this research project was to develop methods of fabricating nanostructured materials for use in energy storage devices, for the reasons described above. Chapter 2 and Chapter 6 in this dissertation will focus on those effects. However, the increased use of nanostructured materials has led to another major research area: the characterization of such materials and their behavior during electrochemical cycling. There are a multitude of different methods to characterize and understand the behavior of these materials in energy storage systems. Many researchers have examined the changes that occur on electrode materials during and after electrochemical cycling, using techniques including scanning electron microscopy [23-27], transmission electron microscopy [28-30], x-ray diffraction [31, 32], among others. The method that forms the bulk of this dissertation is electrochemical strain microscopy, a scanning probe microscope technique that seeks to examine at nanoscale the electrical and mechanical interactions in materials for energy storage. Scanning probe techniques have been applied extensively to examine changes in the surface morphology in lithium ion battery electrodes, usually by measuring the surface topography during or after charge and discharge processes [33-35]. Electrochemical strain microscopy is a relatively new technique in which a combination of alternating current (AC) and direct current (DC) biases are applied onto a material surface and the resulting strain changes are measured to correlate the motion of electrons, holes, ions, and vacancies to the applied biases [36, 37]. As this technique was developed only recently, there remain many unanswered questions relating to the underlying mechanisms behind observed phenomena. In order to distinguish among different mechanisms, a series of experimental protocols were designed, which are described in Chapter 3, which provide a framework that can guide future research. Specific applications of electrochemical strain microscopy on lithium iron phosphate as a cathode for lithium-ion batteries are discussed in Chapter 4 and on samarium doped ceria as an electrolyte for solid oxide fuel cells in Chapter 5.

Nanostructured materials have become increasing more important in the field of energy storage. The development of techniques to both manufacture and characterize these materials for use in high efficiency energy storage materials remains a major topic of interest in the research community. The final chapter in this dissertation will present some ideas of possible next steps in this area.

1.2 Energy Storage Systems

1.2.1 Lithium-Ion Batteries

Lithium-ion batteries have become the dominant energy storage technology due to their high energy densities compared to other rechargeable battery systems [38]. Initially, lithium rechargeable batteries were fabricated with an intercalation compound as the cathode and lithium metal as the anode, taking advantage of lithium's low density and electropositivity [39]. However, safety issues arising from the use of lithium metal inhibited this technology's feasibility for wide-spread use. The lithium-ion battery, in contrast, uses intercalation compounds for both anode and cathode, with an inorganic electrolyte, avoiding the stripping and plating that occurs when using lithium. A simplified schematic of a lithium-ion battery is depicted in Figure 1.1, showing the motion of ions and electrons during the charge and discharge processes.

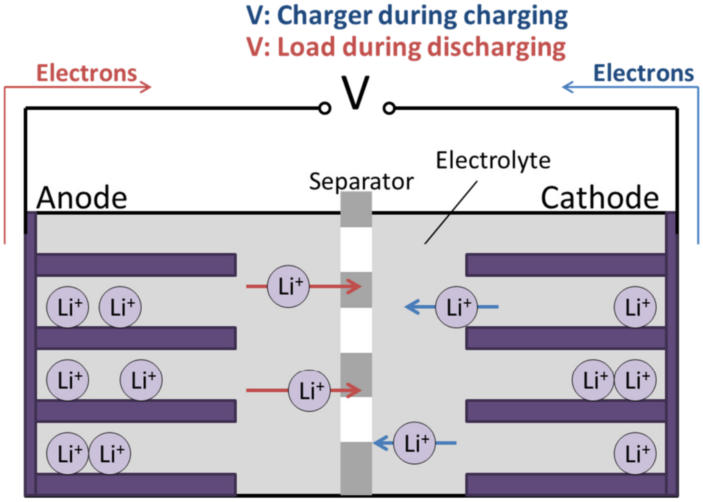

Figure 1.1: Schematic of lithium-ion battery

When Li-ion batteries are charged, lithium ions are released by the cathode, pass across the electrolyte, usually through an ion-porous separator that prevents short-circuiting, and are intercalated into the anode. During discharging, lithium ions undergo the reverse motion, moving from the anode through the electrolyte and into the cathode. The electrochemical processes occurring at the electrodes produce or consume electrons that flow through an external circuit. Although the basic concepts underpinning lithium-ion batteries are straight-forward, the actual processes involved are highly complicated, involving diffusion and electromigration of Li-ions in the electrolyte, electrochemical reactions and charge transfers at the interfaces between electrolyte and electrodes, and intercalation and extraction of Li-ions in electrodes. For example, the successful use of graphite as the anode requires the formation of a solid electrolyte interface that allows for kinetic stability in the system [40, 41], the study of which is a subfield of its own within the lithium-ion battery community.

The current industrial standard for lithium ion batteries consists of a lithium metal oxide such as lithium cobalt oxide as the cathode, graphite as the anode, and an organic electrolyte, with the anode and cathode electrically separated by a polypropylene separator [42]. In order to improve upon the current status quo, researchers have sought out alternatives to each component. For the majority of electrolytes currently in use, lithium hexafluorophosphate ($LiPF_6$) salt is dissolved in a combination of ethylene carbonate (EC) and a linear carbonate such as dimethyl carbonate (DMC), diethyl carbonate (DEC), or ethyl methyl carbonate (EMC) to increase the fluidity and decrease the melting point [43]. However, this compound has its limitations in terms of temperature and voltage range, and is vulnerable to decomposition which can lead to thermal runaway. Researchers have focused on improving the current electrolyte compounds through the use of additives [44], and turning toward aqueous electrolytes [45, 46], gel polymer electrolytes [47, 48], or solid electrolytes [49, 50]. For the lithium-ion anode, technological improvements have approached the theoretical energy density of graphite, and efforts have been underway to develop materials with higher energy densities [51]. Some systems of interest are nanostructured titanium dioxide (TiO_2) [52], tin dioxide (SnO2) [53], and silicon [54], all of which have higher theoretical capacities, but are limited in practical use due to cost, stability, and large volume changes during cycling. On the cathode side, there is a multitude of alternatives to the layered lithium cobalt oxide ($LiCoO_2$), which has a relatively low theoretical capacity and can be expensive due to the limited availability of cobalt [55]. Some alternatives include the spinel structures lithium manganese oxide ($LiMn_2O_4$) [56] and lithium nickel manganese oxide ($LiNi_{0.5}Mn_{0.5}O_2$) [57], vanadium oxides (V_2O_5) [58], and phospho-olivine structures such as lithium iron phosphate ($LiFePO_4$) [59]. It is this latter material, lithium iron phosphate, which serves as the focus of the synthesis and characterization efforts in this project, due to its unique olivine structure in which lithium ions move along one-dimensional channels [60]. The benefits and limitations of this system will be discussed in further detail in Chapter 2.

1.2.2 Solid Oxide Fuel Cells

Fuel cells are storage devices that convert energy from fuel to electrical energy through electrochemical processes. The focus in this work is solid oxide fuel cells (SOFCs), which are named for their ceramic electrolyte, and typically operate at high temperatures [61]. They have attracted significant attention in recent years due to their high efficiencies as well as low emissions, and can serve as combination heating and power systems [62]. A schematic of a solid oxide fuel cell is shown in Figure 1.2.

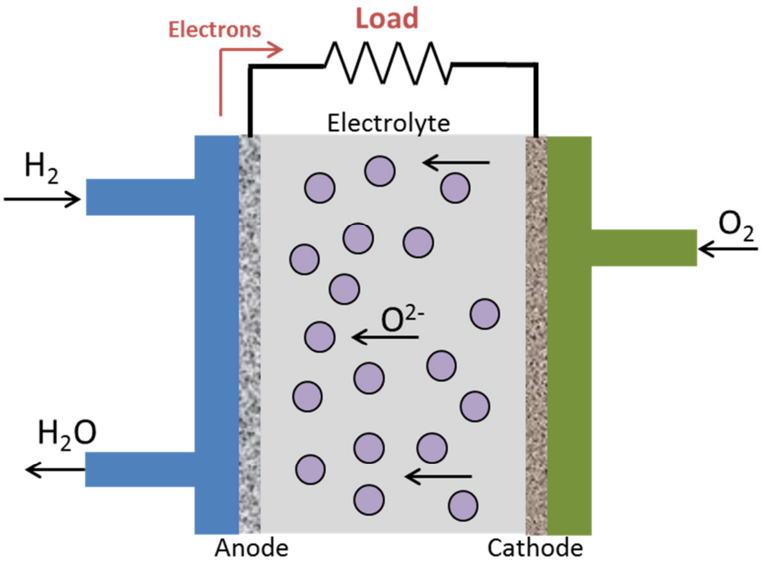

Figure 1.2: Schematic of solid oxide fuel cell

In a solid oxide fuel cell, oxygen is supplied to the system on the cathode side, where it is reduced to oxygen ions. The oxygen ions move through the ion-conducting electronically insulating ceramic electrolyte, and combine with hydrogen, supplied on the anode side, to form water. The reaction of hydrogen and oxygen ions also releases electrons, which flow through an external circuit from anode to cathode. The half-cell reactions can be written as the following:

Anode: $H_2 + O^{2-} \rightarrow H_2O + 2e^-$

Cathode: $\frac{1}{2}O_2 + 2e^- \rightarrow O^{2-}$

On both the cathode and anode sides of the SOFC, conductive catalytic materials are required to carry out the electrochemical reaction. Anode materials are required to be stable at high operating temperatures in the reducing environment at the gas inlet, and not be oxidized at the gas outlet. This limits the choice of materials to nickel, cobalt, and precious metals, with nickel being the most commonly used due to its low cost [62]. The nickel anode is typically mixed with the electrolyte material for the sake of thermal expansion compatibility [63]. In some cases, the nickel/electrolyte composite is doped with metals such as copper or platinum to enhance electronic conductivity, increase catalytic behavior, or to better accommodate the use of hydrocarbon fuels [64, 65]. Cathode materials are typically conducting oxides such as the perovskite-structured lanthanum strontium ferrite and lanthanum strontium cobaltite, also often mixed with the electrolyte [66]. By mixing with the electrolyte, the material is not only more compatible with the system in terms of thermal expansion, but also improves in efficiency due to the increased surface area over which oxygen reduction can occur [67].

The focus in this project is on the solid electrolyte, particularly doped ceria. The solid electrolyte in SOFCs must have good ionic conduction in order to minimize cell impedance, but must also be electrically insulative to minimize leakage currents [68]. Furthermore, the electrolyte must be completely nonporous in order to separate the oxygen and hydrogen fuels. The most common electrolyte currently used is yttria-stabilized zirconia (YSZ), which is particularly suitable for operation at high temperatures, at around 800 - 1000°C [69, 70]. However, YSZ ionic conductivity decreases exponentially with decreasing temperature, and is subject to decreases in conductivity due to aging [71, 72]. A promising alternative to YSZ has emerged in doped cerium oxide, or ceria, which can be used at lower temperatures between 500 - 700°C. Ceria is commonly doped with samarium or gadolinium to increase ionic conductivity, typically at dopant concentrations of up to 20 -25%. In recent years, the efforts in solid oxide fuel cell technology has turned toward decreasing the operating temperature to 500 – 750°C, termed intermediate temperature (IT) SOFCs [73, 74]. As such, the emphasis on doped ceria has become pronounced, particularly focusing on effects of grains in bulk ceria and their influence on ion conduction. However, ceria also exhibits electronic conduction in certain conditions, primarily at low oxygen partial pressures, and nanocrystalline ceria can exhibit this mixed conduction even under oxidizing conditions [75]. The exact mechanism of the electronic conduction is still under debate, and a focus of this project will be on examining the behavior of ions and electrons at surfaces and grain boundaries in order to characterize the mixed conduction behavior.

1.3 Electrochemical Strain Microscopy

The major focus in this dissertation research was to implement electrochemical strain microscopy (ESM) to study nanoscale electrochemical properties of materials for energy storage systems. ESM is a novel technique developed in the past few years by a group at Oak Ridge National Laboratory, based initially on a similar, more well-established, method for probing piezoelectric materials, titled piezoresponse force microscopy (PFM) [76-78]. The basis of both techniques, and in strain-based scanning probe microscopy (SPM) in general, is the use of a conductive scanning microscope tip to apply a series of alternating current (AC) and direct current (DC) voltages to the surface of the material to be studied, inducing strain changes that can be measured as vertical or lateral deflections of the cantilever. The motion of the SPM probe is measured through a laser reflecting off of the cantilever and directed at a photodiode, capable of detecting strains on the order of picometers. A simplified schematic for ESM is presented in Figure 1.3.

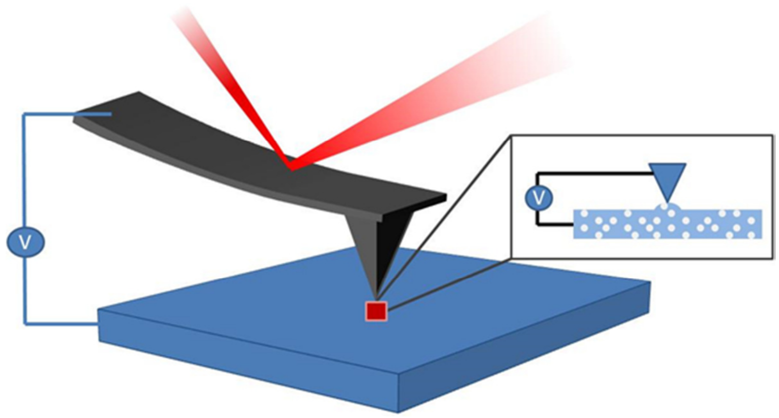

Figure 1.3: Schematic of electrochemical strain microscopy

Unlike the well-defined responses in ferroelectric materials measured through PFM, the responses measured during ESM are complex and can be governed by many different underlying material behaviors. The exact material behaviors that govern the measured strains are not yet fully known, but experiments can be performed to distinguish among possible mechanisms, as will be discussed in Chapter 3.

1.4 Dissertation Overview

This dissertation covers research performed over the past four years in both fabricating and characterizing nanostructured materials for energy storage systems. Chapter 2 covers the synthesis of nanostructured lithium iron phosphate fibers through electrospinning and multi-step thermal treatment. Chapter 3 begins the electrochemical strain microscopy portion of the dissertation by introducing some of the many techniques developed to distinguish among different mechanisms behind observed strain behavior. Chapters 4 and 5 describe specific applications of electrochemical strain microscopy on lithium iron phosphate (Chapter 4) and samarium doped ceria (Chapter 5). During the course of the past few years, a portion of time was spent each year at the Jet Propulsion Laboratory, developing materials for metal-air batteries. The research performed during those internships is described in Chapter 6. Finally, Chapter 7 will summarize the research covered in this dissertation and present some ideas for the next steps in this area.

2 Synthesis of $LiFePO_4$ Fibers through Electrospinning

2.1 Motivation

Although lithium-ion batteries have become the dominant energy storage solution in many industries, including consumer electronics and automotive power, improvements in each of these applications require even more performance and reliability from these batteries. In order to increase capacity and cyclability, researchers have turned to nanostructured materials for electrodes [79, 80], for many reasons. The rate of lithium ion intercalation and electron transport can increase in nanostructured morphologies due to reduced distances [81] . Furthermore, as the individual particle sizes are reduced within a material, the overall surface area is correspondingly amplified, allowing for better contact with the electrolyte and increasing lithium-ion flux across the electrode-electrolyte interface. Researchers have found that nanostructured systems that include degrees of porosity also demonstrate increased capacity and longevity, due to porous materials being able to accommodate substantial volume change during lithium-ion intercalation and extraction without irreversible damage [82, 83].

The primary electrode system focused on here is lithium iron phosphate ($LiFePO_4$) as a cathode for lithium-ion batteries. $LiFePO_4$ is being developed as a competitive candidate to replace the now commonly used $LiCoO_2$ due to its low toxicity, high thermal stability, abundant sources, and its relatively lower costs [84, 85]. Its olivine structure allows for reversible insertion and extraction of lithium ions, with a theoretical specific capacity of 170 mAh/g at a steady voltage of 3.45 V versus lithium [86]. The structure of $LiFePO_4$ is shown in Figure 2.1(a), along with a typical charge/discharge curve in Figure 2.1(b).

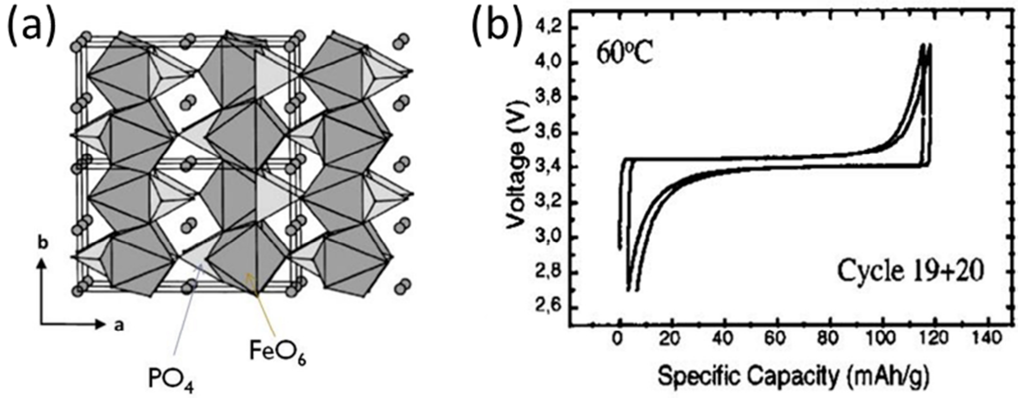

Figure 2.1: (a) Crystalline structure of $LiFePO_4$ [87] (b) Typical charge/discharge curve for LiFePO4 showing steady voltage [88].

Within this olivine structure, insertion and extraction of lithium ions occur with the following two-phase reaction: $LiFePO_4 \leftrightarrow FePO_4 + Li^+ + e^-$

Lithium ions can only travel through 1-D channels, along the b direction in the figure above. One major drawback of $LiFePO_4$ as a cathode material is its poor electronic and ionic conductivity, especially when the particles are large, since the channels can be more easily blocked by ionic disorder, foreign phases, or stacking faults. For practical use, $LiFePO_4$ is often coated with carbon or other conductive materials [89], most commonly by introducing a carbon source into the synthesis procedure. Many kinds of carbonaceous organic compounds, including precursor materials containing acetates, carbonates, and citrates, can be incorporated prior to annealing in a reducing atmosphere, forming a homogeneous carbon coating on the final material [90].

Due to the unique nature of $LiFePO_4$ and the method by which lithium ions travel in 1-D channels, forming nanostructured materials is crucial to the performance of the electrode. The primary methods of synthesis discussed in this work are solution-based electrospinning techniques used in conjunction multi-step thermal treatment.

2.2 Principles of Electrospinning

Electrospinning is a convenient and versatile technique that has been developed to process polymeric, ceramic, metallic, and composite nanofibers with diameters ranging from 10s of nanometers to micrometers [91-93]. The setup for electrospinning consists of a spinneret with a metallic needle, a syringe pump, a high-voltage power supply, and a grounded collector. A viscous solution is loaded into the syringe and driven to the needle tip by a syringe pump, forming a droplet at the tip. A high voltage is then applied to the needle, and the droplet is stretched. If the viscosity of the solution is sufficiently high, an electrified liquid jet is formed. The jet is then stretched and whipped continuously by electrostatic repulsion until it is deposited on the grounded collector, resulting in nanofibers with uniform cross-section. However, if the viscosity is low, which can be controlled by adjusting polymer concentration, then the droplet cannot be stretched into a continuous nanofiber, and is broken into smaller droplets instead. A schematic of this processing technique is shown in Figure 2.2(a), alongside a photograph of the actual laboratory setup in Figure 2.2(b).

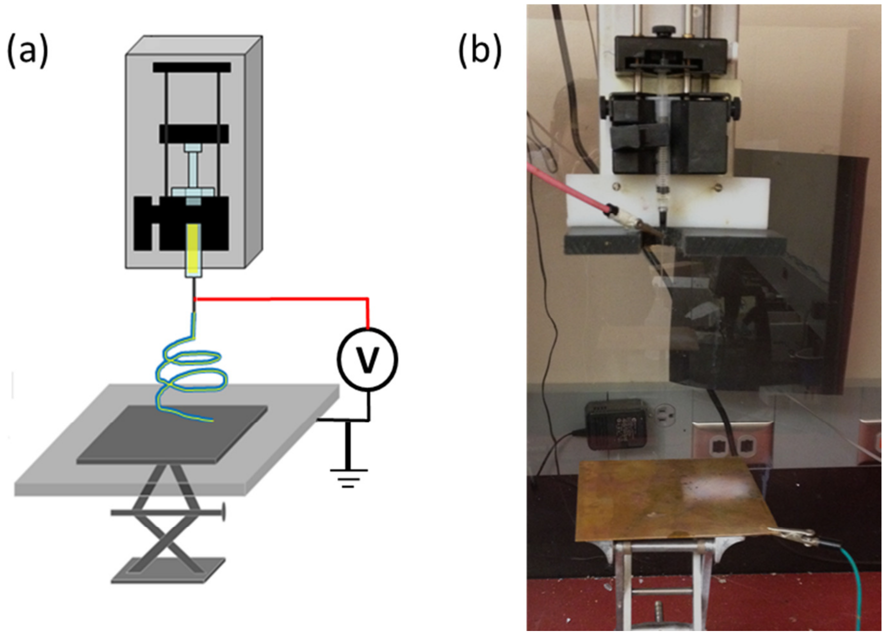

Figure 2.2: (a) Schematic of electrospinning, with voltage applied between syringe needle and conductive collector, (b) picture of actual electrospinning setup in laboratory

Initially, electrospinning was developed to fabricate polymer fibers, in which materials such as polyethylene, polystyrene, and polyacrylonitrile are mixed with solvents to form viscous solutions, and then electrospun into fibers of varying diameters and morphologies. Later, electrospinning techniques were expanded to fabricating ceramic nanofibers by electrospinning followed by annealing [94], particularly for applications in lithium-ion batteries [95, 96]. There are many variables that affect the resulting fibers, both within the precursor solution as well as during the electrospinning process [97]. The precursor solution properties that affect the resulting electrospun fibers include surface tension, conductivity, and viscosity, while the applied voltage, tip-to-collector distance, and solution flow-rate affect the fibers during electrospinning. Furthermore, the electrospinning environment, such as temperature and humidity, also has an effect on the final material.

In this research project, electrospinning is used to form lithium iron phosphate, a highly crystalline material that must be annealed to form the olivine structure. Furthermore, the polymer component of the precursor solution must be selectively annealed so that a portion of it is converted to carbon to increase conductivity [98].

2.3 Electrospinning Results

There were two main paths taken in this project, based on two different precursor formulations. The first was based on an acetate solution, consisting of lithium acetate, iron (II) acetate, and phosphoric acid, inspired by the work of Zhang's group at North Carolina State University [90]. The advantage of using this particular set of precursor ingredients is that the iron ions present in the solution are already in the ferrous state, which is necessary for the formation of lithium iron phosphate. As a result, the iron ions do not need to be further reduced during the annealing process, but simply needs to be prevented from oxidizing. Zhang's group dissolved these precursor elements into polyacrylonitrile (PAN) and N,N-dimethylformamide (DMF) for electrospinning. The goal of this research project was to use the same $LiFePO_4$ precursor materials to form fibers through electrospinning, but to replace PAN with the much less expensive polyvinylpyrrolidone (PVP), and replace the highly toxic DMF with a water/acetone solution.

The second path described in this research project was to electrospin $LiFePO_4$ using a nitrate-based set of precursor ingredients, consisting of lithium hydroxide, ferric nitrate, and phosphoric acid, based on the work of Yanyi Liu in Cao's group [99]. This set of precursor ingredients uses iron ions in its ferric state, requiring iron to be reduced to its ferrous state during the synthesis and annealing procedures. However, these materials are readily soluble in water at relatively high molarities, which is beneficial when forming viscous precursor solutions for electrospinning. The work of Yanyi Liu was geared toward forming thin films through drop-casting, so her recipe was modified by adding PVP to increase viscosity for electrospinning and removing ascorbic acid since PVP by itself was sufficient to reduce Fe^{3+} to Fe^{2+}. The goal for this part of the research project was to determine if electrospinning in conjunction with a multi-step thermal treatment process could form porous lithium iron phosphate fibers.

2.3.1 Acetate route of synthesis

This synthesis process began by mixing together lithium acetate, iron (II) acetate, and phosphoric acid with a molar ratio of 1:1:1 with respect to Li:Fe:P, and adding water to form a 10 wt% solution. This particular mixture tends to be insoluble in water. To resolve this issue, citric acid is added in order to raise the pH of the solution, which in turns aids solubility [100]. In addition, the citric acid serves as a source of carbon in the final annealed material. Citric acid was added at 2.3 wt%, and the entire solution was heated to 60°C for 30 minutes to aid dissolution. Polyvinylpyrrolidone (PVP) was added to the solution at three different concentrations: 8%, 9%, and 10%, by weight. All of the solutions were electrospun at a voltage of 20 kV applied at a distance of 12 cm from electrospinning tip to collector. Scanning electron microscope images of the electrospun fibers are presented in Figure 2.3.

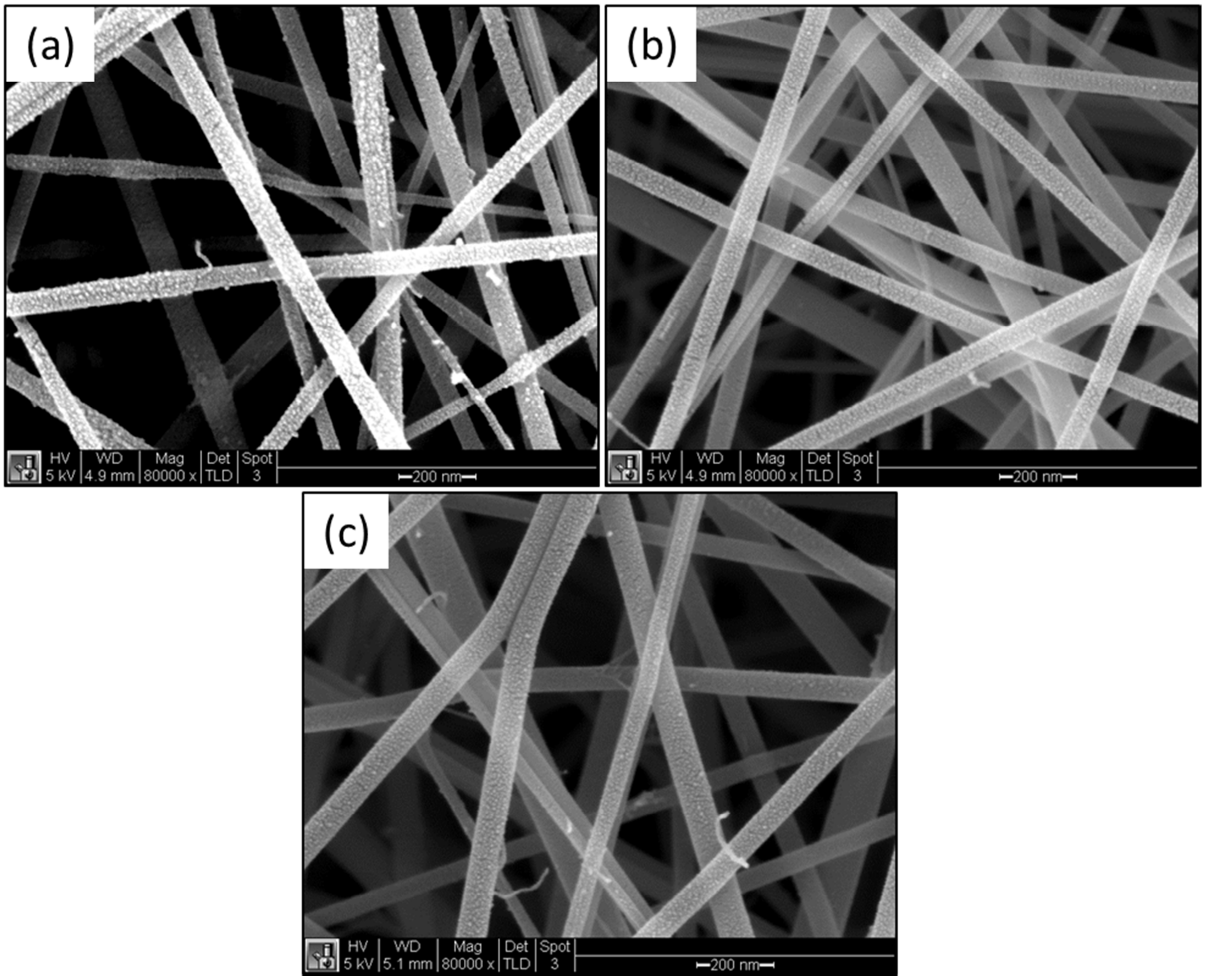

Figure 2.3: SEM images of electrospun fibers with three different concentrations of PVP added.

As Figure 2.3 shows, the fibers all had diameters between 50 – 70 nm, regardless of the concentration of PVP. Higher concentrations of PVP, however, made the electrospinning process more difficult because the solution had a tendency to coagulate at the tip of the syringe. Therefore, subsequent thermal treatment processes were performed on the 8% PVP solution only. A multi-step thermal treatment process was performed, based on a method developed to produce carbon nanofibers [98] from PVP. The effect of each thermal treatment step on the morphology of the fibers is presented in Figure 2.4.

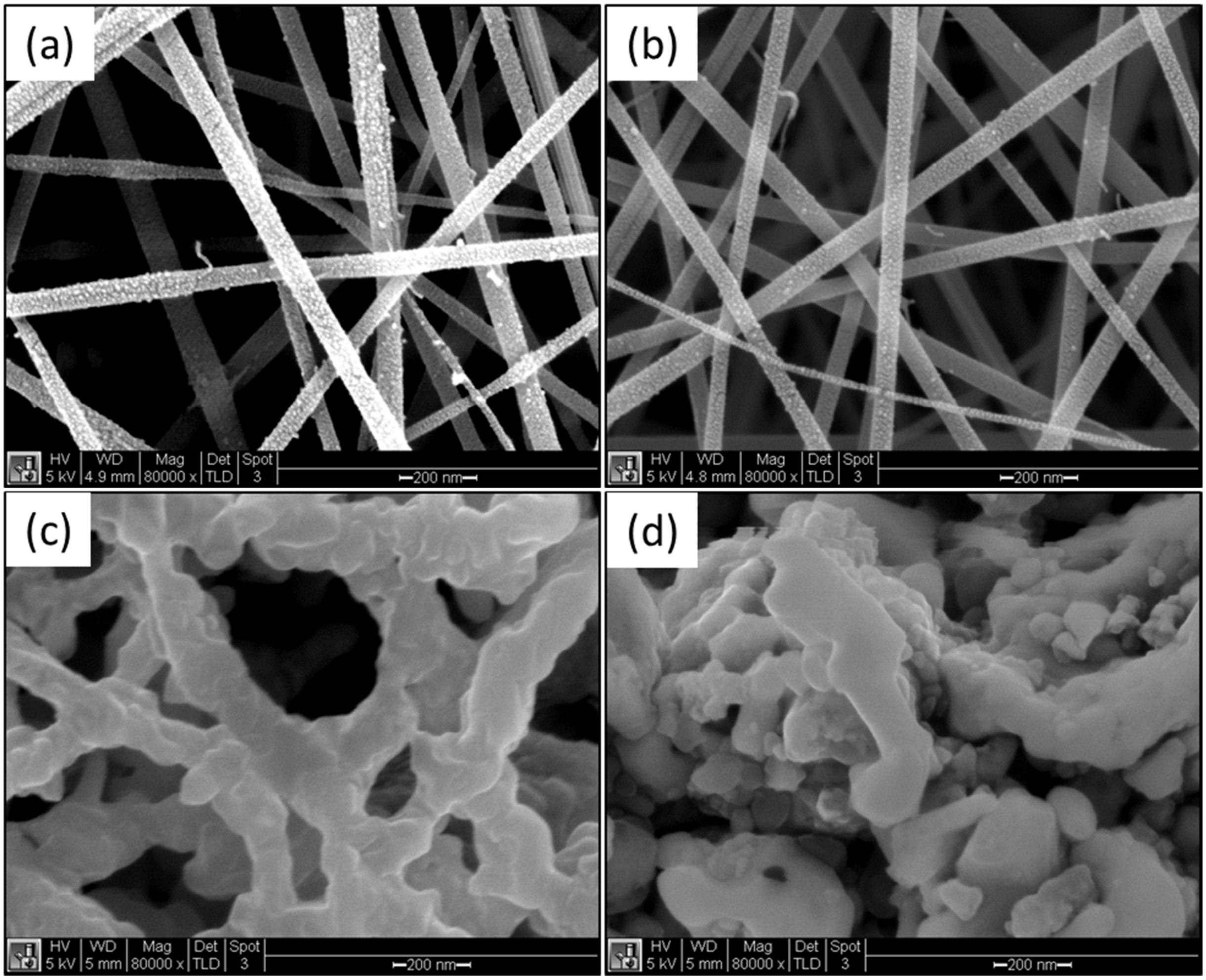

Figure 2.4: SEM images of $LiFePO_4$ fibers after being (a) electrospun, then (b) stabilized in air at 150°C for 24 hours, (c) pre-oxidized in air at 360°C for 4 hours, and (d) annealed in flowing nitrogen at 600°C for 3 hours.

The fibers were first dried in air at 150°C for 24 hours, which serves to slowly allow all of the solvents to evaporate and stabilize the fibrous morphology. The stabilization step does not alter the fibers significantly, except to slightly decrease fiber diameter through solvent evaporation, as

Figure 2.4(b) demonstrates. The stabilized fibers were heated in an oven in air at 360°C for 4 hours as a pre-oxidation step to preserve the fibrous structure prior to converting the PVP to carbon during annealing. It appears that this pre-oxidation process begins to crystallize the lithium iron phosphate structure, as Figure 2.4(c) depicts, but the material is still in its fibrous structure. Finally, the sample was annealed in flowing nitrogen gas at 600°C for 3 hours to form the olivine lithium iron phosphate. This final crystallization step destroys the fibrous structure, leaving behind scattered small lithium iron phosphate crystals, as shown in Figure 2.4(d). The main problem with this particular synthesis route is that the fibers are initially very thin in diameter yet high in polymer concentration, and once crystallization begins, it is difficult to maintain the fibrous structure. Attempts to increase the diameter of the fibers by increasing the concentration lead to coagulation at the tip of the syringe, rendering electrospinning impossible. Another common method to increase the diameter is to reduce the applied voltage between syringe and collector, but this resulted in formation of particles rather than fibers for this particular system. As a result, a different formulation for electrospinning lithium iron phosphate fibers was pursued.

2.3.2 Nitrate route of synthesis

The second synthesis route discussed here is based on a synthesis method developed by Liu et. al. [99] for synthesizing $LiFePO_4$ thin films by forming a dilute precursor solution and then drop-casting. The electrospinning precursor solution took basic elements from her formulation, beginning by mixing together phosphoric acid, iron (III) nitrate nonahydrate, lithium hydroxide monohydrate, and ascorbic acid at a molar ratio of 1:1:1:1 for P:Fe:Li:ascorbic acid, and then added to water at a concentration of 1 mol/L. The 1 M solution was then heated on a hot plate to 60°C, and held at that temperature for an hour in order to allow the ascorbic acid to fully dissolve. Polyvinylpyrrolidone (PVP) was then added to the solution at 6.5 wt% after mixing to increase viscosity and serve as an additional source of carbon. The resulting solution was electrospun at 20 kV at a distance of 10 cm to the plate. Due to the conductivity of the precursor solutions, particularly the nitrate, the electrospun fibers took on a cloudy consistency between the electrospinning needle and the collection plate, as shown in the Figure 2.5(a).

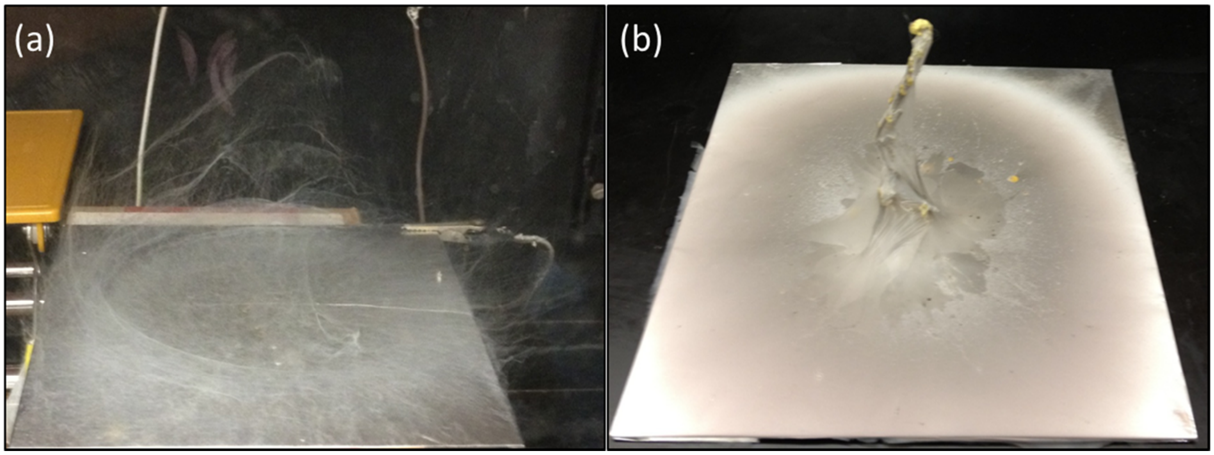

Figure 2.5: (a) $LiFePO_4$ precursor solution during electrospinning process (b) Electrospun fibers with clumping evident

The cloudiness during the electrospinning process eventually leads to clumps forming in the final material, as depicted in Figure 2.5(b).

Platinum-coated silicon substrates were used to collect small amounts of the electrospun fibers, which were then annealed in nitrogen gas at 600°C for crystallization. Scanning electron microscope images of the annealed fibers are shown in Figure 2.6.

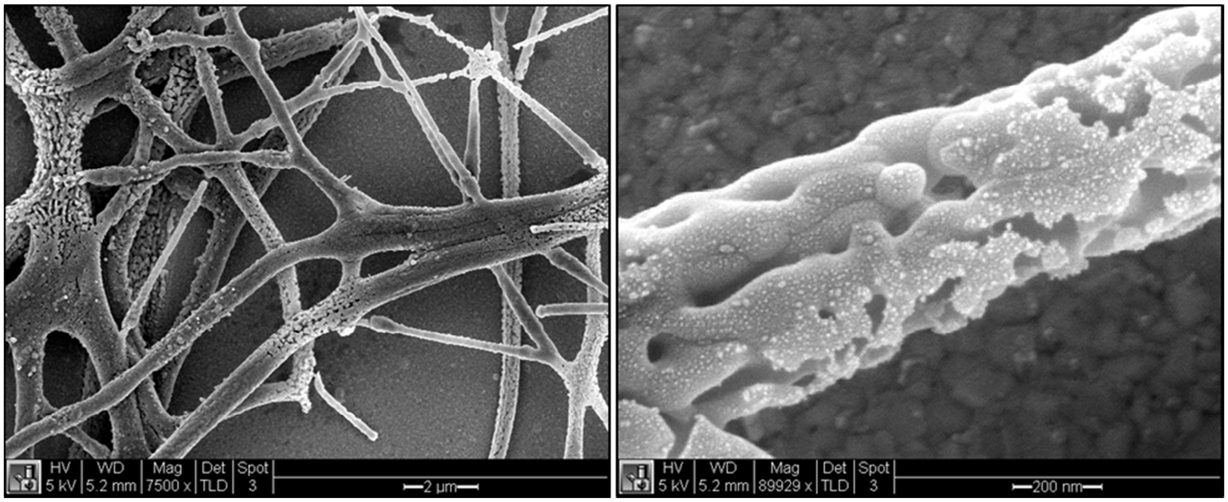

Figure 2.6: Scanning electron microscope images of annealed $LiFePO_4$ at two different magnifications

As the figure shows, the fibers range in diameter from approximately 500 nm to 1 μm. The fibers on Pt/Si were assembled into a battery half-cell using the three-electrode method, with an Ag/Ag^+ electrode serving as reference, as pictured in Figure 2.7(a). The first charge and discharge curves of this electrode are shown in Figure 2.7(b), below. Due to the very small amount of fibers that adhered to the substrate, an accurate measurement of mass, and therefore specific capacity, could not be made.

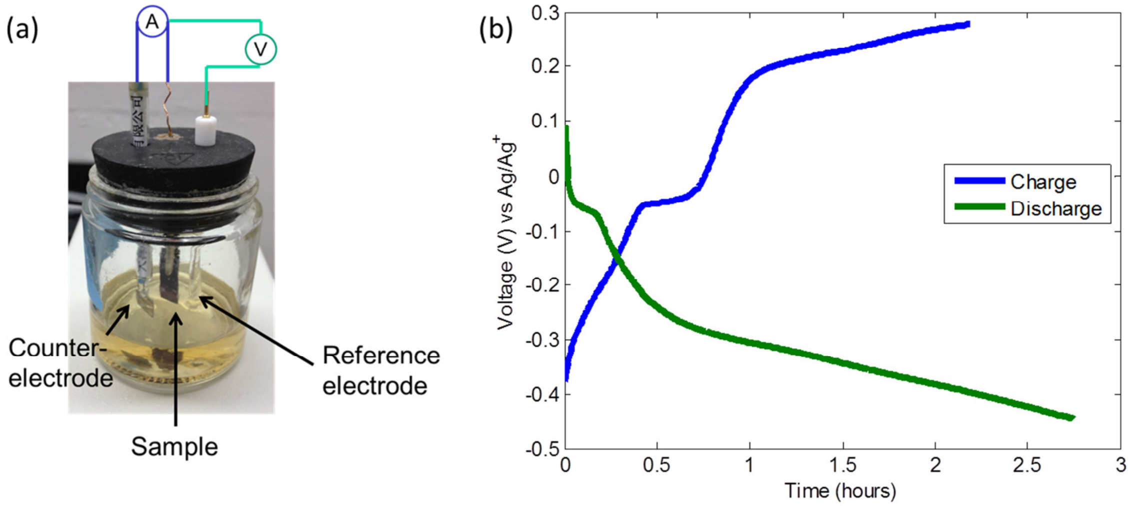

Figure 2.7: (a) Three-electrode electrochemical cell, and (b) charge/discharge curve for $LiFePO_4$ fibers

This synthesis route appeared to be promising, but had several major issues. In Figure 2.7(b), there is a slight plateau at around -0.05 V vs. Ag/Ag+, which corresponds to the expected 3.45 V vs. Li plateau expected from lithium iron phosphate. However, the overall capacity of this sample is low, due in part to the large quantities of carbon present in the fibers. In addition, because of the clumping of fibers during the electrospinning process, it is difficult to fabricate larger quantities of fibers for electrochemical testing. For the first problem, an effort was made to reformulate the precursor solution to reduce the amount of material that would convert to carbon upon annealing. The original formulation utilized ascorbic acid as a reducing agent, but through x-ray diffraction (XRD), it was found that citric acid or PVP by itself was sufficient to reduce Fe^{3+} to Fe^{2+} during the annealing process. Three solutions containing $LiFePO_4$ precursor ingredients were created, and one of the reducing agents of citric acid, ascorbic acid, or PVP was added to each. The solution was dried and annealed in flowing nitrogen, and the resulting powders were ground up for XRD, with the results plotted in Figure 2.8.

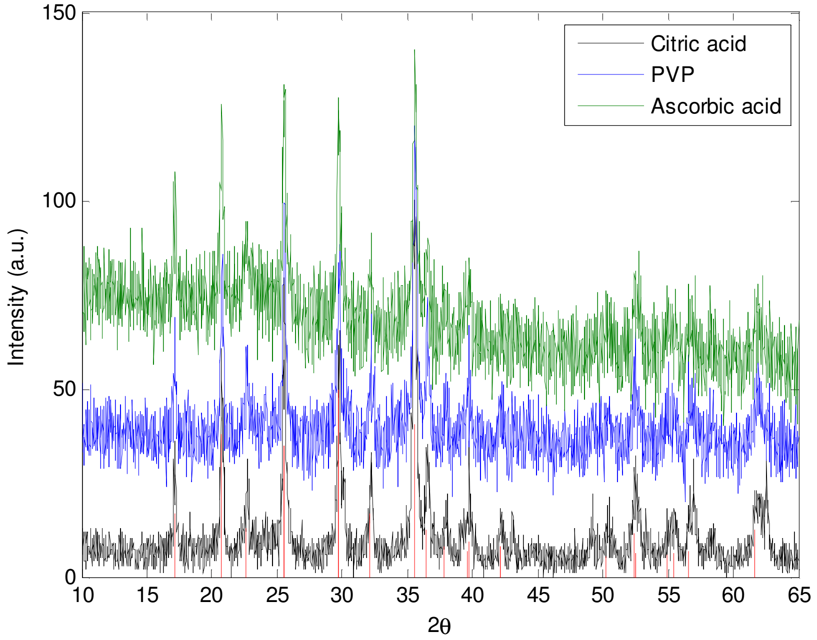

Figure 2.8: X-ray diffraction data for lithium iron phosphate synthesized with citric acid, PVP, and ascorbic acid as reducing agents. The red vertical lines correspond to expected $LiFePO_4$ olivine peaks.

All three sets of powders displayed the characteristic peaks of olivine $LiFePO_4$, indicating that any of these reducing agents alone would be sufficient to reduce Fe^{3+} to Fe^{2+}. Since the addition of PVP is necessary to increase viscosity, for further experiments, only PVP was added to the $LiFePO_4$ ingredients.

The other major drawback of the nitrate synthesis route is the conductivity of the electrospinning solution that creates the cloudiness present in Figure 2.5(a), making it difficult to fabricate larger quantities of these fibers. To solve this problem, a modification to the electrospinning set-up was made, using a rotating drum collector rather than a flat plate. The schematic of the rotating drum is shown in Figure 2.9(a). The rotating drum manually forces the fiber to coil around the collector, rather than being attracted to the electrospinning tip. An actual rotating drum was designed and manufactured by Feiyue Ma, another member of the research group, and a picture of this set-up is presented in Figure 2.9(b).

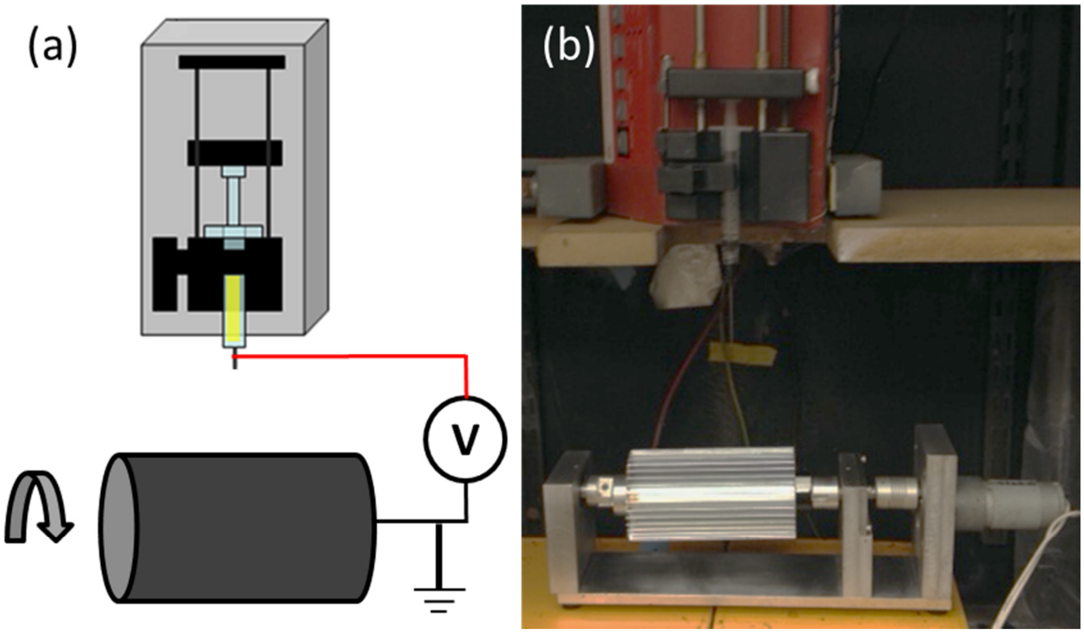

Figure 2.9: (a) Schematic of rotating drum fiber collector along with (b) picture of actual setup in laboratory.

With the rotating drum set-up, larger quantities of lithium iron phosphate fibers could be fabricated from the nitrate formulation. The precursor solution was similar to that previously used, consisting of phosphoric acid, iron (III) nitrate nonahydrate, and lithium hydroxide monohydrate at a molar ratio of 1:1:1 for P:Fe:Li dissolved in water at a 1 M concentration. The solution was heated to approximately 50°C to aid dissolution, and PVP was added at 7 wt% for electrospinning purposes. Higher concentrations of PVP were also attempted, but led to coagulation at the tip of the syringe. Scanning electron microscope images of the electrospun fibers is presented in Figure 2.10, showing fibers of diameters of approximately 500 nm to 1 μm in diameter, similar to that in the original formulation.

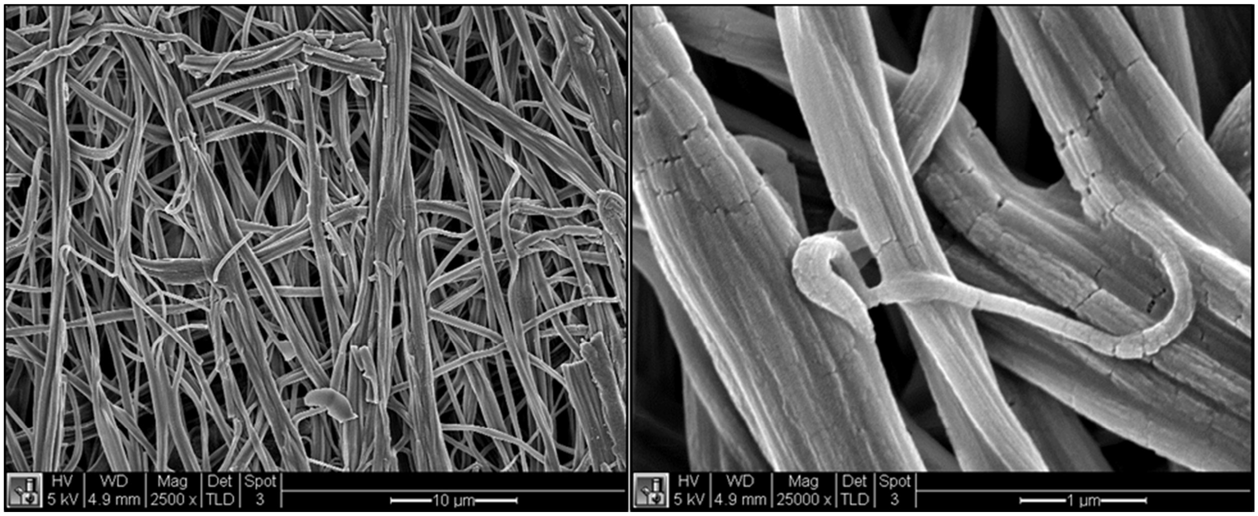

Figure 2.10: Scanning electron microscope images of electrospun lithium iron phosphate fibers at different magnifications

The same multi-step thermal treatment described previously was also applied to these fibers, but here the influence of each thermal treatment step on fiber morphology is isolated and examined. The final annealing step of 3 hours in flowing nitrogen at 600°C remained unaltered.

The first thermal treatment step was to stabilize the fibers at 150°C for 24 hours. In Figure 2.11, fibers that were directly annealed are compared against fibers that underwent the stabilization step prior to annealing.

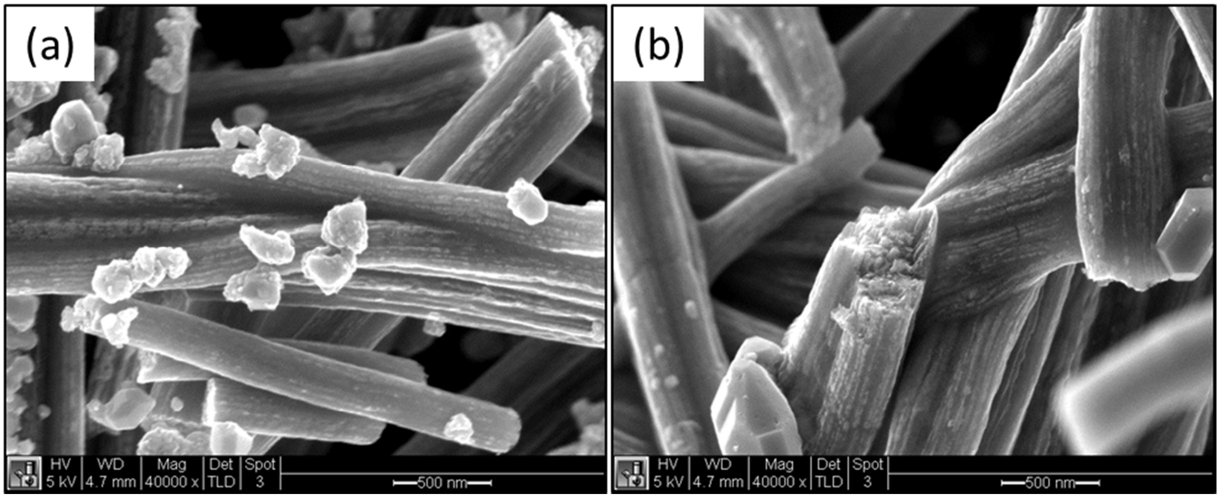

Figure 2.11: SEM images of electrospun $LiFePO_4$ fibers (a) directly annealed in N_2 at 600°C for 3 hours, and (b) first stabilized at 150°C for 24 hours and then annealed in N_2 at 600°C for 3 hours.

From the SEM images, there does not appear to be a significant effect in the morphology of the fibers from the stabilization step by itself. The next thermal treatment step was a pre-oxidation at 360°C in air for four hours. However, when this particular thermal treatment step was applied to the fibers followed by annealing, the resulting material was orange in color, indicating presence of iron in its ferric state, most likely forming $Li_3Fe_2(PO_4)_3$. When there is not enough PVP present during the annealing step, the iron present tends to oxidize into its ferric state. The pre-oxidation step was reduced in length until annealed fibers remained dark brown after annealing. The difference in color between fibers pre-oxidized for 4 hours and fibers pre-oxidized for 30 minutes is shown in Figure 2.12.

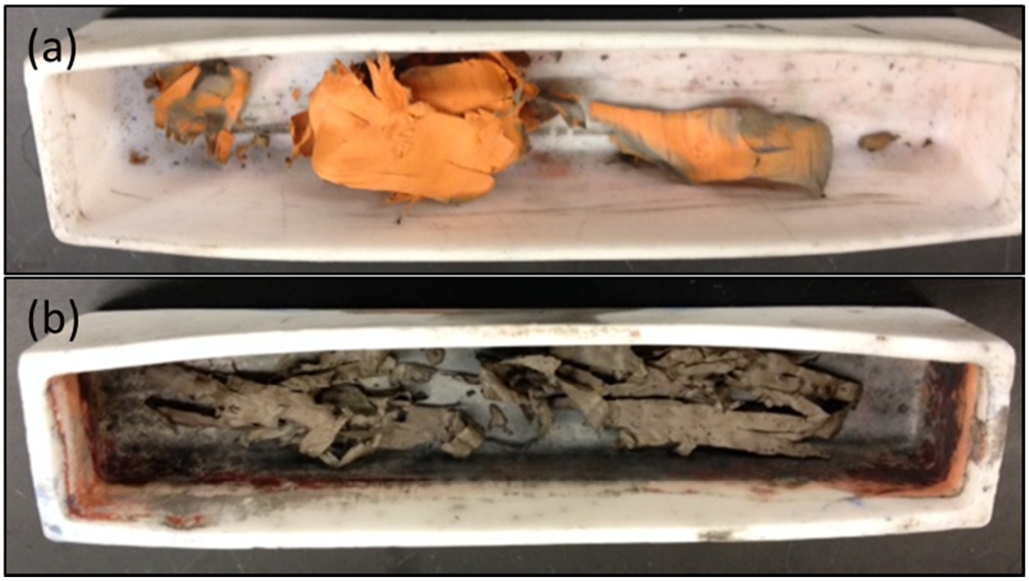

Figure 2.12: Fibers annealed in N_2 gas for 3 hours that have been first pre-oxidized for (a) 4 hours, and (b) 30 minutes

From this set of experiments, it was determined that the pre-oxidation step could not be more than 30 minutes at 360°C. This pre-oxidation step appeared to have a significant effect on the morphology of the electrospun fibers, making the fibers slightly porous, as shown in Figure 2.13.

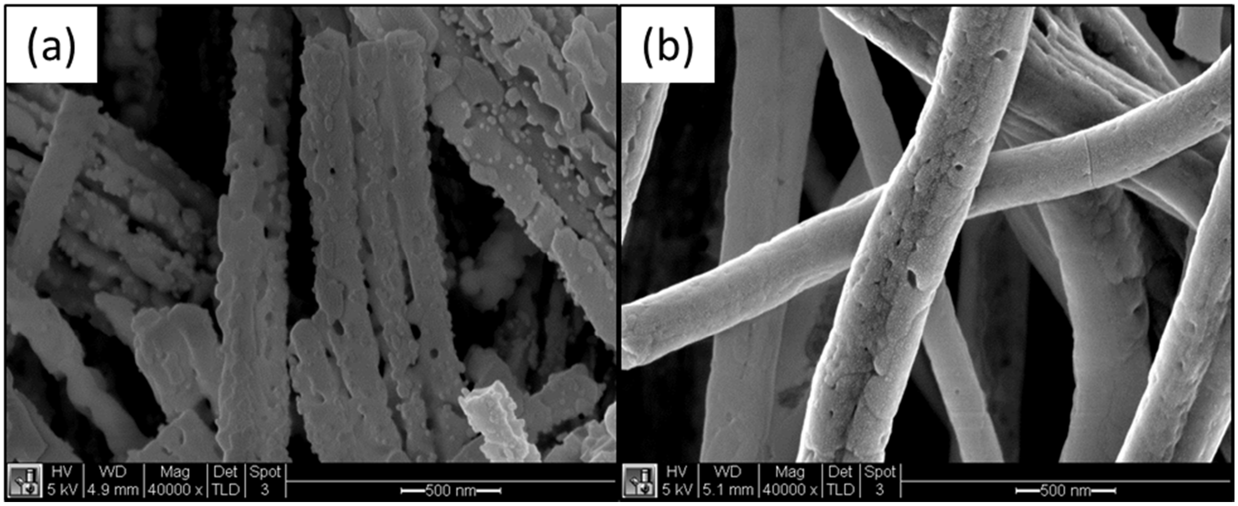

Figure 2.13: SEM images of $LiFePO_4$ fibers that have been (a) pre-oxidized at 360°C for 30 minutes, then annealed in N_2 at 600°C for 3 hours, and (b) stabilized at 150°C for 24 hours, pre-oxidized at 360°C for 30 minutes, then annealed in N_2 at 600°C for 3 hours.

Furthermore, fibers that were pre-oxidized without the stabilization step appeared to be slightly more porous than fibers that were first stabilized before the pre-oxidation and annealing steps. By using a pre-oxidation step, porous lithium iron phosphate fibers could be fabricated through solution-based synthesis, electrospinning, and multi-step thermal treatment.

2.4 Summary

Electrospinning has proven to be a versatile technique in the fabrication of electrode materials for lithium ion batteries. Up to this point, fabrication of lithium iron phosphate fibers using electrospinning techniques have involved the use of PAN as the polymeric thickener, which is fairly expensive, and NMP to dissolve the precursor ingredients, which is highly toxic. Efforts were undertaken to replace PAN with PVP and NMP with water or acetone. An acetate based synthesis route was first attempted, with the formation of the precursor solution facilitated by citric acid as an aid for dissolution. The electrospun fibers from this precursor formulation were very thin in diameter, ranging from 50 – 70 nm. Due to the thinness of the electrospun fibers, it was very difficult to maintain the fibrous structure during subsequent annealing processes. Efforts to increase the initial diameter were unsuccessful due to coagulation at the syringe tip when increasing polymer concentration and spraying of droplets rather than fibers when decreasing applied voltage during electrospinning.

Lithium iron phosphate fibers with larger diameters could be formed after switching to a nitrate formulation that was more easily dissolved in water. The nitrate formulation was too conductive to electrospin using a plate collector, so a rotating disc collector had to be manufactured for synthesizing larger quantities of fibers. These fibers were stabilized, pre-oxidized, and annealed to form olivine lithium iron phosphate, and the effects of each thermal treatment step on the morphology of the fibers was studied. The use of a pre-oxidation step proved crucial to the formation of porous fibers. The fibers formed during this process appeared to be promising for use as lithium ion battery cathodes. However, the electrospinning and thermal treatment processes were extremely time-consuming, rendering this process inefficient for large-scale manufacturing of lithium-ion battery electrodes. A method to mass-produce fibers by electrospinning in conjunction with modifying the thermal treatment process would have to be developed in order for this technique to be feasible for practical use. Due to these limitations, electrochemical characterization of electrospun fibers for lithium-ion batteries was not completed.

3 Electrochemical Strain Microscopy: Distinguishing Mechanisms

3.1 Motivation

The development of electrochemical strain microscopy in the past few years has galvanized researchers into delving into the intricacies of bias-induced strain measurements within scanning probe microscopy. The underlying premise of these measurements, applying a series of alternating current (AC) and direct current (DC) electric fields to the surface of a material of interest using a scanning probe microscope cantilever, was originally used to examine ferroelectric materials as piezoresponse force microscopy [77, 78, 101]. In ferroelectric materials, the strains induced through the application of AC biases were the result of the piezoelectric effect, in which oscillating electric fields induce strain changes through motion of cations and anions within an asymmetrical crystal lattice [102]. The characteristic property of ferroelectric materials, the existence of spontaneous dipole moment that can be polarized, can be observed using PFM by applying DC voltages and observing hysteretic reversals in phase and butterfly-type loops in amplitude. A simplified schematic for the mechanism that governs PFM is presented in Figure 3.1.

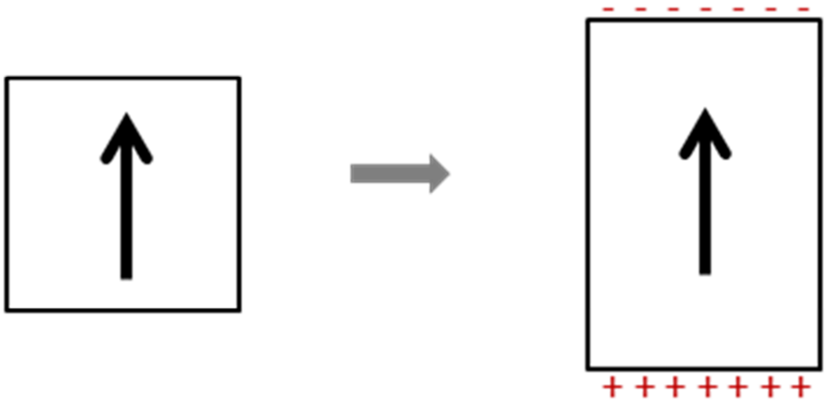

Figure 3.1: Schematic of electromechanical coupling due to piezoelectric effect

In the past few years, a group of researchers at Oak Ridge National Lab developed electrochemical strain microscopy to study lithium-ion battery electrodes [36, 103, 104]. This technique was later applied to electrodes for fuel cells and metal-air batteries [105], and solid electrolytes for lithium-ion [106] and solid oxide fuel cells [107]. However, as the range of applications expanded, there arose many more questions about the nature of the measured electrically-induced strain. The original explanation behind electrochemical strain microscopy was that the observed strains were Vegard strains from concentration changes of lithium ions or oxygen vacancies, as schematically described in Figure 3.2. However, this explanation appears insufficient to cover all of the observed phenomena.

Figure 3.2: Schematic of electromechanical coupling due to Vegard strain

A series of recent publications in particular motivated this particular project. Recent studies have experimentally observed electromechanical coupling in glass [108] and silicon [109], and additionally observed that both materials can exhibit hysteretic phase loops and butterfly amplitude loops. Neither material is piezoelectric nor ferroelectric, yet their behavior resemble the characteristics of classical ferroelectrics. At the same time, these materials also do not follow the rules that would classify their behavior under Vegard strain. It is suggested that their behavior is the result of electrostrictive behavior of the dipoles in the material, as schematically described in Figure 3.3.

Figure 3.3: Schematic of electromechanical coupling due to electrostriction.

Recent research on samarium doped ceria, an electrolyte for solid oxide fuel cells [107], attributed observed strains to Vegard strains due to the motion of oxygen vacancies. However, in further experiments performed in this project, as described in more detail in Chapter 5, another possible explanation arose, that of valence change being the underlying mechanism rather than ionic motion. Due to these disputes within the research community, it became increasingly necessary to develop a series of methods and experiments that can distinguish among different possible mechanisms and answer the crucial questions that arise during strain-based scanning probe microscopy.

3.2 Resonance Enhancement

Typical amplitudes of surface strain induced by an applied AC bias during ESM are on the order of 10 pm or less, which although detectable, can be difficult to separate from the inherent noise in the system. In order to magnify the response, the AC bias is applied at frequencies close to the resonance frequency of the tip-sample interaction to enhance the sensitivity, magnifying the responses by orders of magnitude. Analytically, the cantilever-sample system can be regarded as a damped driven harmonic oscillator, with the amplitude (A) and phase (φ) at a particular frequency (ω) given by [110]

$$\boldsymbol{A(\omega) = \frac{A_{drive}\omega_0^2}{\sqrt{\left(\omega_0^2-\omega^2\right)^2+(\omega_0\omega/Q)^2}}} \tag{3.1}$$

$$\boldsymbol{\varphi = tan^{-1}\left(\frac{\omega_0\omega}{Q({\omega_0}^2-\omega^2)}\right) + \varphi_{drive}} \tag{3.2}$$

where ω_0 is resonant frequency and Q is the quality factor, and A_{drive} and φ_{drive} refer to the intrinsic surface oscillation amplitude and phase. Close to the resonance frequency, the amplitude and phase in the real system does, indeed, behave as governed by equations (3.1) and (3.2), as depicted in Figure 3.4. The red and green dots in Figure 3.4 represent experimentally measured amplitude and phase from the lock-in amplifier, and the black curves are fitted by equations (3.1) and (3.2). By fitting such curves, the intrinsic, or drive, amplitude and phase can be calculated for a specific location.

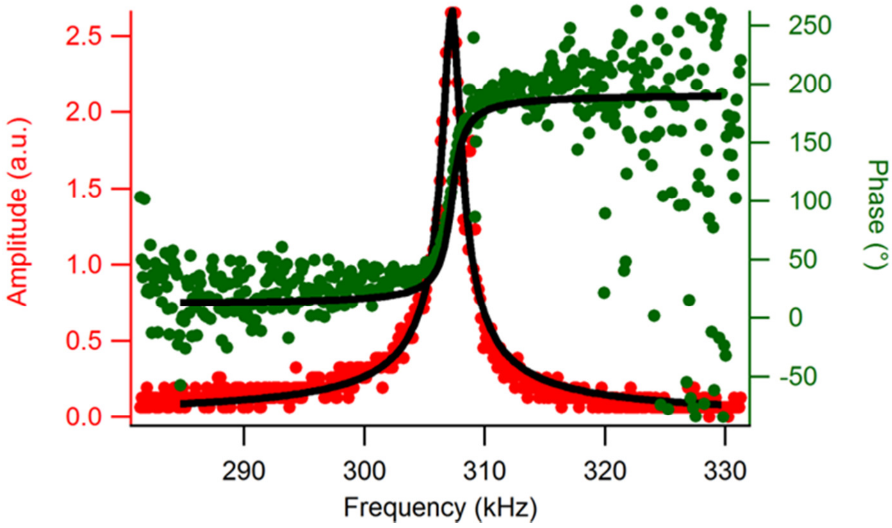

Figure 3.4: Amplitude (red) and phase (green) as a function of frequency close to resonance

Such measurements of amplitude and phase as a function of frequency are time-consuming when used in conjunction with lock-in amplifiers. However, the use of a single frequency when mapping a region of a material is problematic, because the resonance frequency varies from location to location. As an example, in Figure 3.5(a), a 2 µm by 2 µm ESM mapping of $LiFePO_4$ is shown, with three locations selected. At each location, bias was applied over a sweep of frequencies, with the corresponding amplitudes plotted, as shown in Figure 3.5(b). The resonance frequency can shift by as much as 20 kHz in this particular case, since the resonant frequency is highly dependent on topography.

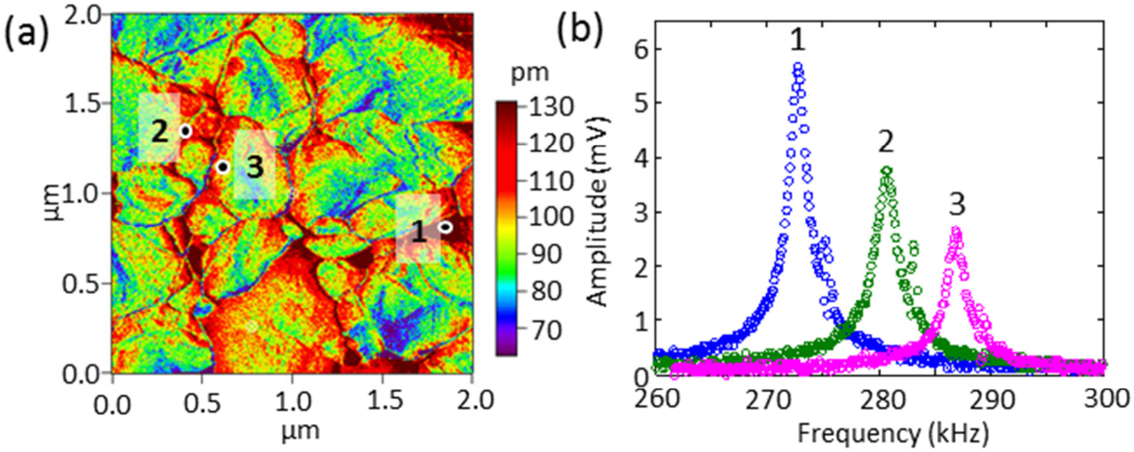

Figure 3.5: (a) ESM scan of a 2 µm by 2 µm area of LiFePO4, with three locations marked (b) amplitude vs frequency plots for the three marked locations.

There are two main methods by which mappings of amplitude and phase can be performed using resonance enhancement to increase the signal-to-noise ratio. The first, by which Figure 3.5(a) was generated, is termed dual amplitude resonance tracking, or DART, and was developed by Rodriguez and group and licensed by Asylum Research [111, 112]. This method, as depicted schematically in Figure 3.6, sums two excitation voltages with frequencies on either side of resonance and sends this signal to the cantilever.

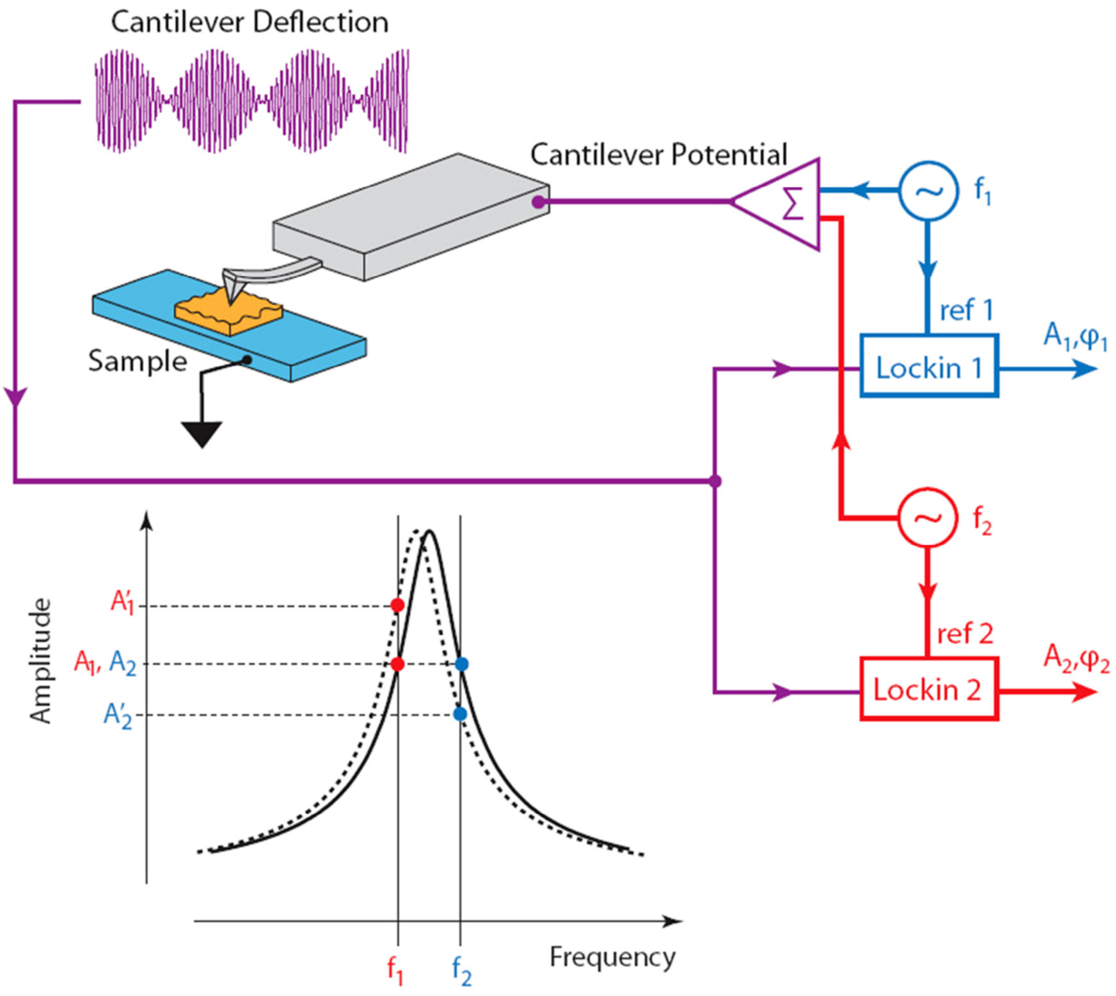

Figure 3.6: Schematic of Dual AC Resonance Tracking method for ESM [111]

The resulting surface vibrations are sent to lock-in amplifiers referenced to the two frequencies, and the amplitude and phase at each frequency is extracted. The difference between the two amplitudes is used for feedback control. This allows the resonance frequency to be tracked as it shifts during scanning. From the two amplitude and two phase values extracted, equations (3.1) and (3.2) can be solved for the drive amplitude and phase, as well as quality factor and resonant frequency [112]. This technique allows for fairly quick mappings of amplitude and phase while maintaining contact resonance. However, over rough surfaces, the resonance tracking can fail, in the sense that the two frequencies applied are no longer on either side of the actual resonant frequency. Furthermore, since the full shape of the response-frequency curve is not measured, quantitative calculations of damping in the system are limited.

Another approach to tracking resonance frequency is to apply biases across a band of frequencies that encompass all of the resonance frequencies over the region of interest, and then extract the intrinsic amplitude and phase during post-processing. This technique is termed band excitation, and was developed in Kalinin's group at Oak Ridge National Lab [113, 114]. Figure 3.7 presents a schematic of this method.

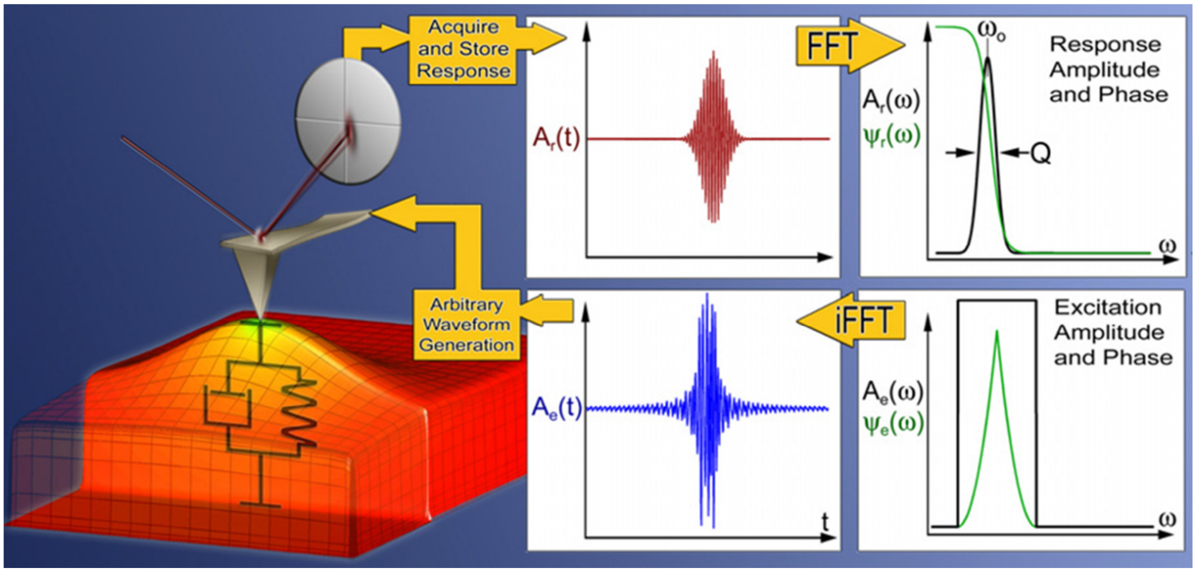

Figure 3.7: Schematic of band excitation, showing the process by which bias across a band of frequencies is applied to a sample [114].

As the schematic shows, from the lower right, a signal in the frequency domain, with a defined amplitude and phase in a band around the resonant frequency, is inverse Fourier transformed into a time signal and sent to the SPM cantilever. The measured response is Fourier transformed and fitted with the driven damped harmonic oscillator model to obtain amplitude and phase in the frequency domain. This technique allows for quantitative analysis of surface amplitude and energy dissipation, essentially eliminating the issues that arise with topographic crosstalk. However, since lock-in amplifiers are not used in this method, the signal-to-noise ratio is inherently lower during operation of band excitation compared to single-frequency or dual-frequency methods.

The ESM work presented in this dissertation will make use of all of the different methods described here to measure the intrinsic amplitude and phase of the material of interest. These methods include not only DART and BE, but also the measurement of amplitude and phase as a function of frequency at single points over a grid, which is time consuming but can lead to greater insights into the underlying mechanisms of the material.

3.3 Phase Determination

One of the major tools used in strain-based scanning probe microscopy is the application of AC voltages to a conductive scanning probe microscope (SPM) probe in contact with a material that demonstrates strain deformation due to the applied voltage. The oscillating strain deformation is measured by the SPM probe through a laser spot reflecting off the probe cantilever and onto a photodiode. This signal passes through a digital lock-in amplifier, from which amplitude and phase can be calculated [115]. The phase signal is of particular interest for PFM and ESM, as it establishes whether the material of interest expands or contracts when subjected to bias. A simplified schematic of the phase lag as defined in this context is presented in Figure 3.8.

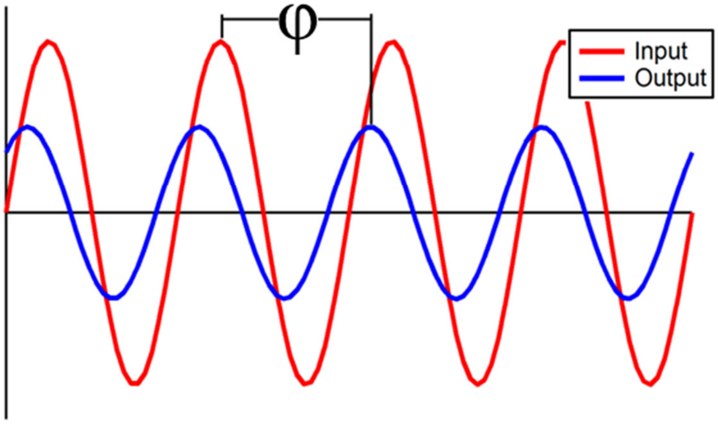

Figure 3.8: Schematic of phase lag between the input signal, which is the bias sent to the cantilever by the direct digital synthesizer (DDS), and the output signal, as measured through a laser-photodiode system and sent to a lock-in amplifier.

However, the phase lag between the input voltage and the response is also influenced by instrumental phase lags in the system. Furthermore, close to the cantilever-sample resonance frequency, the phase undergoes a 180° reversal, since it behaves in accordance to a damped drive harmonic oscillator model, as shown in Figure 3.4. The majority of experiments performed in strain-based scanning probe microscopy take place at the cantilever-sample resonance frequency to increase the signal to noise ratio, making the determination of phase during the course of normal operating difficult. The determination of the true phase lag within the material requires eliminating the contributions of these other factors, which is the object of this portion of the research project.

The first part of this project lies in establishing the instrumental phase lags in the system. To measure the phase lag due to the lock-in calculation, the direct digital synthesizer (DDS) is routed directly to the digital signal processor, and the phase difference can then be measured. This phase lag is listed in Table 3.1 as the lock-in phase lag. Next, to include the external circuitry, the DDS is routed to the high voltage amplifier, which sends the signal to the sample holder containing the high voltage source, as pictured in Figure 3.9. During normal measurements, this SPM probe would be connected to the high voltage source. However, for this measurement, the high voltage source is routed to the digital signal processor, and the phase difference is listed in Table 3.1 as the total instrument phase lag. This phase lag is higher than the one contributed by the lock-in alone, indicating that the hardware plays a significant role in the overall phase lag.

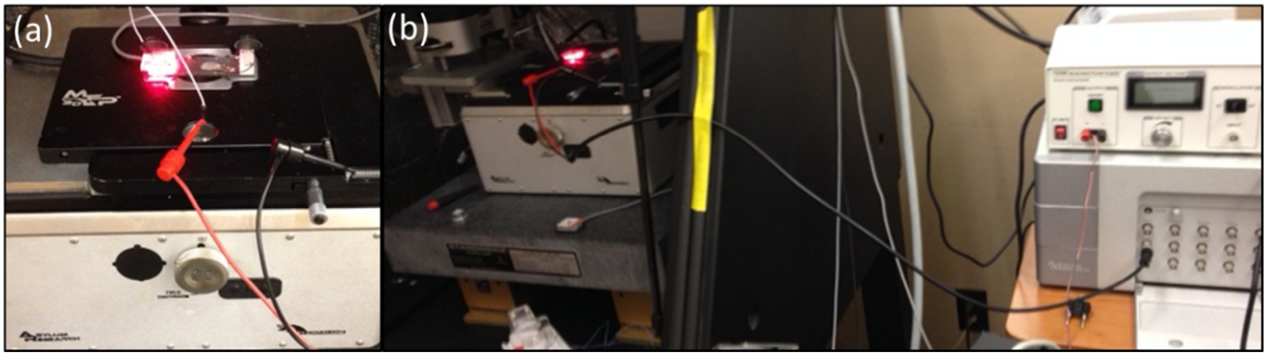

Figure 3.9: (a) High voltage source, with wire connecting out of it, and (b) Wire connecting high voltage source to BNC Input 1 on controller.

The measured phases from both sets of experiments are dependent on the frequency of the input signal. For both sets of experiments, an AC bias of 1 V was applied at the specified frequency.

Frequency	Lock-in Phase Lag	Total Instrument Phase Lag
10 kHz	2°	2°
50 kHz	10°	13°
100 kHz	20°	27°
200 kHz	40°	60°
300 kHz	60°	90°

Table 3.1: Phase lag due to the lock-in calculation and overall phase lag, as a function of frequency

As the data indicates, the phase lag increases linearly with frequency, both in the lock-in calculation as well as in the total instrument lag. This can be seen more clearly in a plot of the phase lag versus frequency, as in Figure 3.10.

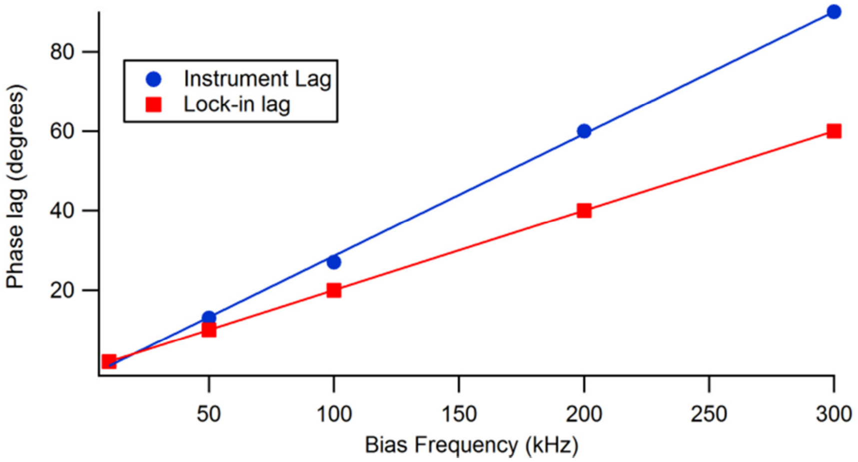

Figure 3.10: Instrument and lock-in phase lags as a function of applied frequency, along with linear fits.

This is a clear indication that there is a constant lag in the time domain from the lock-in calculation and the hardware contribution, since phase is linearly related to frequency when a constant time constant is provided, as equation (3.3) shows.

$$\Delta\varphi = f \cdot \Delta t \cdot 360° \tag{3.3}$$

The measured instrument lag as described leaves out an important additional source of delay inherent in the measurement system: the cantilever-laser-photodiode system. Since there is no simple way to independently measure these lags, it became apparent that a calibration material was needed. Thin-film ferroelectric materials were chosen, because they can be poled using DC voltages to have regions of known polarization on the surface of the material. Two specific systems were chosen: polyvinylidenefluoride-co-trifluoroethylene (PVDF-TrFE) and lead zirconate titanate (PZT), both of which were synthesized through solution-based methods and spin-coated onto platinum-coated silicon wafers and annealed [116, 117]. Regions of the thin films were polarized in a square pattern using a conductive cantilever to apply large DC biases, as shown schematically in Figure 3.11(a). For the PVDF-TrFE sample, +/- 40 V was applied to polarize the region, while for the PZT sample, +/- 10 V was applied. The region was then scanned using piezoresponse force microscopy to verify that two separate domains were formed, as depicted as phase contrast images in Figure 3.11(b) for PVDF-TrFE and Figure 3.11(c) for PZT. In the images presented, only the relative phase differences between the two regions are significant, as the absolute value contains multiple components as previously described, and are typically offset so that the measured response are between -90° and 270°.

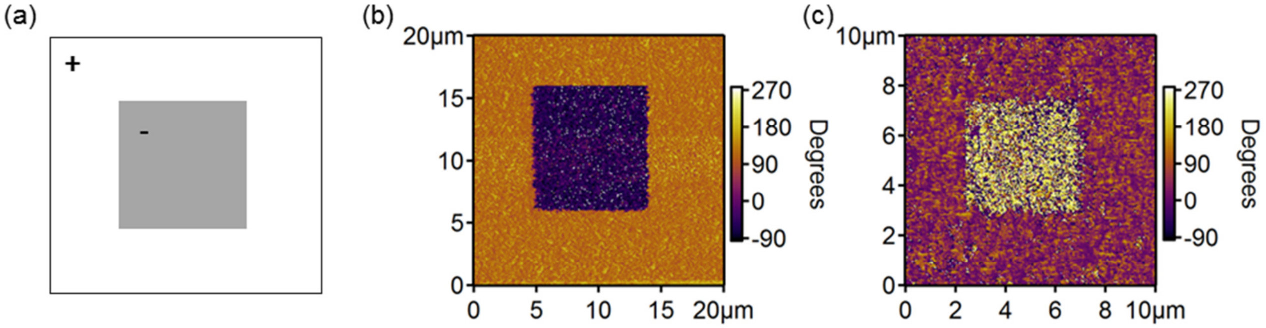

Figure 3.11: (a) Schematic of DC voltage application, with +/- 40 V for PVDF-TrFE and +/- 10 V for PZT, (b) phase mapping of PVDF-TrFE after voltage application, and (c) phase mapping of PZT after voltage application.

As Figure 3.11(b) and (c) indicate, the DC biasing process created two separate domains with a 180° phase difference between the two. In order to determine the true inherent phase lag in the material, phase was measured as a function of frequency at individual points in both domains for both systems. Since phase scales linearly with frequency, it is beneficial to perform the measurements at relatively low frequencies, far away from the cantilever-sample resonance frequency. An example of the phase measurement at low frequencies is shown in Figure 3.12.

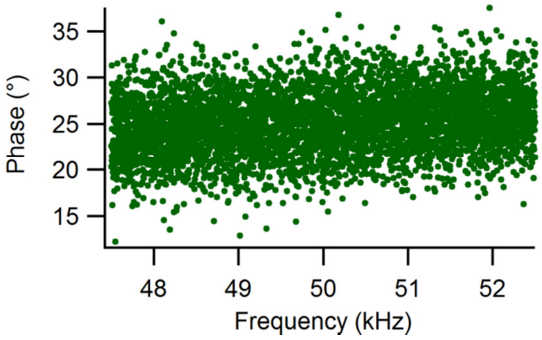

Figure 3.12: Example of phase measurement away from resonance frequency

Many more data points were collected than usual measurements of this type in order to capture a more accurate data set. For a data set as presented in Figure 3.12, an average and standard deviation of phase is calculated, and the results are displayed versus the center frequency in the data set, in this particular case, 50 kHz. A major limitation of this particular experiment is that the poled regions are only stable for a limited amount of time, thus only a few points for each sample was measured for its inherent phase before the region must be again polarized. However, this experiment has proven to be repeatable and thereby can be used to determine intrinsic phase.

The phase results for PVDF-TrFE are presented in Figure 3.13, showing the results for four points, two in each domain.

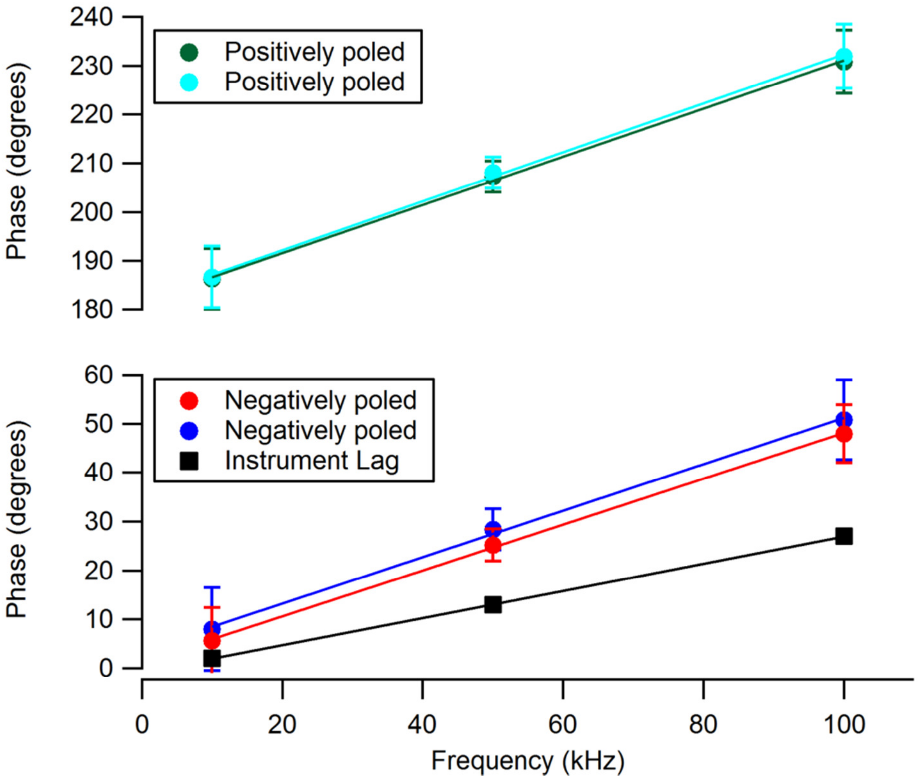

Figure 3.13: Phase lag as a function of frequency for PVDF-TrFE in positively and negatively poled domains.

Because PVDF-TrFE is a material with a negative piezoelectric coefficient [118], positively poled regions are expected to have a 180° phase lag, while negatively poled regions are expected to have a 0° phase lag. As Figure 3.13 indicates, the measured phase lag, even at low frequencies, has additional contributions other than the inherent phase lag. Additionally, the instrumental phase lag is plotted alongside the results for PVDF-TrFE. This measured instrument lag includes phase lag from the lock-in calculation and some of the hardwire connections, but does not include the laser spot - photodiode system. The additional phase lag seen in PVDF-TrFE indicates that this laser spot – photodiode system may be a major contributing factor to the additional lag.

This experiment was repeated using PZT, which has a positive ferroelectric coefficient, and should show intrinsic phase behavior the exact reverse of that in PVDF-TrFE. This particular synthesized material was slightly less stable after poling compared to PVDF-TrFE, so only one point from each location was selected. As Figure 3.14 depicts, measurement of phase in positively poled domains in PZT show phase values that are close to the expected 0°, but offset by phase lag in the system, while the negatively poled domains in PZT show phase values close to the expected 180°.

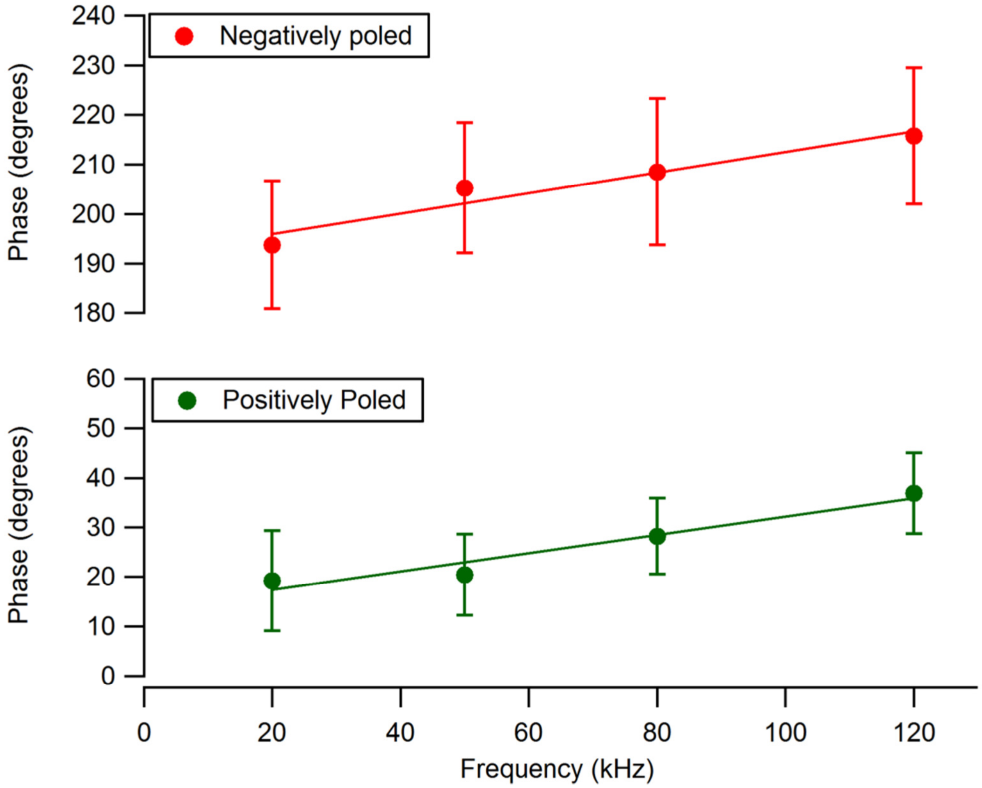

Figure 3.14: Phase lag as a function of frequency for PZT in positively and negatively poled domains.

This technique is valuable for determining whether the material is expanding or contracting with a positive bias, but the phase determination is not precise enough to account for minor deviations from pure expansion and contraction.

Another consideration during the study of phase lag is the influence of cantilever dynamics. For much of the research associated with scanning probe microscopy, the cantilever bending behavior at a single location, typically at the end of the cantilever, is monitored using a laser spot – photodiode system. However, the overall cantilever vibrational shape during operation can have a significant influence on the amplitude and phase measured. From Asylum Research's work on periodically poled lithium niobate [119, 120], it appears that long-range electrostatic interactions and small changes in contact stiffness in the sample can alter the shape of the cantilever from its theoretical behavior. These effects can occur even at frequencies below the cantilever-sample resonance frequency, causing contrasts in measured phase based on the position of the laser spot on the cantilever holder. Although the frequencies used in these experiments tend to be well below the reversal frequencies measured by Asylum Research, it is important to eliminate this possible source of phase lag. From their work, it appears that the reversal in phase behavior occurs at much higher frequencies when the laser spot is away from the end of the cantilever. The previous set of experiments were repeated with the laser spot moved from its original position at the tip of the cantilever to a location close to half-way down the length, as schematically depicted in Figure 3.15. If a phase reversal does occur, the phase results from measurements taken with the laser at the shifted spot would be different than the phase results taken with the laser at the end of the cantilever.

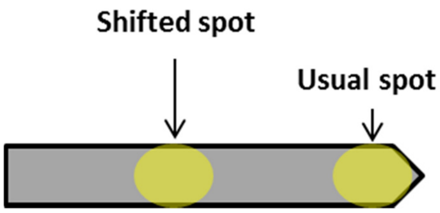

Figure 3.15: Schematic depiction of laser spot position on SPM cantilever

The laser spots in Figure 3.15 are represented by large circular shapes due to the resolution of the optical microscope, and are not representative of the actual laser spot. The Asylum Research experiment was performed on a Cypher system with a much more powerful optical microscope that can more precisely locate the laser spot on the cantilever. However, the parameters of this experiment are sufficient to determine if there is a phase change when the laser spot is shifted.

With the laser spot adjusted to the new position halfway down the length of the SPM cantilever, a series of phase measurements were performed in positively and negatively poled regions of PVDF-TrFE, following the exact same procedure as with the previous set of experiments. The results are plotted in Figure 3.16(a) along with a set of results taken with the original laser spot location. Here, 80 kHz was used for the third frequency due to unexplained amplitude peaks at 100 kHz which may skew the data.

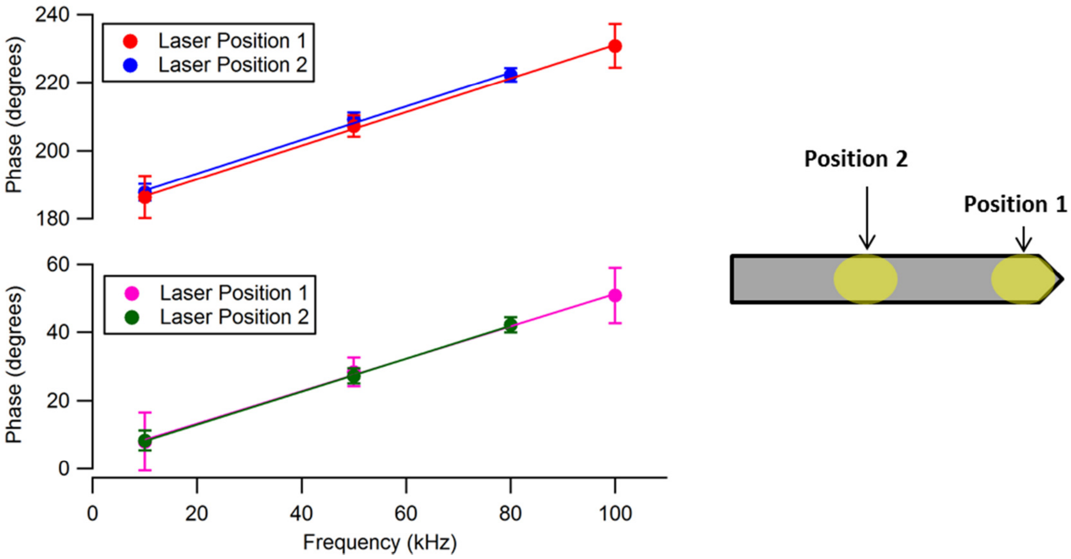

Figure 3.16: Phase lags in positively and negatively poled regions, using two different laser positions.

As Figure 3.16 depicts, the phase lags with the laser spot shifted are virtually identical to phase lags from the original and more commonly used laser spot. This result indicates that the experiments described in this section are not affected by a possible phase reversal, and can be used definitely to calibrate materials for which the intrinsic material phase lag is unknown. One such material, samarium doped ceria (SDC), was measured and compared to negatively poled domains of PVDF-TrFE, which has an intrinsic material phase lag of 0°.

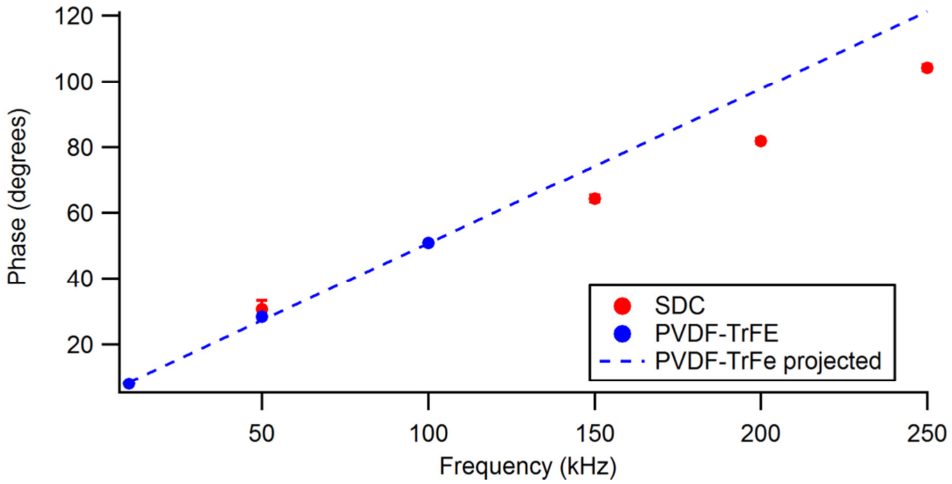

Figure 3.17: Phase lag in samarium doped ceria, plotted with PVDF-TrFE for comparison.

As Figure 3.17 shows, the phase lag in SDC is very similar to the phase lag in negatively poled domains of PVDF-TrFE, indicating that it also has a 0° phase lag, which means that it expands under a positive bias. The implications of this result lead to a hypothesis regarding the underlying mechanism of bias-induced strains observed during electrochemical strain microscopy experiments of samarium doped ceria, which are discussed in Chapter 5.

3.4 First and Second Harmonic Responses in Vertical and Lateral Measurement Modes

For the most part, when discussing strain-based scanning probe microscopy experiments, the assumption is that the measured strain changes are linearly related to the applied AC biases. Essentially, the applied bias, when only an AC component is present, can be expressed as:

$$V_{tip} = V_{ac}\cos(\omega t)$$

The surface response contains not only a corresponding linear response, but also responses at higher harmonics. The amplitude can be expressed as:

$$A = A_1 cos(\omega t + \varphi_1) + A_2 cos(2\omega t + \varphi_2) + A_3 \cos(3\omega t + \varphi_3) + \cdots$$

During the normal operation of bias-induced strain microscopy experiments, the measured amplitude is filtered through lock-in amplifiers, which use the frequency of the applied bias as a reference [115], extracting out the first harmonic amplitude and phase. However, higher harmonic responses can lead to greater insights to the nature of the material. For example, electrostrictive, joule heating, and electrostatic effects are typically second harmonic responses to applied voltage [67, 121, 122]. Recent research in this area has used the analysis of these higher harmonic responses to study ferroelectric nanocapacitors [123, 124], in which the linear response, corresponding to ferroelectricity, can be separated from the quadratic response, corresponding to Joule heating effects arising from leakage currents. In this project, the difference between first (linear) and second (quadratic) harmonic responses are applied to a number of different materials with the goal of distinguishing among the different mechanisms that are responsible for observed SPM strains.

In the research performed by Kalinin's group at Oak Ridge National Laboratory, the second harmonic response was measured through a technique termed half-harmonic band excitation, a schematic of which is presented in Figure 3.18.

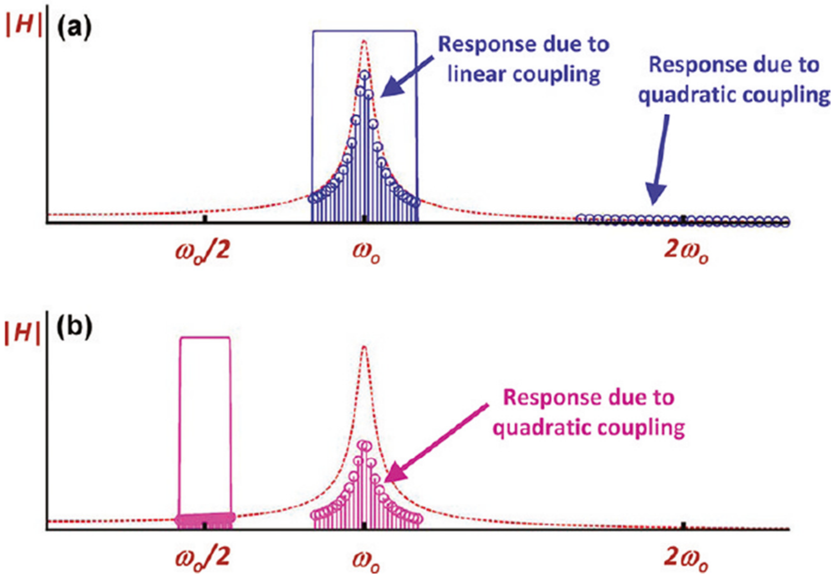

Figure 3.18: Schematic of operational principle of (a) first-harmonic and (b) half-harmonic band excitation [124]

The principles of band excitation were covered in Chapter 1 of this dissertation, but essentially the signal applied to the cantilever consists of a band of frequencies with a constant amplitude, and the response is measured and fitted with the damped driven harmonic oscillator model to obtain amplitude and phase values [114]. In the first harmonic operation, the input and output signals lie in the same frequency range, close to the cantilever-sample resonance frequency. In the half-harmonic band excitation method, the input signal is applied at half the resonance frequency, while the output signal is monitored at the resonance frequency, thereby measuring the quadratic response while still using the cantilever-sample resonance enhancement to increase the signal-to-noise ratio.

In the AFM system used over the course of this research project, implementation of the band excitation technique is not yet sufficient to perform the range of experiments necessary to characterize the materials of interest. The method used instead for most experiments was a dual amplitude resonance tracking (DART) technique [112], which is also covered in more detail in Chapter 1. This technique uses two frequencies, one on either side of the resonance frequency, to track the resonance frequency as it shifts over the course of an experiment, utilizing lock-in amplifiers for each frequency. The existence of these two lock-in amplifiers makes it possible for the implementation of a half-harmonic technique to measure quadratic responses. During typical operation, an AC voltage with a specific frequency is referenced to one lock-in, and the output signal is sent to the same lock-in, amplifying the response at the input frequency. The frequency of the AC voltage and the measured response can be swept over a series of values, typically chosen to be close to the cantilever-sample resonance frequency. A typical amplitude versus frequency curve generated through such an experiment is shown in Figure 3.19(a). In order to measure the second harmonic signal, the response is sent instead to the second lock-in, which is referenced to twice the input frequency. The input frequencies are chosen to be close to half of the resonance frequency, so that the response signals are amplified by the cantilever-sample resonance. This second harmonic response is shown in Figure 3.19(b).

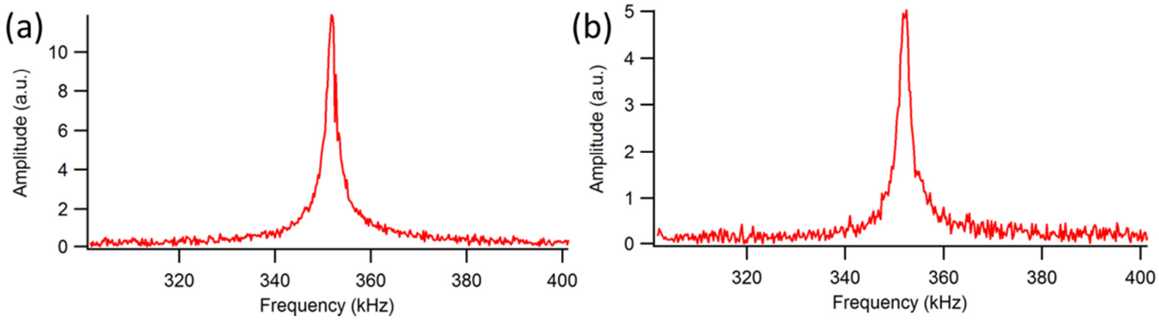

Figure 3.19: Amplitude versus frequency data as a result of biases applied at (a) the frequencies measured and (b) half the value of the frequencies measured.

The measurements in Figure 3.19 were performed on lithium iron phosphate ($LiFePO_4$), a cathode material for lithium ion batteries. In this case, the quadratic response is most likely due to quadratic terms within Vegard strain, and is smaller than the linear response. The difference between quadratic and linear responses can be used to distinguish among different underlying mechanisms that cause field-induced strain responses measured by the SPM.

Recent publications regarding piezoresponse force microscopy on silicon and glass have demonstrated ferroelectric-like strain responses, even though neither material is ferroelectric [108, 109]. However, particularly in soda-lime glass, the measured responses are most likely due to electrostrictive behavior of the dielectric material and electrochemical behavior of the sodium ions at the surface. The ferroelectric and electrostrictive responses can be distinguished by examining the difference between linear and quadratic responses, since piezoelectric strain is linearly related to applied field, while electromechanical strains from electrostriction are quadratic to the applied field. This can be expressed as equation (3.4):

$$\boldsymbol{\varepsilon \propto (P_s + \chi E)^2 = P_s^2 + 2\chi P_s E + \chi^2 E^2} \qquad \textbf{(3.4)}$$

where P_s is the spontaneous polarization, and χE is the induced polarization. For a ferroelectric material, the spontaneous polarization dominates, while for a dielectric material with no spontaneous polarization, the induced polarization terms cause the resulting strain. Correspondingly, for a ferroelectric material such as lead zirconate titanate (PZT), the linear response should dominate, while for a material such as soda-lime glass, the quadratic response should be strong. This behavior is observed experimentally in Figure 3.20.

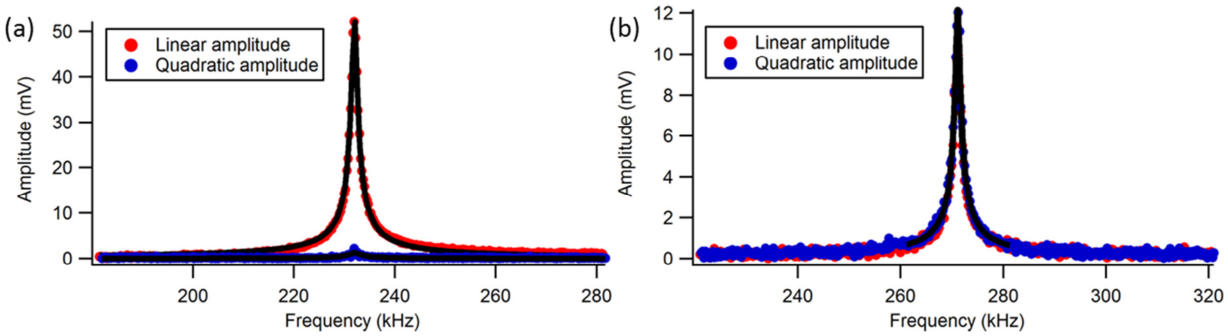

Figure 3.20: Linear and quadratic responses to applied bias for (a) PZT and (b) soda-lime glass

Furthermore, the difference between piezoelectric and electrostrictive responses can be further distinguished by examining the lateral response to applied bias. Up to this point, all of the strain measurements have been made in the vertical direction. However, there is also a lateral component to piezoelectric response, since the domains can be aligned perpendicular to the applied field. The lateral response can be measured as a twisting of the cantilever rather than the bending observed in the vertical response. For dielectric, non-ferroelectric materials, there should not be a significant lateral response, since induced polarization behavior is in the direction of applied bias. Measurements of the linear and quadratic responses in lateral mode for PZT and soda-lime glass are shown in Figure 3.21(a) and (b), respectively.

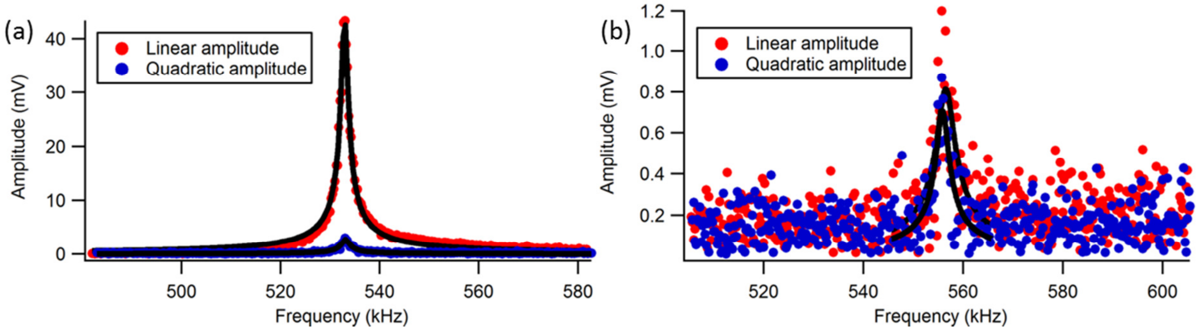

Figure 3.21: Linear and quadratic responses in the lateral direction for (a) PZT and (b) soda-lime glass.

These results demonstrate that the comparison between linear and quadratic responses in vertical and lateral modes can aid in distinguishing between piezoelectric and electrostrictive behavior. However, the examination of second harmonic responses has its limitations with regard to distinguishing among the many different possible mechanisms. For example, lithium iron phosphate also shows strong quadratic responses in both vertical and lateral modes of measurement, as shown in Figure 3.22, albeit with slightly higher linear response compared to the quadratic.

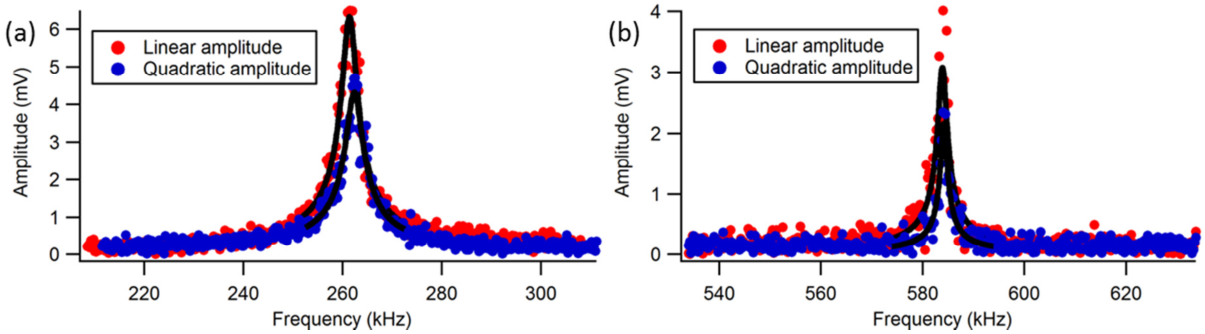

Figure 3.22: Linear and quadratic responses in $LiFePO_4$ in (a) vertical and (b) lateral modes

The quadratic response in $LiFePO_4$ may be the result of a quadratic component to the Vegard strain, but may also have contributions from electrostatic interactions as well. This area of study is of increasing interest to the research community, and may possibly have greater implications in the field of electrochemical strain microscopy.

3.5 Spectroscopic Measurement Techniques

Up to this point, the scanning probe microscopy techniques described have all focused on the application of alternating current (AC) voltages to the sample of interest. The application of direct current (DC) voltages can cause changes in the local state of the material, which can then be detected by application of AC voltages and measurement of the resulting strain changes. For example, the application of large DC biases can switch the local polarization in ferroelectric materials and increase or decrease the local ion concentration in lithium ion electrodes. One particular experiment, involving a triangular sweep of DC bias modulated by square wave signals, is commonly applied to ferroelectric and electrochemical materials. This experiment has been alternately described in publications as switching spectroscopy [125], dynamic ESM [105], among others. For the sake of simplicity, here, the technique will be referred to by the more general term voltage spectroscopy [36], although this is technically a misnomer since it does not strictly involve the interaction between matter and radiated energy. A representation of the waveform applied to the sample is shown in Figure 3.23.

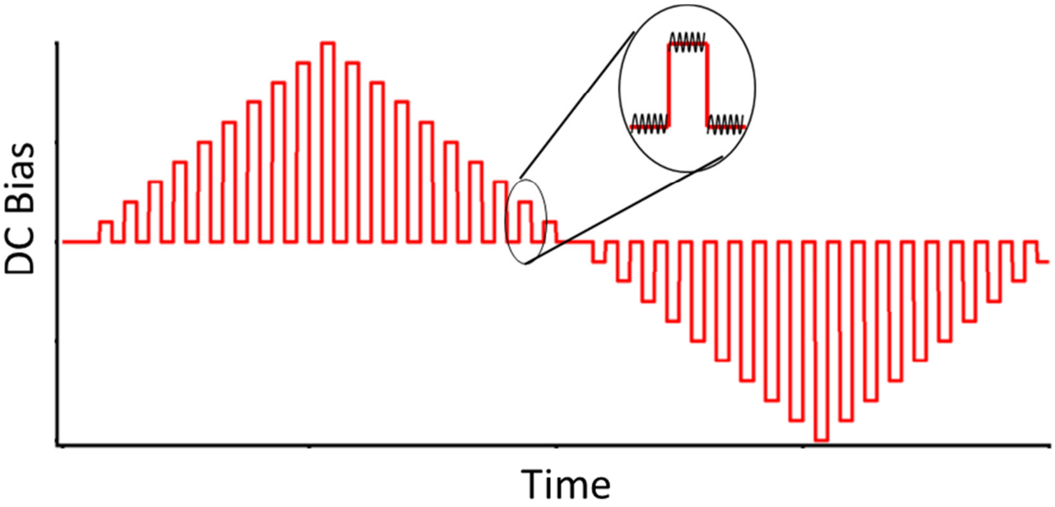

Figure 3.23: Schematic of triangle-square waveform

The triangle-square waveform shown in Figure 3.23 represents the series of DC biases that are applied to the sample through a conductive cantilever. On top of these DC biases, AC biases are applied to measure field-induced strain. When the DC bias is applied, the measured response is dominated by electrostatic effects, which in large part cover up any other responses due to piezoelectricity or Vegard strain. Therefore, the AC response is measured after each DC pulse, in order to characterize the behavior of the material in response to DC stimuli. The amplitude and phase as a response to the DC pulses, plotted in Figure 3.24 for three different classes of materials, differ depending on the underlying mechanism that dominates electromechanical behavior in the given material system.

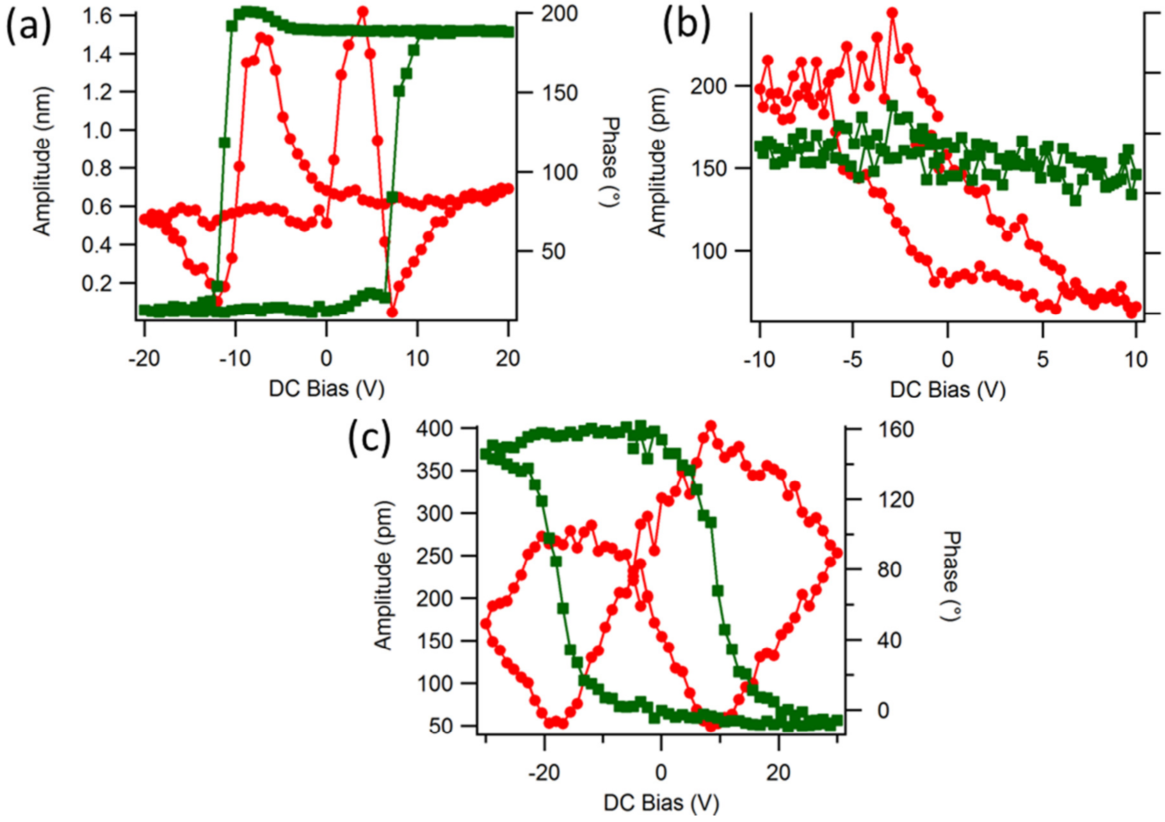

Figure 3.24: Voltage spectroscopy amplitude and phase for (a) PZT, (b) $LiFePO_4$, and (c) soda-lime glass

For ferroelectric materials such as PZT, application of DC voltages past the coercive voltage cause a switching of the polarization, resulting in characteristic butterfly loops in amplitude and hysteresis loops in phase, as shown in Figure 3.24(a). For electrochemical materials such as lithium iron phosphate, application of DC voltages simply manipulates the ionic concentration and correspondingly the magnitude of its strain response, while leaving the phase unchanged, as shown in Figure 3.24(b). Furthermore, its amplitude is anti-symmetric rather than symmetric with respect to DC bias, which is consistent with the compositional dependence of nonpolar Vegard strain. Figure 3.24(c) shows the amplitude and phase response for soda-lime glass, which, unexpectedly exhibits ferroelectric-like hysteresis and butterfly loops, even though it is neither piezoelectric nor ferroelectric. The reversibility of the phase suggests that the strain response in glass is dipolar in nature, and that the electromechanical coupling is related to dipoles induced by ionic motion under external electric field, as proposed by Roger Proksch in a recent publication [108].

In addition to the examination of second harmonic responses described previously, electromechanical behavior arising from ferroelectricity and dipolar electrostriction can also be distinguished by varying the parameters of voltage spectroscopy. The behavior of amplitude and phase as the maximum DC bias applied is increased is different for ferroelectric materials such as PZT compared to amorphous insulators such as glass, as shown in Figure 3.25.

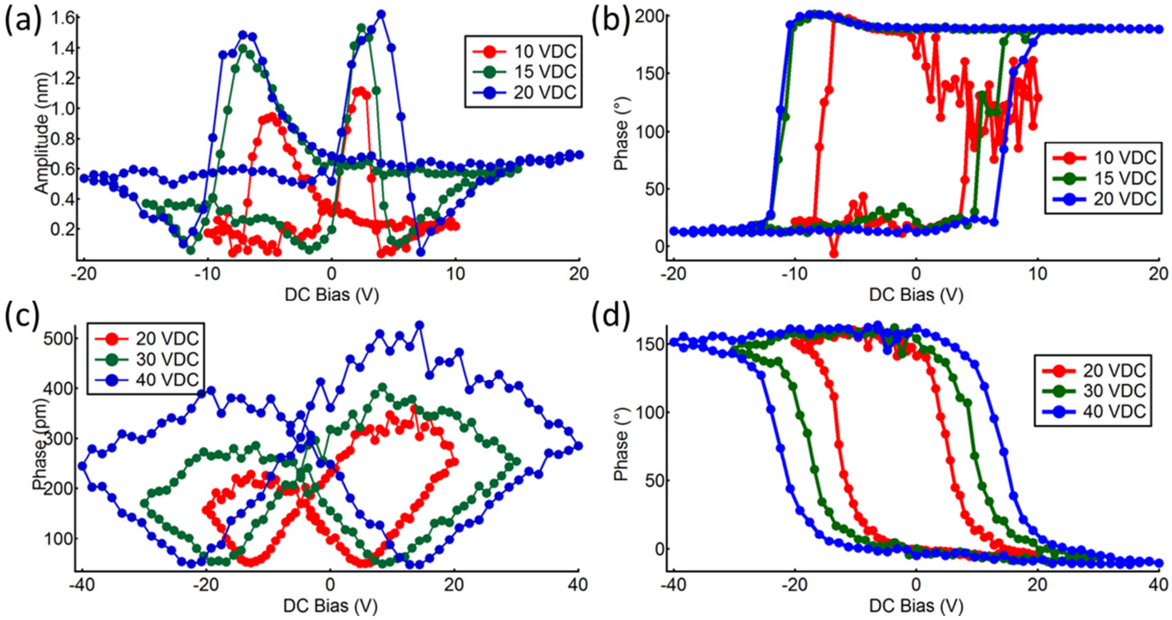

Figure 3.25: Voltage spectroscopy with varying maximum DC biases, showing (a) amplitude and (b) phase responses for PZT, and (c) amplitude and (d) phase responses for soda-lime glass.

For ferroelectric materials such as PZT, the phase hysteresis loop and amplitude butterfly loops do open up as maximum DC voltages increases, up to its coercive voltage, and does not open up further beyond that, as shown in Figure 3.25(a) and (b). For soda-lime glass, however, the electrostrictive response does not show a defined coercive voltage. Higher electric fields induce larger extents of ionic diffusion, and thus the hysteresis response opens up further with increased maximum voltage, as shown in Figure 3.25(c) and (d). In essence, the glass possessed mixed characteristics of both polar and electrochemical systems.

Another parameter that can be altered to differentiate among different mechanisms in voltage spectroscopy is the overall period of the triangular sweep, that is, the total time shown in the schematic in Figure 3.23, which is also the total time it takes to obtain data for a single hysteresis or butterfly loop. For ferroelectric materials, intrinsic polarization is very fast, and essentially time-independent within the parameters of this experiment. As a result, changing the sweep time does not significantly alter the shape of the hysteresis or butterfly loops, as Figure 3.26(a) and (b) show.

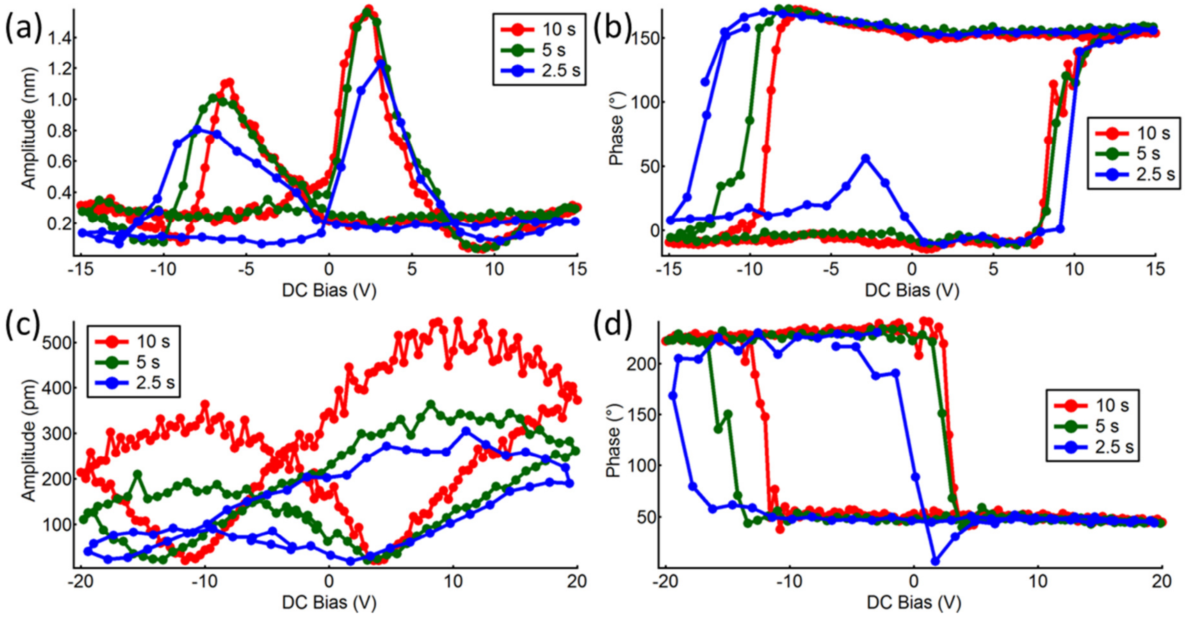

Figure 3.26: Voltage spectroscopy with varying loop times, showing (a) amplitude and (b) phase responses for PZT, and (c) amplitude and (d) phase responses for soda-lime glass.

Since the strain response in glass is dipolar, it is limited by ionic transport, which is much slower than the dynamics of intrinsic polarization. Therefore, decreasing the sweep time causes the butterfly and hysteresis loops to collapse, as shown in Figure 3.26(c) and (d). The use of these voltage spectroscopy techniques adds another method by which the many different mechanisms observed in strain-based scanning probe microscopy can be distinguished.

3.6 Summary

The development of electrochemical strain microscopy and its application to a diverse series of materials has opened up questions about the fundamental nature of the observed behavior. Initial assumptions about measured strain changes being the result of the motion of ions and vacancies have been proved to be incomplete. This section describes a series of experiments that can provide more clues as to the actual mechanisms occurring on the surface of a given material during strain-based scanning probe microscopy measurements. Measurement of the intrinsic phase behavior of the material indicates whether the surface is contracting or expanding with applied bias. Another experiment described was to compare the first and second harmonic responses to applied bias. Since linear and quadratic components arise from different material behaviors, this information provides additional clues as to the underlying mechanisms at play. Similarly, measurement of lateral responses is an indication of the presence of out-of-plane response to an in-plane excitation, which can eliminate certain sources of signal, such as electrostatic interactions.

Voltage spectroscopy techniques have been applied to great effect in ferroelectrics for many years. However, the hysteretic behavior of non-ferroelectric materials such as soda-lime glass and silicon has recently become a mystery. Through varying experimental parameters such as the voltage sweep period and the maximum DC bias applied, significant differences between ferroelectric and non-ferroelectric behavior can be illuminated. This technique can be used to even greater effect if it can be combined with second-harmonic measurements, in order to examine the behavior of mechanisms that respond as a function of the field squared. The development of second-harmonic voltage spectroscopy requires customization of the AFM software, and will be pursued in the near future.

4 Electrochemical Strain Microscopy of $LiFePO_4$

4.1 Motivation

Researchers in the field of energy storage have increasingly turned to nanostructured materials to increase capacity and cyclability beyond the theoretical limit of bulk materials [16, 17, 126]. However, the exact mechanisms responsible for this enhancement are not yet fully understood, and techniques to study lithium-ion batteries at nanoscale are crucial to furthering the understanding of nanostructured systems. In the previous chapters, electrochemical strain microscopy (ESM) was discussed as a promising technique that can directly study lithium ion distribution and diffusion in electrode and electrolyte materials. The local strain changes detected using this method is due to the oscillation of lithium ion concentration induced by a conductive scanning probe microscope tip. ESM analysis of electrode materials makes it possible to correlate local electrochemical activities of lithium ion electrodes at nanometer scale with topographical morphology as well as macroscopic battery performance at device level, and thus can help to pin down the mechanisms responsible for performance enhancements often observed in nanostructured electrodes.

This technique is applied to study the properties of inhomogeneous lithium iron phosphate ($LiFePO_4$). $LiFePO_4$, due to its olivine structure, allows reversible intercalation and extraction of lithium ions through one-dimensional channels. For larger particles, however, capacity becomes limited when the channels become blocked by Li/Fe disorder or stacking faults [60]. Furthermore, it has been proposed that lithium ion insertion occurs as a two-phase reaction, which limits electronic and ionic conductivity, particularly when the particles are large [127, 128]. Electrochemical strain microscopy can be used to directly compare lithium ion motion on lithium iron phosphate particles of varying sizes, and is applied here on an inhomogeneous lithium iron phosphate system. The first set of experiments was performed using an Asylum MFP-3D atomic force microscope, using the dual amplitude resonance tracking (DART) technique. Later, a series of experiments were performed at Oak Ridge National Laboratory as part of a user proposal, using band excitation to study $LiFePO_4$ electrodes. In conjunction with these experiments, a collaborator, Chihou Lei, developed an analytical model for ESM on lithium-ion electrodes. Using values calculated from his model, experimental data could be quantitatively fitted in order to estimate the diffusivity of lithium ions at the surface of $LiFePO_4$. These results suggest that ESM can be applied to quantitatively determine fundamental properties of lithium ion electrodes at nanoscale.

4.2 Fabrication of $LiFePO_4$ samples

The samples of $LiFePO_4$ used in the first set of experiments were fabricated by Yanyi Liu from Professor Guozhong Cao's sol-gel group in Materials Science, with a synthesis procedure modified from previously published work [99]. The precursor solutions were prepared by combining lithium hydroxide monohydrate, ferric nitrate, phosphoric acid, and L-ascorbic acid $C_6H_8O_6$ with a molar ratio of Li:Fe:P:ascorbic acid of 1:1:1:1. The ingredients were added to deionized water at a concentration of 1 mol/L and heated at 60°C for 1 hour on a hot plate to fully dissolve the ascorbic acid. After allowing the solution to cool, a small amount was further diluted to 0.01 mol/L. The undiluted solution was ground up for x-ray diffraction in order to confirm the crystal structure of the synthesized material. The results of the x-ray diffraction experiment are shown in Figure 4.1, with the red lines indicating standard peaks for the olivine lithium iron phosphate.

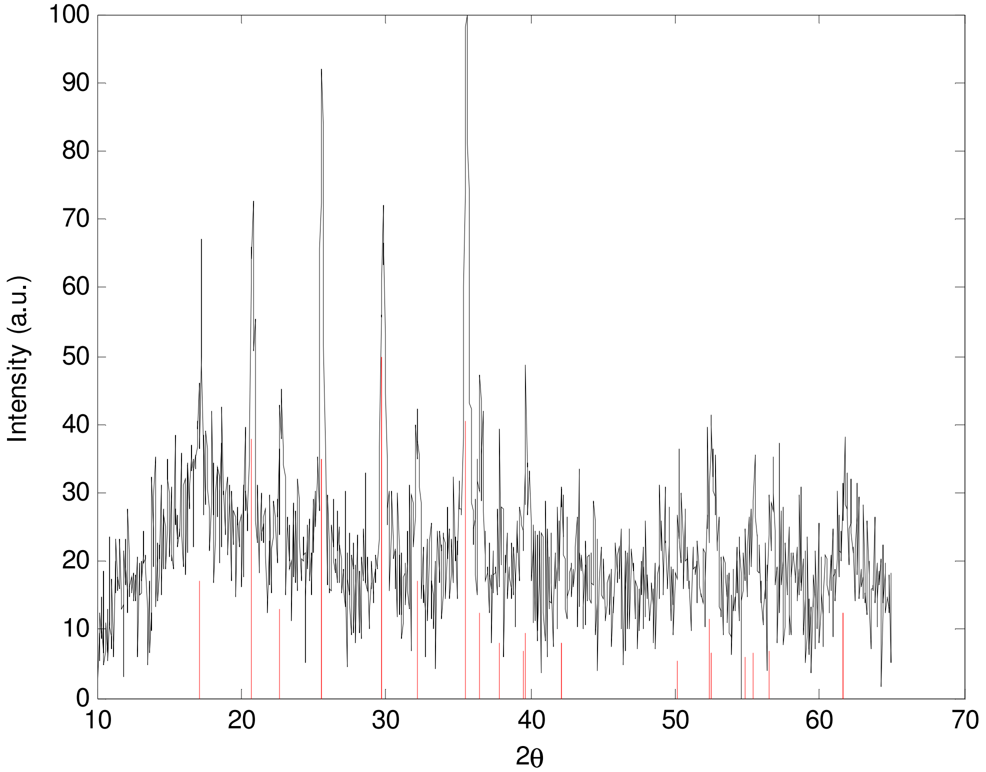

Figure 4.1: X-ray diffraction of concentrated lithium iron phosphate powder

The solution that had been diluted to 0.01 M was used to fabricate electrodes by drop-casting 50 μL onto Ti-foil. Films were annealed at 600°C for 3 hours in N_2 gas. The resulting lithium iron phosphate material was imaged using scanning electron microscopy (SEM), as shown in Figure 4.2.

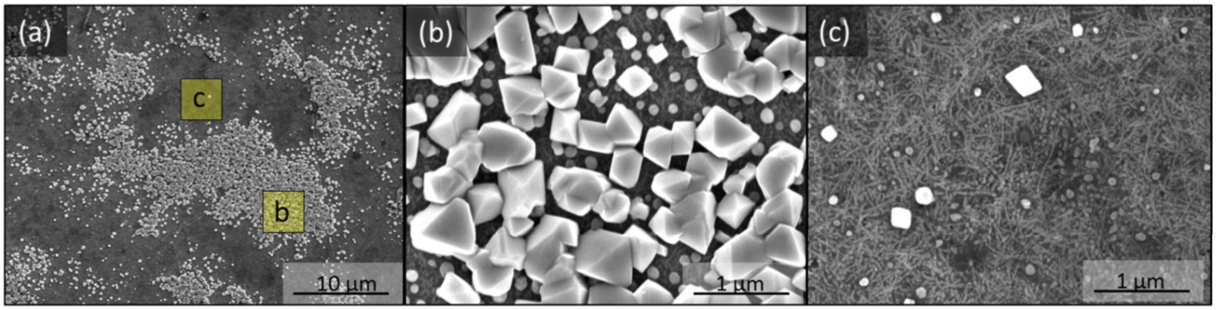

Figure 4.2: Scanning electron microscope images of lithium iron phosphate, with a larger area shown in (a), and smaller areas highlighted and shown as (b) and (c).

As the SEM images illustrate, the resulting film is inhomogeneous, with areas that show very crystalline morphology with particles on the order of 500 nm – 1 µm, as shown in Figure 4.2(b) and areas that show evidence of much smaller particles, as shown in Figure 4.2(c).

One of the prepared samples was directly used in electrochemical strain microscopy experiments, after attaching the foil to a thin stainless steel disk using epoxy. The edges of the Ti foil were coated with silver paint to ensure a conductive path between the steel disk and the sample. Figure 4.3 shows photographs of the lithium iron phosphate electrode during the preparation process for electrochemical strain microscopy.

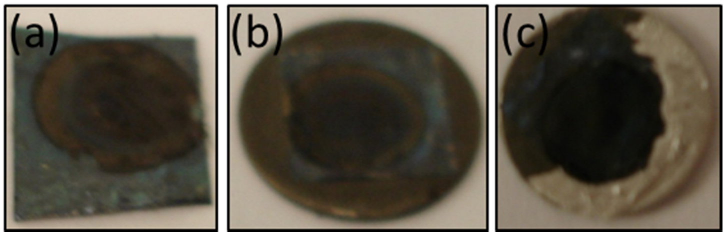

Figure 4.3: Lithium iron phosphate sample (a) after annealing, (b) adhered to a steel disk, (c) coated with silver paint.

Two other samples were prepared and assembled into electrochemical test cells using a lithium metal foil as anode, Celguard 2400 microporous film as separator, and electrolyte composed of 1 M $LiPF_6$ dissolved in a mixture of ethylene carbonate and dimethyl carbonate at a volume ratio of 1:1. One of the samples was charged to a potential of 4.2 V vs. lithium metal, while the other sample was charged to 4.2 V and then discharged to 2.0 V; both the charging and discharging processes were carried out at a rate of 1 C. The charge/discharge curves are shown in Figure 4.4.

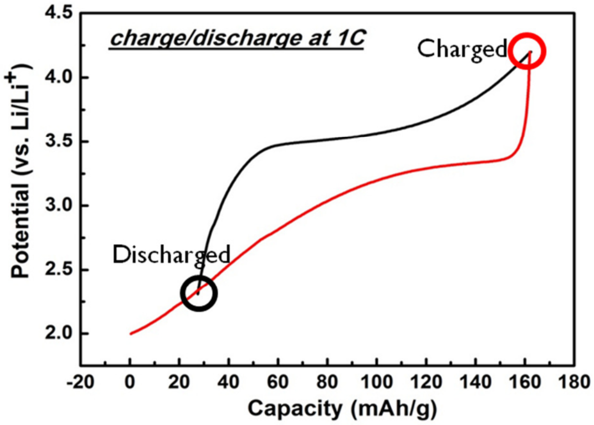

Figure 4.4: Charge and discharge curve for lithium iron phosphate

Additional samples were prepared for the band excitation studies at Oak Ridge National Lab. The synthesis procedure was identical to the one described above, except that they were fabricated by the author of this dissertation. The substrates used were thin pieces of titanium metal (99.7% pure, 0.25 mm thick, Sigma Aldrich). Scanning electron microscope images of the thin films are presented in Figure 4.5, also showing different morphologies in different regions of the sample.

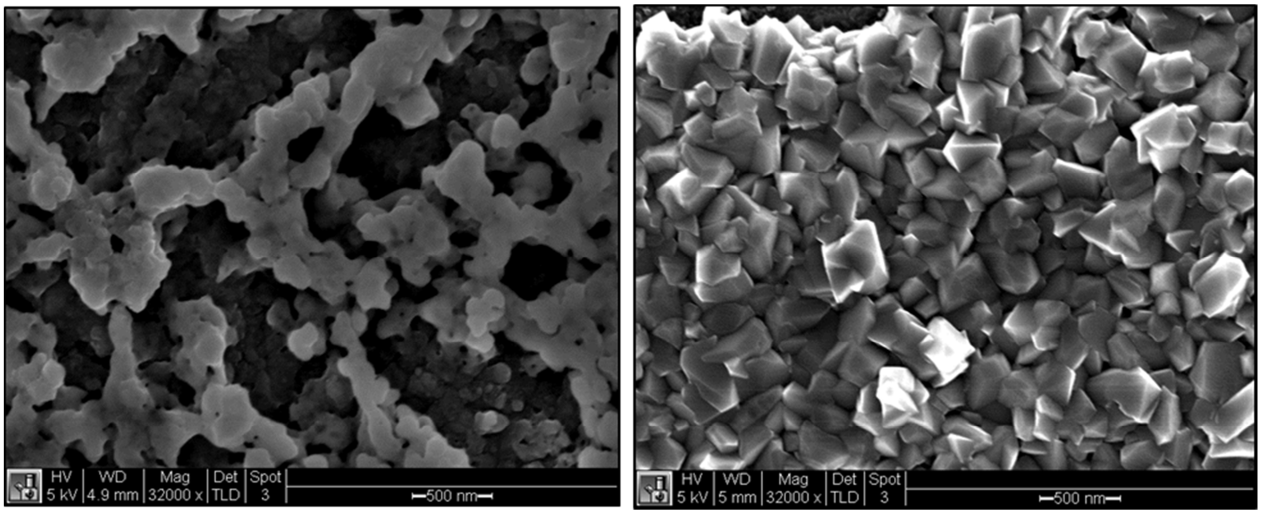

Figure 4.5: SEM images of $LiFePO_4$ thin films on titanium substrates. Both images were taken from the sample sample, but in different regions.

One sample was kept for ESM testing as an as-processed sample, while two other samples were assembled into coin cell batteries with lithium metal as the anode. One of these samples was charged before being disassembled from the coin cell, and the other one was charged and discharged prior to disassembly. The charge and discharge curves for the tested $LiFePO_4$ samples are presented in Figure 4.6.

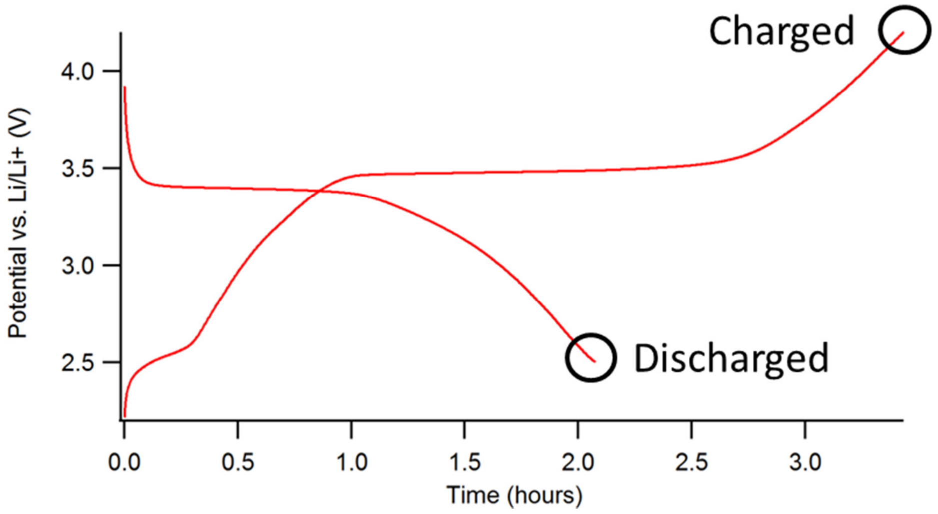

Figure 4.6: Charge and discharge curves for $LiFePO_4$ on titanium substrates

There was a major problem with the samples prepared for band excitation experiments. The electrodes were assembled into coin-cell type batteries that were not very stable at the charged and discharged states indicated in Figure 4.6. As a result, by the time the electrodes were disassembled from the coin-cell batteries, the potential of the cell had shifted from its fully charged or fully discharged states. Therefore, it is difficult to conclusively evaluate the lithiation state of the electrodes tested.

4.3 Electrochemical strain microscopy with DART

As was previously described, the $LiFePO_4$ samples studied were inhomogeneous in terms of morphology, which make them convenient samples due to the presence of particles of different sizes in a single specimen under otherwise identical conditions. This allows for the ability to correlate local lithium ion motion with morphology and macroscopic battery performance. Figure 4.7 shows contact-mode atomic force microscopy images of the two different types of morphologies.

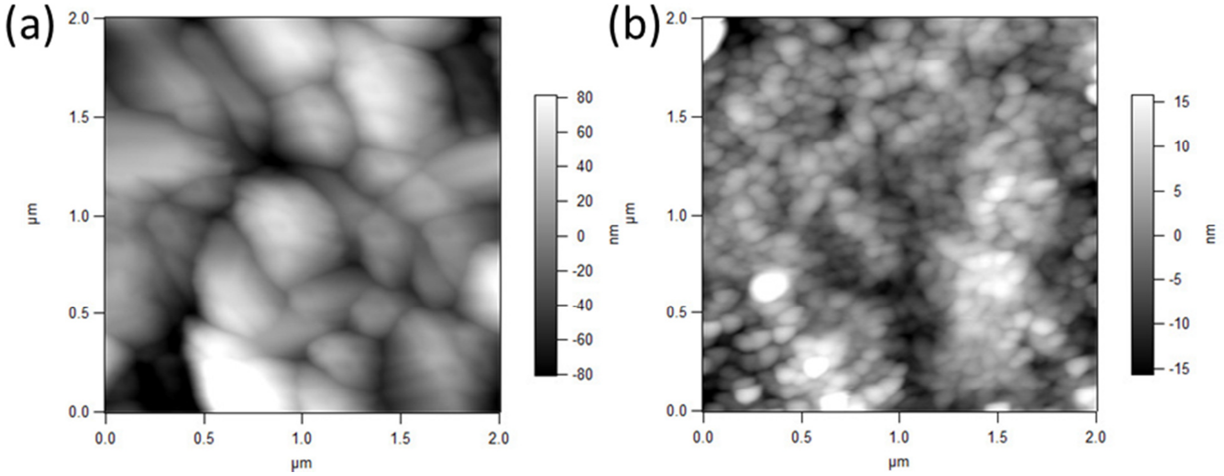

Figure 4.7: Contact mode atomic force microscopy of $LiFePO_4$ sample showing two different morphologies

Electrochemical strain microscopy was performed on both types of morphologies, which from here on will be referred to as microcrystalline for the regions with micron-sized particles and nanocrystalline for regions with nanosized particles. For all of the experiments, ESM was performed using the dual amplitude resonance tracking (DART) technique, described in more detail in Chapter 3. The data presented was calculated from the experimentally collected data using a damped driven harmonic oscillator model. Figure 4.8 is an example of the data collected from ESM overlaid on topography.

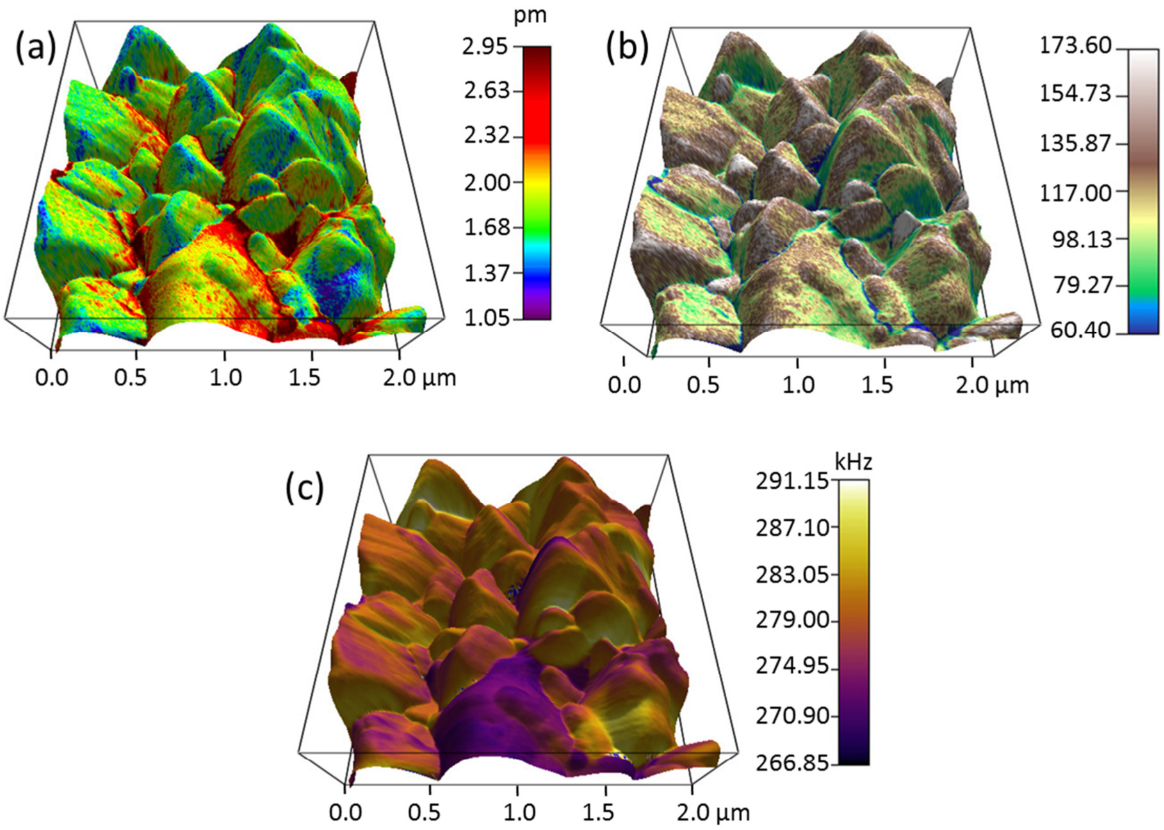

Figure 4.8: (a) Amplitude overlaid on topography, (b) quality factor overlaid on topography (c) resonance frequency overlaid on topography

Figure 4.8(a) shows the drive amplitude overlaid on the topography, while Figure 4.8(b) shows the quality factor, a measure of energy losses in the system, and Figure 4.8 (c) shows the resonant frequency, which is primarily a function of the topography.

In order to understand the electrochemical implications of the ESM response, the transport of lithium ions in electrodes is examined with more detail. While the dynamics and kinetics of lithium ion intercalation and extraction in $LiFePO_4$ is very complicated and not yet well understood, for small perturbations under SPM induced electric field, the assumption is made that the redistribution of lithium ion concentration *n* is governed by diffusion driven by concentration gradient and electro-migration driven by electric field gradient [129],

$$\frac{\partial n}{\partial t} = \nabla \cdot (\boldsymbol{Dn}) + \nabla \cdot \left(\frac{DzFn}{RT}\nabla\boldsymbol{\varphi}\right) \quad \textbf{(4.1)}$$

Here, the first term is the diffusion contribution, with *D* representing the diffusion coefficient, and the second term is the electro-migration contribution. Under equilibrium conditions before SPM probing, both contributions are balanced with no evolution of lithium ion concentration. Since the AC bias is applied with relatively high frequencies in the range of 300 kHz, which is much shorter than typical diffusion time scales, the redistribution of lithium ion concentration is solely due to electro-migration, and such small perturbations do not change the overall lithium ion concentration distribution. Thus, equation (4.1) can be simplified as

$$\frac{\partial n}{\partial t} = \boldsymbol{n_0 D}\frac{zF}{RT}\nabla^2\boldsymbol{\varphi} \quad \textbf{(4.2)}$$

It is thereby evident that changes in lithium ion concentration induced by the SPM tip are proportional to the local equilibrium concentration n_0 as well as to the diffusion coefficient *D*. Since this change is directly proportional to molar volume change and thus the ESM response probed, it can be concluded that ESM amplitude also correlates with the local concentration as well as the diffusion coefficient of Li-ion.

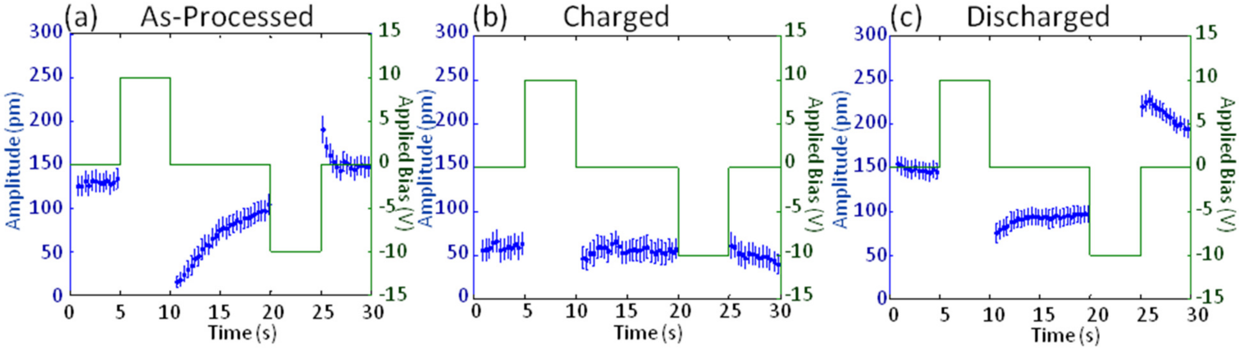

Figure 4.9: Relaxation characteristics of ESM responses of $LiFePO_4$ at different stages of processing and testing, where the left axis indicates the ESM response and the right axis indicates the applied voltage; (a) as processed; (b) charged;, and (c) discharged.

In order to verify this analysis, a sequence of DC step voltages are applied through the SPM tip to the as-processed, charged, and discharged $LiFePO_4$ films and the corresponding ESM responses are measured, as shown in Figure 4.9. Initially, the ESM amplitude is measured in the absence of applied DC voltage to establish a baseline response. A positive DC voltage of 10 V is then applied for 5 seconds, reduced to and maintained at zero for 10 seconds, followed by the application of a negative bias of -10 V for 5 seconds, and then reduced back to zero. The response is dominated by electrostatic interactions when DC voltage is on, which leads to ultrahigh amplitudes. Therefore, only the relaxation of ESM response after the DC voltage is reduced to zero is examined. In the as-processed sample, a large drop in ESM response is observed immediately after the removal of the positive DC voltage, which then gradually increases back to the ground level before application of the negative DC voltage, as shown in Figure 4.9(a). On the other hand, after the removal of a negative DC voltage, a large increase in ESM amplitude is observed, which then gradually decreases to the ground state. The different relaxation characteristics under different DC polarities can be explained from the presented interpretation of ESM responses – a positive DC voltage by SPM tip reduces the lithium ion concentration underneath the SPM tip, resulting in a smaller response than in the ground state, while a negative DC voltage increases the lithium ion concentration underneath the SPM tip, resulting in a larger ESM response. The relaxation of ESM response to its initial state after removal of either positive or negative bias corresponds to the relaxation of lithium ion concentration to the equilibrium distribution. Such interpretation is further confirmed by relaxation characteristics observed for the charged electrode in Figure 4.9(b), where the responses are very close to ground state regardless of applied DC biases, and little relaxation is observed after removal of either positive or negative voltage, due to the lack of lithium ions in the charged cathode. For the discharged cathode, the trend of relaxation is similar to the as-processed sample, though the variation in ESM magnitude is smaller.

The relaxation characteristics after removal of DC voltages confirm that the ESM response correlates with the local concentration and diffusivity of lithium ions, which allows for the examination of differences in lithium ion intercalation and extraction in $LiFePO_4$ materials at different states of charge. Due to the inhomogeneous morphology of the material, differences in ESM amplitude can be seen between the microcrystalline and nanocrystalline structures, as depicted in Figure 4.10.

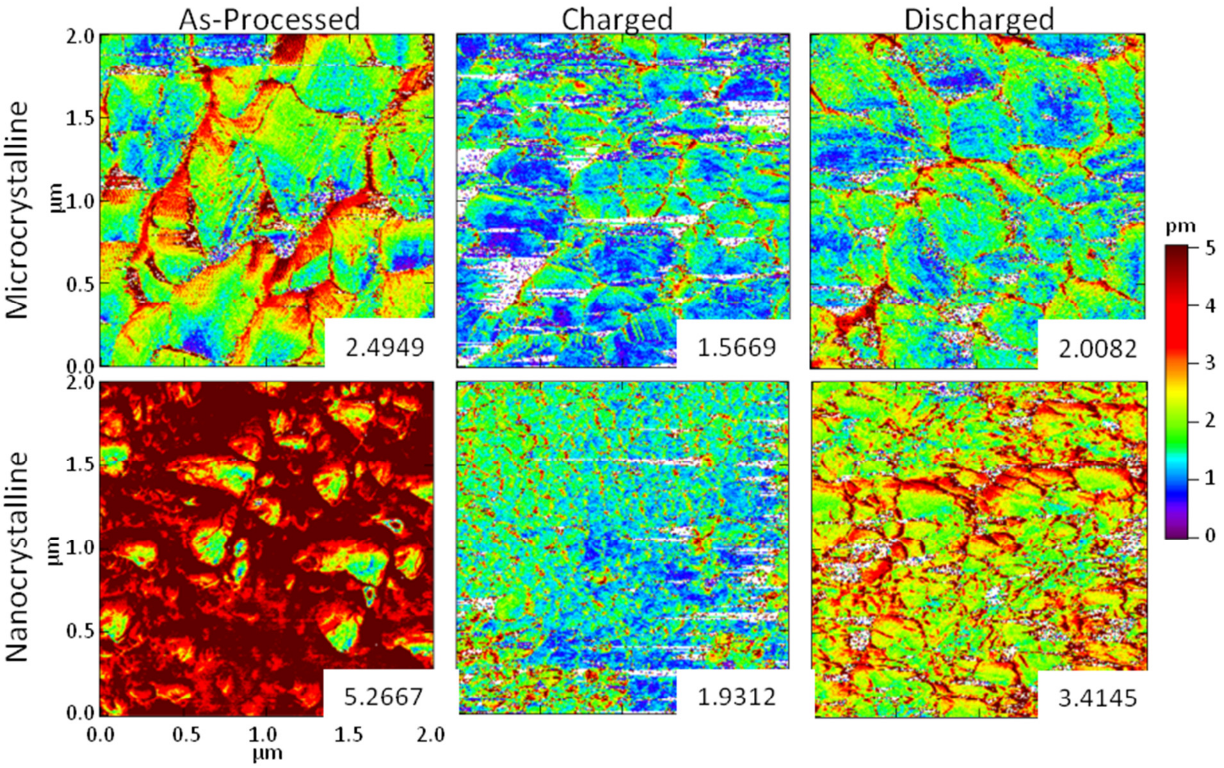

Figure 4.10: Comparison of ESM amplitude mappings of $LiFePO_4$ samples showing microcrystalline and nanocrystalline regions at different stages of processing and testing, with the averaged amplitude identified in each mapping.

The top row maps the microcrystalline area in the as-processed, charged, and discharged states, and the bottom row maps the nanocrystalline areas correspondingly. Again, the differences among as-processed, charged, and discharged samples are evident, confirming that the responses correlate with Li-ion concentration. Even more importantly, more notable differences between micro- and nano- crystalline areas are observed. In the as-processed sample, the averaged ESM response in the nanocrystalline area is more than twice the response of the microcrystalline area, suggesting that lithium ions in the former area have much higher diffusivity. After charging, the averaged amplitude drops substantially in both areas due to extraction of lithium ions, though the nanocrystalline area still shows approximately 20% higher averaged response, again due to its higher diffusivity. In the discharged state, substantially higher ESM response of more than 70% is observed in the nanocrystalline area, which is attributed to both higher Li-ion intercalation and diffusivity. The correlation between nanoscale ESM response and local crystalline morphologies is evident, which may help the understanding of enhanced performance in lithium ion batteries with nanocrystalline $LiFePO_4$ electrodes. Indeed, it has recently been demonstrated that $LiFePO_4$ films annealed at 600°C on Pt-coated Si show nanocrystalline morphology and exhibit a superior initial energy capacity of 312 mAh/g, while $LiFePO_4$ film annealed at 800°C shows microcrystalline morphology, and possesses a relatively low capacity of 120 mAh/g [99]. These local ESM studies thus correlates well with such contrast in macroscopic battery performances and may help understand the mechanisms responsible for performance enhancement in nanocrystalline $LiFePO_4$.

To this end, the mappings of quality factor are also examined, which are inversely proportional to energy dissipation associated with lithium ion redistribution and thus reflects the energy barrier for lithium ion intercalation and extraction. While the total energy dissipation at each point is directly correlated with the quality factor, the energy dissipation per unit lithium ion redistribution is more significant and can be analyzed by normalizing the total dissipation with respect to ESM magnitude, which is directly proportional to redistributed lithium ion concentration. Although the quantity primarily of interest is dissipation originating from ionic motion, it is pointed out that the mechanical dissipation is also included in the data that cannot be separated from ionic effects for the time being. Furthermore, we have ignored the effects of noise background. The mappings of such energy dissipation per unit lithium ion redistribution for micro- and nano-crystalline $LiFePO_4$ under different states are shown in Figure 4.11, and the contrast between the micro- and nano-crystalline $LiFePO_4$ is evident.

The nanocrystalline region shows substantially smaller energy dissipation compared with the microcrystalline one in as-processed and discharged samples, suggesting much smaller energy barriers for lithium ion intercalation and extraction in nanocrystalline $LiFePO_4$. This difference may be due to the one-dimensional ion transport channel in $LiFePO_4$, for which clear crystalline facets as seen in microcrystalline region might not be desirable when they are misaligned with the transport channel. Indeed, it appears from 3D topography that the dissipation is rather uniform within one facet, yet varying from facet to facet in microcrystalline region in the as-processed state. On the other hand, for nanocrystalline region without clear crystalline facet, the dissipation is rather uniform, especially in the as-processed state.

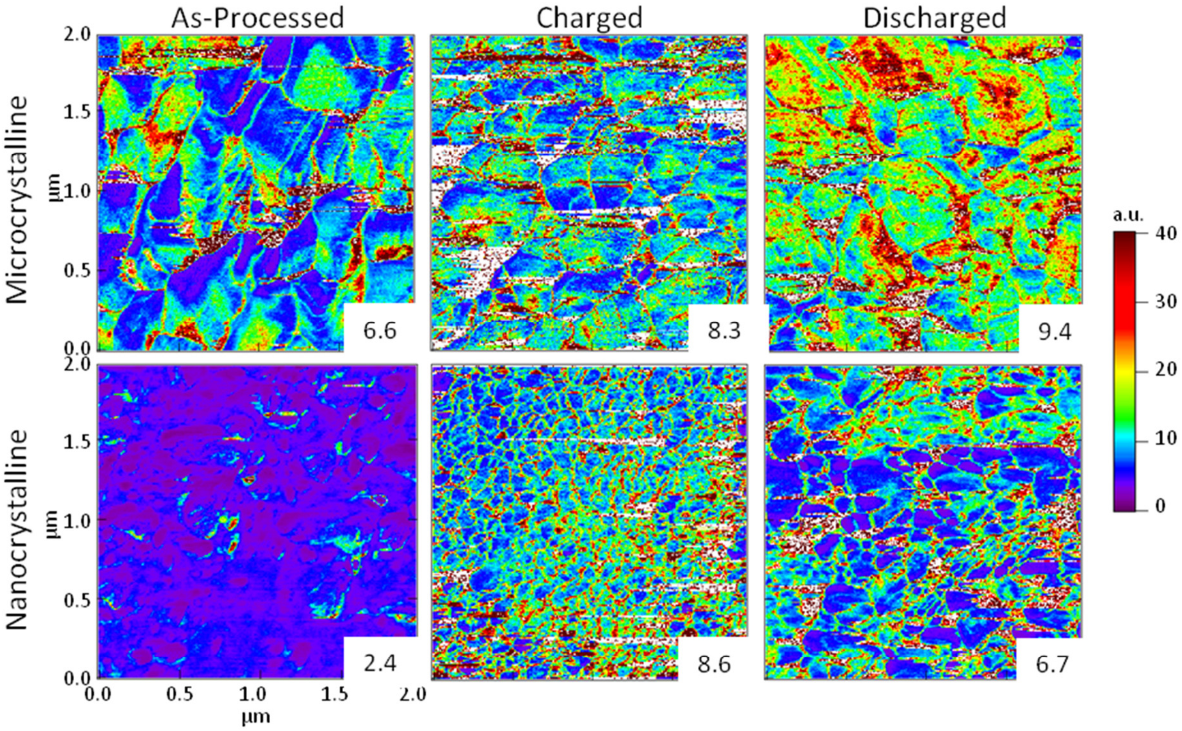

Figure 4.11: Comparison of ESM dissipation mappings, normalized by the calculated amplitude

4.4 Band Excitation Imaging of $LiFePO_4$

Electrochemical strain microscopy experiments on $LiFePO_4$ using the DART method to track resonance frequency resulted in strong correlations among morphology, lithium-ion concentration changes, and electrochemical behavior. However, because the samples of $LiFePO_4$ used were very rough in morphology, questions have arisen regarding the tracking capabilities of the DART method, and how successful it truly was in creating maps of lithium ion concentration changes. The band excitation method, in which the voltage applied to the cantilever consists of a signal encompassing a band of frequencies, was applied to inhomogeneous LiFePO4 samples in as-processed, charged, and discharged states. A schematic of the experiment and an example of the resulting data collected at each point is presented in Figure 4.12.

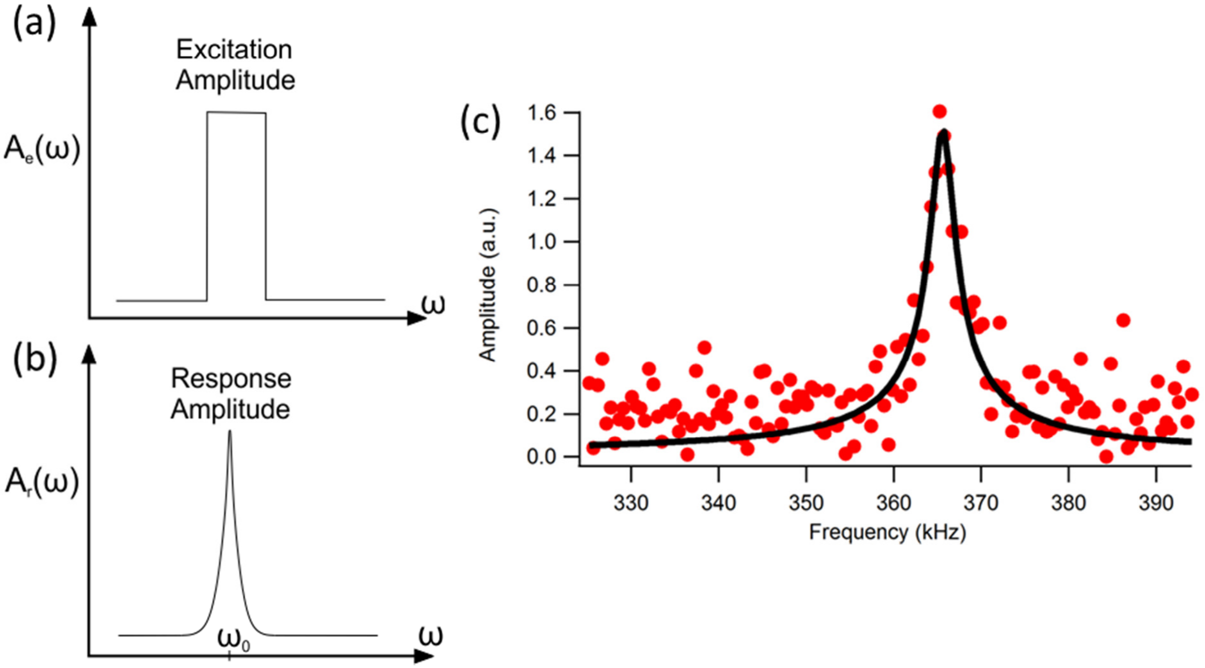

Figure 4.12: (a) Schematic of signal sent to cantilever in frequency domain, (b) schematic of response signal, in frequency domain, (c) actual collected amplitude at a point, fitted using the damped drive harmonic oscillator model.

For band excitation experiments, the amplitude and quality factor information is calculated during post-processing. Therefore, the algorithm by which these values are calculated is important to the overall results. Because of the roughness of the sample, a large frequency bandwidth had to be used to capture all relevant data, typically chosen to be 100 kHz. When the data point had a clear resonance peak, as shown in Figure 4.13(c), the intrinsic amplitude and quality factor could be calculated based on the driven damped harmonic oscillator model described by equations (3.1) and (3.2). However, many data points did not exhibit a resonance peak, an example of which is presented in Figure 4.13(b). When initially analyzing the collected data, this type of data would give a false value for intrinsic amplitude. Therefore, an algorithm was developed to separate out points where there was a peak, as in Figure 4.13(a) from points where the signal was predominantly noise, as in Figure 4.13(b).

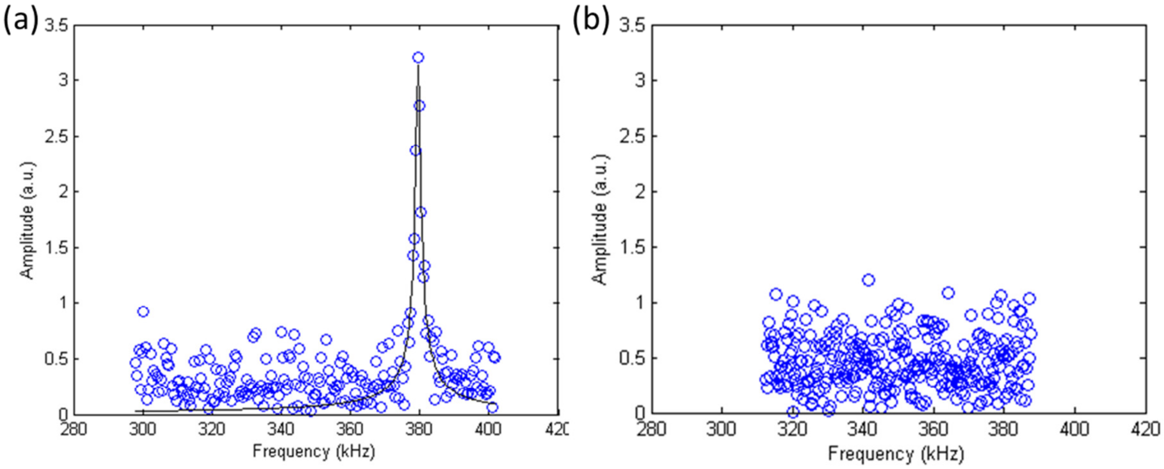

Figure 4.13: Examples of BE data, with (a) signal with fitted SHO, and (b) point where there was no response

The algorithm determined a baseline value for the noise signal, and then calculated if there existed a peak that stood apart from the noise. When there was no such peak, the algorithm would return a “NaN”, or “not a number” value, and would display as white in the color schemes used for amplitude and quality factor. Using this filtering algorithm, ESM maps of the three $LiFePO_4$ samples in the as-processed, charged, and discharged states were compared, as presented in Figure 4.14.

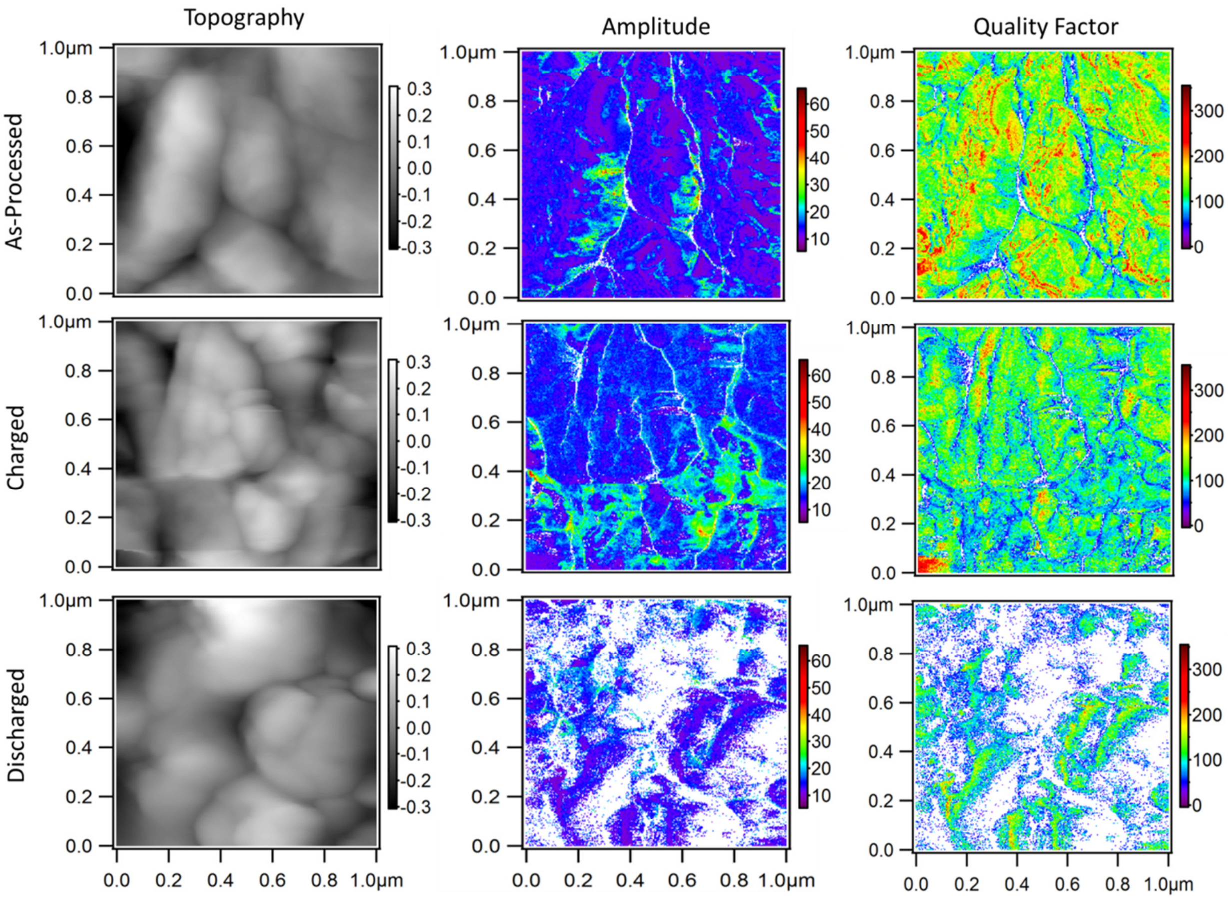

Figure 4.14: Comparison of band excitation results from as-processed, charged, and discharged $LiFePO_4$ samples

In contrast to the DART experiments on lithium iron phosphate at different states of charge, shown in Figure 4.10, the results from BE do not appear to show significant differences in ESM amplitude or quality factor. This is most likely due to the coin-cell testing set-up, in which the lithium ions tended to be unstable at the fully charged or discharged states. Furthermore, this may not be completely representative, as many of the mappings resulted in points where there is little signal, as shown by the many white patches in the discharged amplitude and quality factor images.

The other major experiment performed at Oak Ridge National Laboratory using band excitation was to study the differences between the linear and quadratic responses to applied bias. The first and second harmonic responses were measured in the same location, and the resulting amplitudes and quality factors are presented in Figure 4.15.

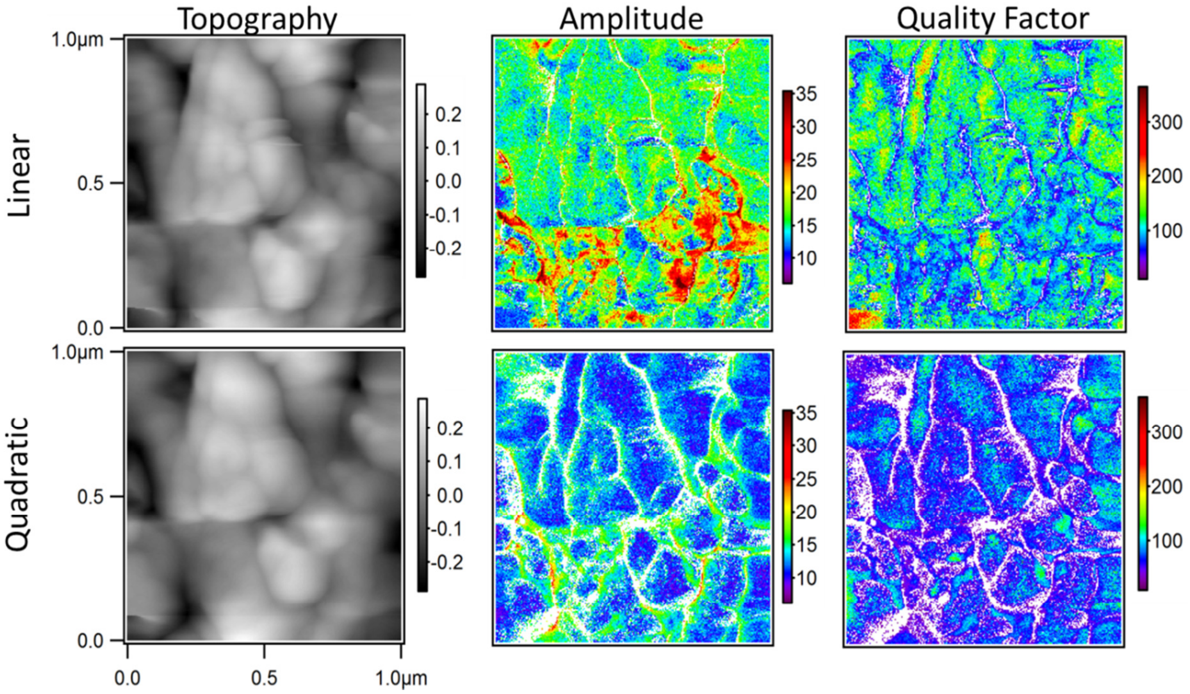

Figure 4.15: Comparison between first and second harmonic responses to applied signal

For lithium-ion battery electrodes, the responses observed in ESM are attributed to Vegard strain, which are predominantly linear with applied bias. There is a strong quadratic response observed here as well, indicating either that there is a 2nd harmonic component to Vegard strain, or that electrostrictive or electrostatic effects may play a role. This is an important area of study that deserves further investigation; especially with other lithium ion battery electrode materials such as the more commonly used lithium cobalt oxide.

Although the band excitation experiments did not indicate clear differentials based on lithium ion state of charge, they help to confirm the observations obtained using DART, particularly at the grain boundaries.

4.5 Summary

Electrochemical strain microscopy (ESM) was used to probe lithium ion concentration changes in inhomogeneous $LiFePO_4$ cathodes with nanometer resolution, using two different resonance tracking techniques. Using the dual amplitude resonance tracking (DART) technique, which relies on error tracking of the amplitude signal, clear correlations were observed between nanoscale lithium ion electrochemical activity, local crystalline morphology, and macroscopic battery level performance. Not only have the local lithium ion concentration and diffusivity been probed, but also the energy dissipation during lithium ion transport been mapped. It was discovered that nanocrystalline $LiFePO_4$ exhibits higher lithium ion diffusivity and lower energy dissipation than microcrystalline $LiFePO_4$, which explains its higher capacity often observed at macroscopic battery level. The DART technique resulted in high signal-to-noise ratios during measurements, but loses some of the detail in amplitude and phase vs frequency curves. The band excitation (BE) technique captures more of the cantilever dynamics in play during ESM, but has lower signal-to-noise ratios. Due to the low signals and high roughness present on $LiFePO_4$ thin films, this resulted in many measured points have no discernable signal separate from the inherent noise in the system. Band excitation was also used to examine the differences between linear and quadratic responses of this material to applied bias, which showed strong quadratic signals, but that were lower than the linear signal. The underlying cause of the quadratic response is still undetermined, and may be due to second harmonic components of the Vegard strain, or due to electrostrictive or electrostatic effects. This study thus can help understand lithium ion intercalation and extraction at nanoscale, particular their dependence on crystalline morphologies and defects, and can help develop electrode materials for lithium ion batteries with enhanced performance.

5 Electrochemical strain microscopy of doped ceria as an electrolyte for solid oxide fuel cells

5.1 Motivation

Solid oxide fuel cells are receiving increasing amounts of attention from the research community and energy developers at large, as power generators in stationary, portable, and transportation applications. Not only do they convert chemical fuel to electrical energy with high efficiency, but also produce much lower emissions of carbon dioxide and hydrocarbons compared to petrochemical sources. Solid oxide fuel cells are defined by their electrolyte, consisting of a metal oxide oxygen ion conductor, and typically operate at high temperatures, between 800 – 1000°C [62]. However, as progress in efficiency and longevity increases, the high operating temperatures are proving to be a major limitation [130], as it requires special materials for housing and interconnects. A new field arose with the goal of reducing the operating temperature to 500 - 700°C, termed intermediate-temperature solid oxide fuel cells. To realize this technology, alterations would have to be made in all components. Here, the focus is on the electrolyte, which must continue to be ionically conductive at lower temperatures. Doped ceria has been found to have high ionic conductivities at lower temperatures, as compared to the commonly used yttria-stabilized zirconia (YSZ), and also exhibits lower polarization resistances [131-133]. However, doped ceria can also have the disadvantage of being electronically conductive under reducing conditions [134, 135], and nanostructured ceria can be electronically conductive even under oxidizing conditions [136]. The degree to which ceria behaves as a mixed conductor is dependent on its doping level, temperature, and oxygen activity [131]. The exact basis of this mixed conduction is still not completely understood, with initial explanations attributing increased electronic conductivities being due to finite size effects or dopant segregation in the bulk of the material [137]. However, recent research have shown that a strong case can be made for conductivity increases arising from space-charge effects near grain boundaries, as schematically depicted in Figure 5.1.

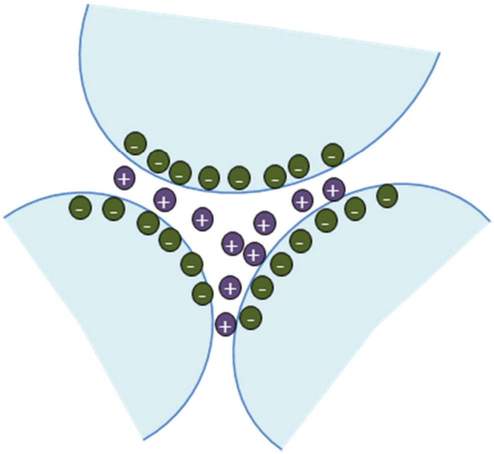

Figure 5.1: Schematic of space charge model, with the blue areas indicating grains, and the circles indicating charges

In this model, positively charged species, impurities, and/or defects move to the grain boundaries in order to decrease the overall energy in the system [138]. To maintain neutrality, the opposite charge to that of the interfacial core will accumulate in the adjoining grains, forming a space-charge region. The compensating charge is composed of small polarons, that is, electrons and their associated lattice distortions. The size of the space charge region is directly related to the Debye screening length [138],

$$L_D = \left(\frac{\epsilon_r \epsilon_0 k}{T q^2 C_b}\right)^{1/2} \tag{5.1}$$

where C_b is the concentration of the bulk majority carrier. Depending on material properties, the Debye length can be on the order of 50 - 100 nm. As grain sizes in doped ceria approach the Debye length, the space charge effect dominates, leading to electronic conduction in nanostructured doped ceria at even low temperatures. It is important to emphasize that this is at this point only a model. The purpose of this project is to examine the space-charge model using electrochemical strain microscopy (ESM), a novel technique that has never been applied to this particular system. Although the system to be studied is not nanocrystalline in nature, ESM is applied locally at the grain boundaries and at the surface, focusing on areas where the space-charge region holds sway.

5.2 ESM Experimental Setup

A sample of samarium doped ceria ($Ce_{0.8}Sm_{0.2}O_{2-\delta}$) was obtained from Professor Adler's laboratory, which was processed as described in Lu's thesis [139]. The SDC electrolyte was sintered at 1625-1650°C to form flat electrolyte plates. Scanning electron microscope images of the resulting surface morphology is shown in Figure 5.2(a), and shows evidence of clear grain boundaries.

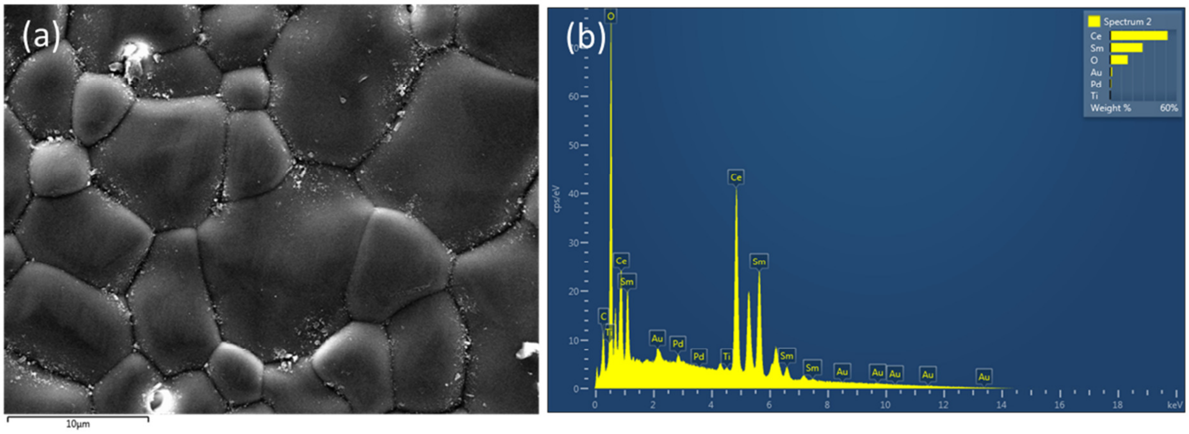

Figure 5.2: (a) SEM image of samarium-doped ceria (b) EDS analysis of composition

The SEM image in Figure 5.2(a) was taken after first sputtering gold particles onto the surface of the electrolyte in order to form a conductive path for imaging purposes. Energy dispersive spectroscopy (EDS) was performed on this sample as well, with the results shown in Figure 5.2(b), indicating that the approximate concentration of samarium in the specimen was 20%.

The sample was mounted onto a piece of gold-coated silicon wafer using conductive silver paint. The gold-coated wafer was then placed onto the PolyHeater^{TM} unit from Asylum Research, which has the capability to heat up to 300°C. A photograph of the sample and the PolyHeater unit are shown in Figure 5.3.

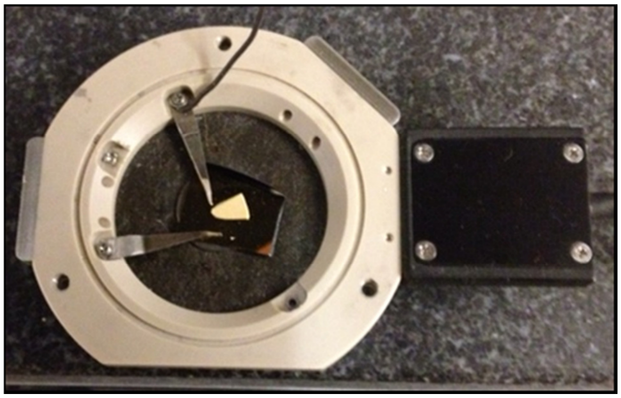

Figure 5.3: Photograph of heater with sample and substrate mounted

Metal clips are used to hold the wafer and sample in place; the metal clip also serves to connect the gold-coated wafer to an external ground, completing the electrical circuit once the SPM tip is applied to the sample. For all of the varying temperature experiments, the PolyHeater is heated to the desired temperature at a rate of 5°C/min. Increasing temperature also causes the SPM cantilever, which is composed of silicon coated with titanium and iridium, to expand. Due to this expansion, at least 30 minutes was allowed to elapse before beginning any experiments to ensure that the entire system was at the steady state temperature.

5.3 Proposed Mechanism for ESM of SDC

Previous research into electrochemical strain microscopy on samarium doped ceria by Kumar and colleagues attributed observed strain responses to chemical strains caused by local changes in oxygen vacancy concentration upon reduction/oxidation of the bulk material near the scanning probe microscope tip [107, 140]. However, this explanation appears unlikely due to chemical expansion due to oxygen vacancies being too small in magnitude at the low temperatures studied. It is more likely that the strains induced by AC biases arise from changes in small polaron concentration in the space charge region near the surface of the material and at grain boundaries. The determination on whether the material behaves expansively or contractively with positive bias can serve to distinguish the mechanism by which the observed strains are generated. This is done by measuring the intrinsic phase of the material, as described in more detail in Chapter 3. Because the intrinsic phase of the material is difficult to separate out from cantilever dynamics and system phase lags, ferroelectric thin films were used as calibration materials, with which SDC could be compared to. Figure 5.4(a) depicts the locations at which the phase measurements were made, and Figure 5.4(b) shows the results from the phase measurements as compared to ferroelectric materials.

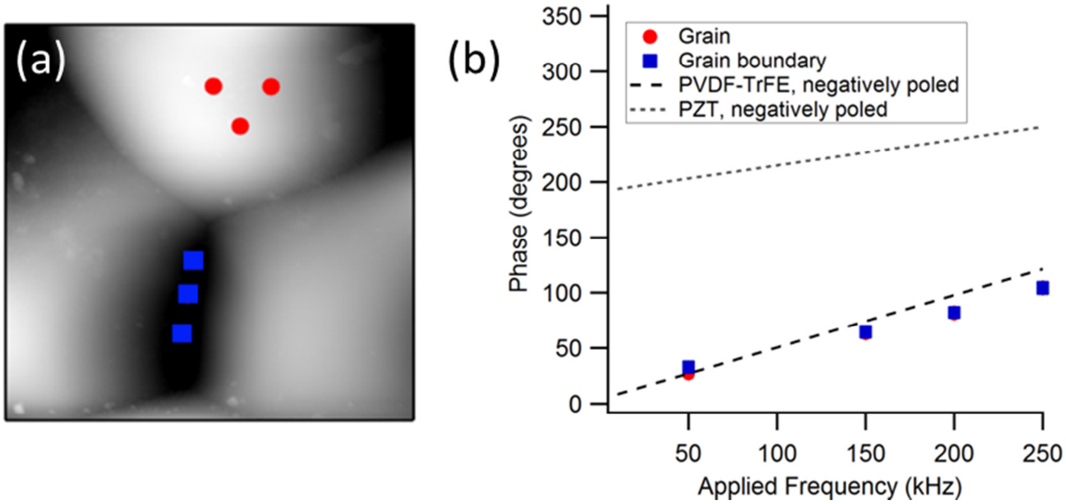

Figure 5.4: (a) AFM topography image showing where on the SDC sample the phase measurements were made, (b) phase measurements as a function of frequency compared against negatively poled regions of PVDF-TrFE and PZT

The intrinsic phase of SDC was measured at locations on the bulk grain and at grain boundaries in order to determine if the governing mechanism is different in these regions. The measured phases are compared to negatively poled regions of PZT and PVDF-TrFE, and found to be similar to negatively poled PVDF-TrFE, which is known to behave expansively with applied positive bias. The results are consistent between locations on the grain and at the grain boundary, indicating that the same governing mechanism exists in both regions. The intrinsic phase lag was also measured as a function of temperature, as displayed in Figure 5.5, with all measurements taken at a 50 kHz frequency.

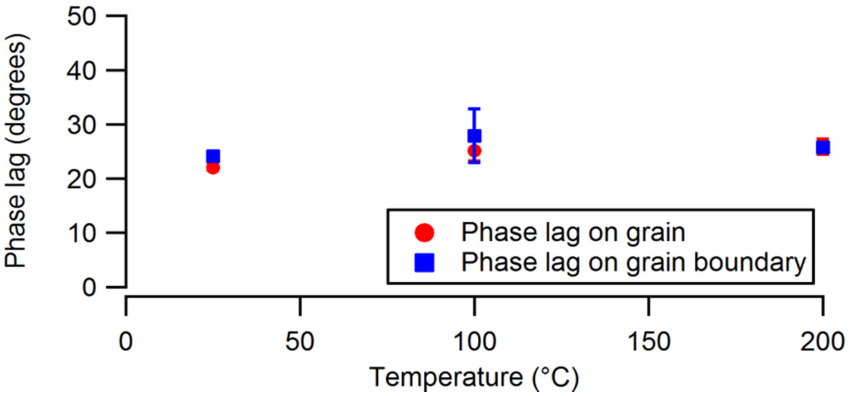

Figure 5.5: Phase measurement as a function of temperature on samarium doped ceria at locations on the grain and at the grain boundary

These results show that the intrinsic phase is not affected by temperature, implying that the governing mechanism is consistent on the bulk grain and at grain boundaries up to 200°C.

Based on these results, it was hypothesized that the measured responses were due to concentration changes of small polarons in the space charge region. In particular, the strain responses are due to the lattice distortions attributed to the valence change of cerium ions. This effect has been studied as a part of chemical expansion, as described by equation (5.2), in Kröger-Vink notation.

$$2Ce_{Ce}^{x} + O_{O}^{x} \leftrightarrow V_{O}^{\cdot\cdot} + \tfrac{1}{2}O_2 + 2Ce_{Ce}' \qquad (5.2)$$

From the work of Marrocchelli and colleagues, it was determined that the expansivity arises from the valence change of cerium atoms rather than the formation of oxygen vacancies, which actually have a contractive effect [141]. This model of chemical expansion assumes electroneutrality, which is true in the bulk of doped ceria. However, in space charge regions, there is not necessarily such an assumption. Furthermore, it is unlikely that oxygen vacancies are sufficiently mobile at the low temperatures and high frequencies present in ESM experiments. As a result, the measured ESM responses are attributed to the valence change of ceria that accompanies the motion of electrons at the surface and at grain boundaries, as described by equation (5.3).

$$Ce^{4+} + e^{-} \leftrightarrow Ce^{3+} \qquad (5.3)$$

The experimentally measured strain results induced by AC biases can be interpreted using this model, as concentration changes of small polarons. This can be schematically illustrated as in Figure 5.6.

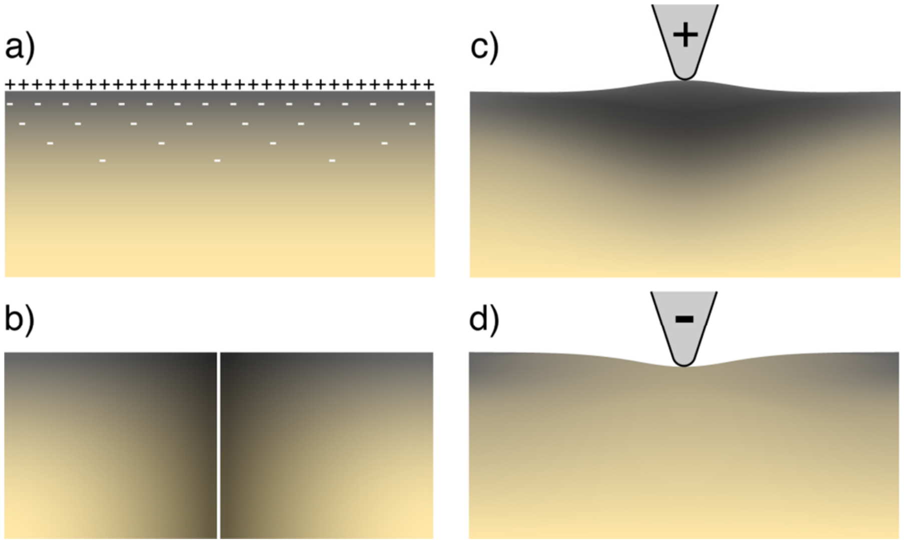

Figure 5.6: Schematic of proposed mechanism for ESM on doped ceria, showing (a) an accumulation of positive charge at the surface, compensated by small polarons within a diffuse space charge region in the bulk, (b) further accentuation of this effect at grain boundaries due to positive charge accumulation in the grain boundary core. Under (c) positive locally applied bias, the small polaron concentration increases, causing expansion at the surface, while under (d) negative locally applied bias, the small polaron concentration decreases, causing local contraction [142].

The interpretation of ESM responses in the rest of this section is based on the model presented.

5.4 ESM Mapping of SDC at increasing temperatures

One goal for this study was to examine the surface strain amplitudes of SDC as a function of temperature. In order to quantitatively determine the amplitude, a set of mapping experiments were performed at increasing temperatures. To maintain consistency, an effort was made to perform the electrochemical strain microscopy (ESM) experiments over the same topographical area. Due to expansion of the cantilever, the location of the cantilever probe on the sample changes each time the temperature is altered. In order to perform ESM over the same area at different temperatures, a 50 µm x 50 µm area was first scanned using tapping mode atomic force microscopy, which, due to intermittent contact between tip and sample, results in less wear on the probe, and allows for scans over larger areas without significantly dulling the probe. Once a specific feature is isolated, ESM is then performed on the smaller area. An example of ESM mapping of a 5 µm by 5 µm area is depicted in Figure 5.7, using an applied bias of 3 V.

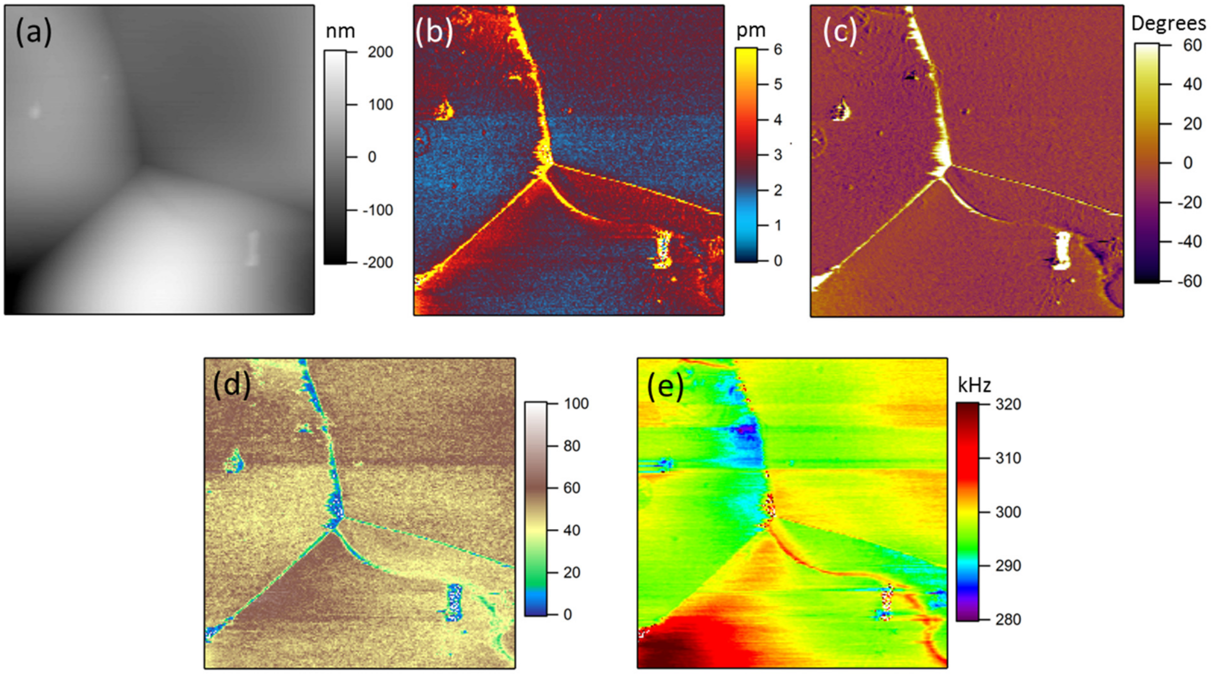

Figure 5.7: ESM mapping of (a) topography, (b) amplitude, (c) phase, (d) quality factor, and (e) resonant frequency at room temperature. The amplitude, phase, quality factor, and resonant frequency were calculated from a damped drive harmonic oscillator model from mappings obtained using DART.

Here, as in previous experiments with $LiFePO_4$, all of the ESM scans are performed in dual amplitude resonance tracking (DART) mode, with the final properties calculated using the damped driven harmonic resonator model. As Figure 5.7 depicts, the values for amplitude, quality factor, and phase are fairly constant over the grains, but deviate significantly along the grain boundaries. The increased amplitude at grain boundaries is due to the higher concentration of small polarons accumulating at the space charge region. This effect becomes more pronounced at increased temperatures, as seen in Figure 5.8.

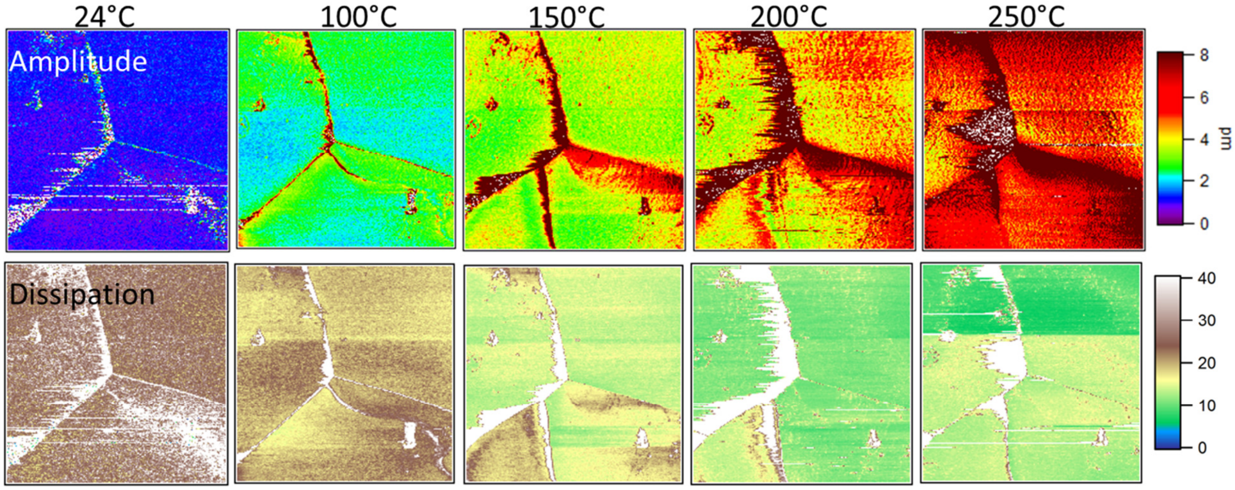

Figure 5.8: ESM amplitude and quality factors of SDC at varying temperatures.

The amplitude increases with increasing temperature, as small polarons become increasingly mobile at higher temperatures. At each temperature, the response is higher at the grain boundaries, as the concentration of small polarons is higher. The dissipation, a measure of energy losses in the system, decreases with increasing temperature, indicating that the barrier to motion decreases. For each temperature, the amplitude and dissipation values were averaged over the area scanned, and the results are collected in Figure 5.9.

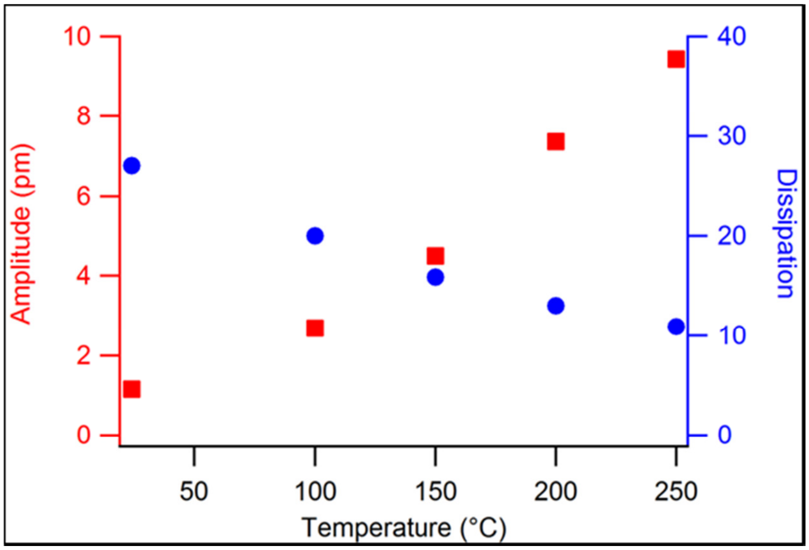

Figure 5.9: Averaged amplitudes and quality factors at each temperature

The increase in amplitude and quality factor with temperature is close to linear, indicating a direct correlation between the temperature of the specimen and the strain changes induced by applied bias. From the averaged amplitude data, the activation energy can be estimated, by fitting the natural log of the amplitude versus the temperature, as shown in Figure 5.10.

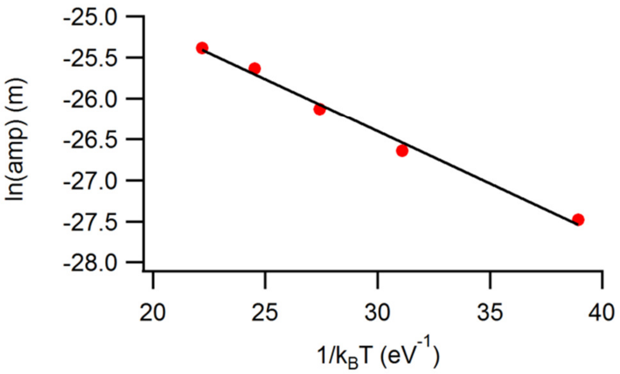

Figure 5.10: Arrhenius plot of average strain amplitude vs. temperature, with a slope of ~0.20 eV

The estimated activation energy is approximately 0.20 eV, which is smaller than the activation energy of small polaron mobility, 0.4 eV [143]. This result further supports the hypothesis of small polaron mobility being the driving mechanism of observed ESM strain changes.

5.5 Relaxation studies of SDC at increasing temperatures

The results described thus far took place at very small time scales, with biases and strains measured close to 300 kHz. At longer timescales, however, polarization on the surface may have an effect on less mobile defects. The first set of experiments focused on applying a series of direct current (DC) biases and examining the amplitude response after the DC voltage was removed. During the experiment, a 3 V AC bias was continually applied on top of the DC bias in order to measure the amplitude response, as schematically described in Figure 5.11.

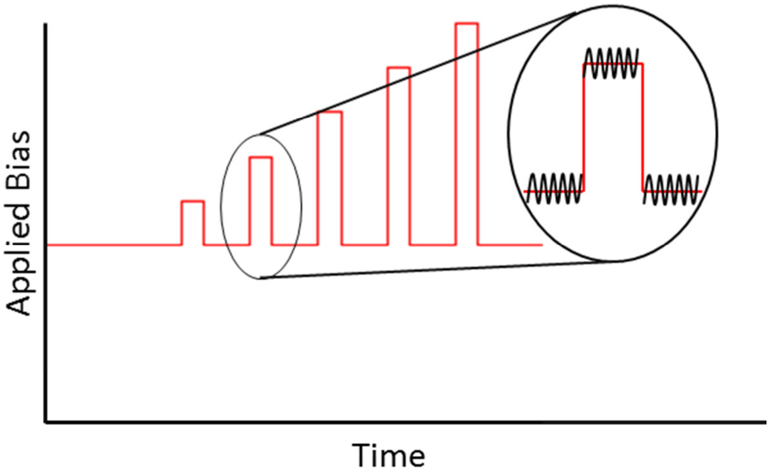

Figure 5.11: Schematic of experiment with AC biases overlaid onto DC pulses.

While the DC pulses are applied to the sample, the amplitude response is dominated by electrostatic effects, which lead to artificially high amplitudes. As a result, only the amplitude response in the DC off state is examined, which serves to study the relaxation behavior of the SDC sample to applied biases. Both positive and negative biases are applied to the sample. Figure 5.12 depicts relaxation studies at room temperature, 100°C, and 200°C, showing the results of applying a series of increasing positive pulses and a series of increasingly negative pulses.

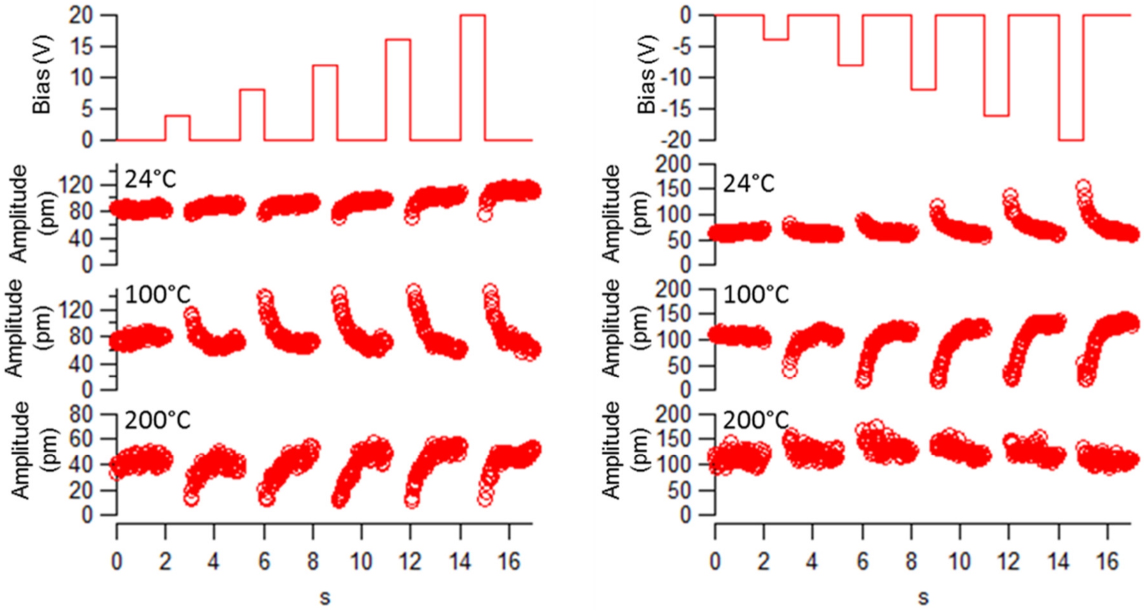

Figure 5.12: Relaxation behavior at varying temperatures, as a function of applied DC bias

Here, the primary conclusion is that increasing the applied DC bias does not appear to significantly alter the shape of the relaxation curve. Therefore, for further studies, it was determined that a pulse of ±10 V is sufficient to study relaxation behavior. From these results, it is also apparent that the shape of the relaxation curve changes with temperature. However, this change with temperature is not a consistently observed behavior. The behavior can depend on the location upon which the measurement was taken, as described in Figure 5.13, showing differing relaxation behavior upon the application of a positive DC bias based on whether the experiment was performed on the bulk grain or at a grain boundary.

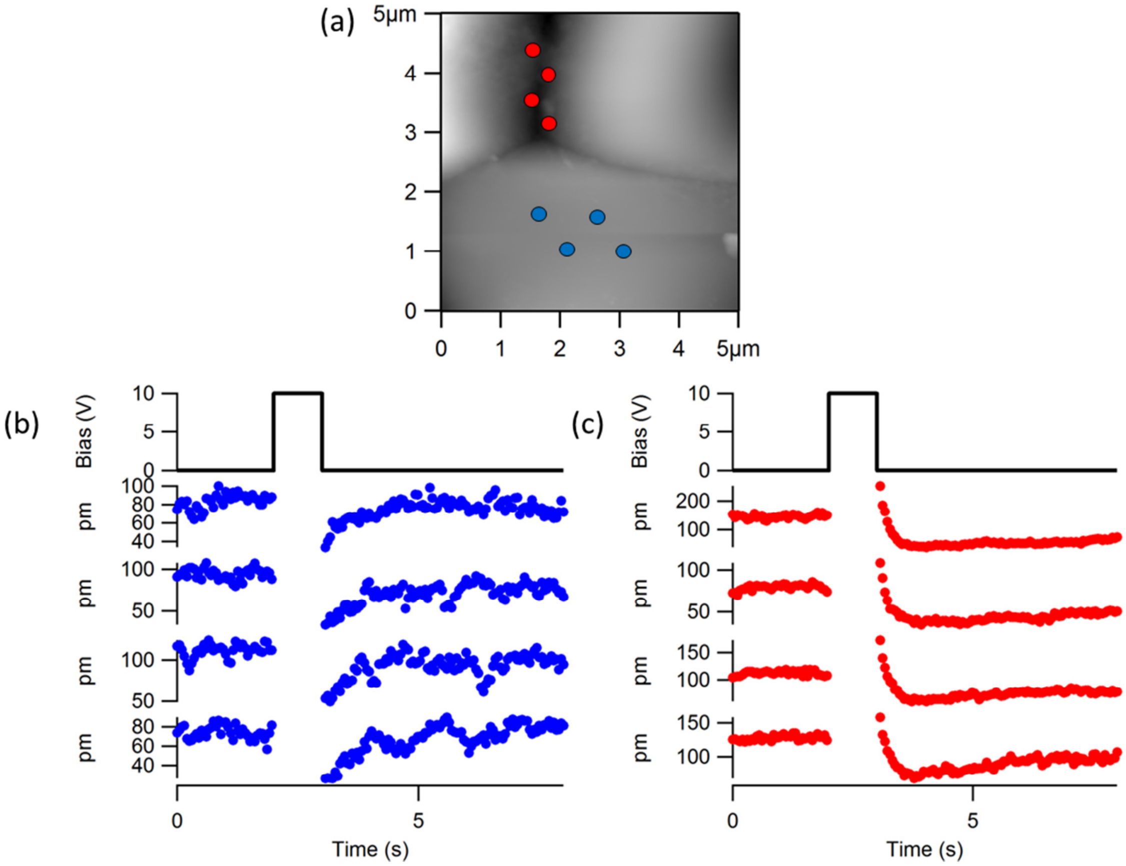

Figure 5.13: Relaxation behavior of SDC at 100°C with (a) AFM topography image showing locations on surface at which measurements were taken, (b) relaxation after positive DC bias on bulk grain, and (c) relaxation after positive DC bias on grain boundary.

These results indicate that there could be a different mechanism at play on the bulk grain versus the grain boundary. Furthermore, at the grain boundary, it appears that there could be multiple relaxation phenomenon observed, one indicating an increase of ESM signal immediately after removal of the DC bias, which gives way to another indicating suppression of ESM signal. The relaxation behavior can also be dependent on the environmental conditions of the laboratory. In Figure 5.14, the relaxation response to a positive DC bias is plotted for a “typical” day in the lab, as shown in Figure 5.14(a), is compared to the relaxation response for an exceptionally hot and humid day in the lab, as shown in Figure 5.14(b).

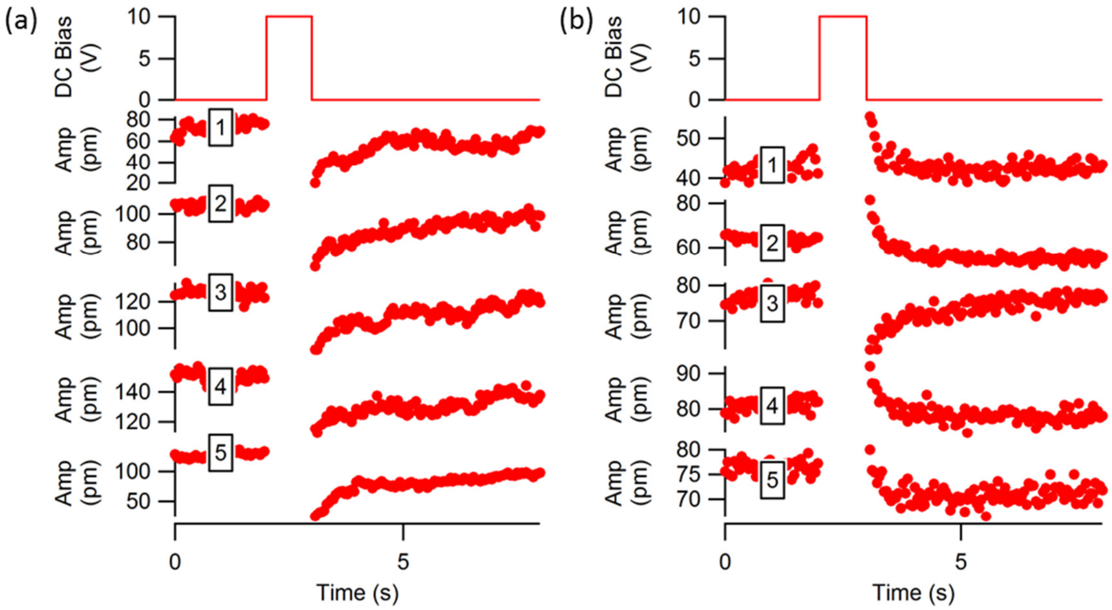

Figure 5.14: (a) Relaxation response on a "typical" day in the lab, and (b) relaxation response on an exceptionally hot and humid day, both sets measured without added heating.

Both sets of data in Figure 5.14 were collected without the use of the heating element, and can be considered as measured at "room temperature", even though the exact room temperature conditions are different. On a typical day, the room was at approximately 24°C - 25°C, while on the "exceptionally hot and humid" day, the room was at approximately 27°C - 28°C. The humidity of the room was not measured, and can only be described qualitatively. The relaxation behavior on a typical day showed a suppression of ESM signal after the application of a positive DC bias, while on a hot day, there appeared to be some reversal of this signal even without heating.

Even when using the heating element for relaxation experiments, the results were inconsistent, and could be dependent on the amount of time between the onset of heating and the measurement. Figure 5.15 shows the difference in relaxation behavior at 65°C for a sample 30 minutes after the onset of heating and 5 hours after the onset of heating.

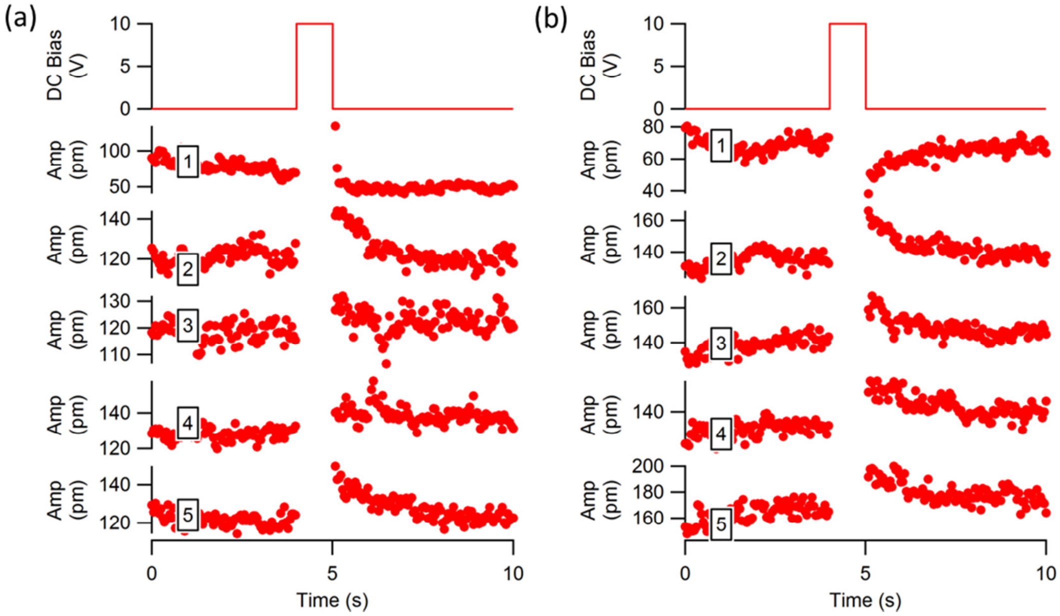

Figure 5.15: Relaxation behavior after the application of a 10 V DC bias at 65°C (a) 30 minutes after onset of heating and (b) 5 hours after onset of heating

Although the results are similar, it appears that the increase in ESM signal is more pronounced after a longer heating time, and in at least one case, showed opposite behavior.

Because of all of these discrepancies, it is difficult to determine the exact mechanism that governs ESM behavior after application of DC biases. One possible explanation is that sustained positive bias slowly drives oxygen vacancies out of the diffuse space charge region, leading to a decrease in the concentration of small polarons, and thus decreases the ESM signal intensity for some time period until the system relaxes back to equilibrium. This explains only the behavior at room temperature. Another, more likely, possibility is that sustained DC bias causes shifts in the concentration of charged defects or adsorbates on the surface. This explanation is more probable because the relaxation behavior changes depending on location, environmental conditions, and time after onset of heating, all of which can alter the surface properties of the sample. In order to fully characterize the relaxation behavior in this material, some of these variables would have to be controlled for by fully controlling the environmental conditions of the experiment.

5.6 Summary

Electrochemical strain microscopy (ESM) has shown to be a valuable tool in examining ion and electron defect dynamics at nanoscale. In this chapter, ESM was applied to samarium doped ceria, in which the strain induced by AC biases was determined to be caused by changes in the small polaron concentration, that is electrons and associated lattice shifts. This theory stands in direct opposition to previous research asserting that oxygen vacancy motion was the cause. Through phase analysis, it was determined that doped ceria undergoes expansion with positive bias, which correlates with small polaron rather than oxygen vacancy mobility. Mappings of the surface of samarium doped ceria (SDC) found that the amplitude of strain response was higher at grain boundaries, where the concentration of small polarons is also higher, and that the amplitude increases with increased temperature, as the mobility increases with temperature. The application of large DC biases to the surface caused shifts in the concentration of small polarons, which over time, relaxed back to its initial state. The direction and degree to which the small polaron concentration was altered depended on the location of the experiment on bulk grain or at grain boundaries, environmental conditions, and how long the sample was heated for at higher temperatures. Because of the inconsistencies of the results, it is most likely that the relaxation responses are due to shifting of surface adsorbates and defects. This area warrants further study, controlling for the different variables separately in order to isolate the relevant mechanism at each condition. ESM may provide a way to investigate local displacement in defect concentrations, revealing more clearly why and how electrode reactions proceed at nanometer length scales.

6 Deposition and Characterization of Cathode Catalysts for Metal-Air Batteries

This section describes research performed at the Jet Propulsion Laboratory over the course of summers 2012, 2013, and 2014, under the supervision of Dr. Andrew Kindler in the electrochemistry group, Section 3463.

6.1 Motivation

Metal-air batteries can be thought of as hybrids between batteries and fuel cells, consisting of metallic negative electrodes and air catalysts as positive electrodes [144]. Metal-air batteries were first developed early in the previous century, and were investigated with great interest in the 1960s and 1970s as energy storage solutions for a wide variety of applications [145]. However, problems with material corrosion and other technical issues led to a drop-off in interest, and the development of lithium-ion and nickel metal-hydride batteries quickly replaced metal-air technology for most applications. However, modern demands of grid storage and electric vehicles are demanding performance beyond the current battery technology. As such, metal-air batteries have received increasing attention in the past decade due to their high theoretical energy densities [146, 147]. Metal-air batteries use oxygen from the air as one of the reactants in the cell, eliminating the weight of the positive electrode that a conventional battery would contain, similar in operation to a fuel cell cathode. The anode can be considered a consumable fuel, as in aluminum-air batteries, or a rechargeable electrode comparable to those in secondary batteries, as in iron-air batteries. Both electrodes, along with the selection of a compatible electrolyte and design of the overall cell, are the subject of increased attention by the research community, as improvements in each element are necessary for the more wide-spread adoption of metal-air technology.

This chapter covers the work undertaken over the course of three internships at the Jet Propulsion Laboratory, in which the area of emphasis was on electrically rechargeable metal-air batteries, particularly iron-air batteries for grid storage and metal-hydride air batteries for electric vehicles. Both systems operate in alkaline solutions, and share common requirements for the air cathode. Iron-air batteries have been under consideration for grid storage, since the requirements in that application focus more on price and long cycle lives rather than on density and power [2-4]. Thus far, sodium-sulfur and redox flow batteries have been the most commonly deployed for grid storage, but recent analysis suggest that aggressive cost reductions would have to be made for long-term implementation [148]. Iron-air batteries can serve as a viable alternative, due to their low cost, abundant material supply, and environmental-friendliness [149].

For electric vehicle applications, alkaline rechargeable batteries have an important advantage over the currently dominant lithium-ion technology, because these aqueous systems are less flammable and therefore do not require stringent thermal regulation systems, which add weight to overall battery packs. Metal-hydride air batteries arise out of nickel-metal hydride systems, which are still in use in some electric vehicles. Metal-hydride air batteries seek to replace the nickel electrode, which weighs approximately the same amount as the metal-hydride electrode but has only two-thirds of its capacity [150]. Previous development of metal-air batteries have involved the use of different electrodes for charging and discharging, which reduces the overall capacity of the system [151]. The development of a bifunctional catalytic material can make this technology more feasible for practical use, since its overall capacity would be higher than its competitors.

Both metal-hydride air and iron-air batteries require truly bifunctional air catalysts to be considered electrically rechargeable. The reactions at the air cathode, when isolated, can be considered identical for both systems. During discharge of the battery, oxygen is reduced to hydroxide ions, while during charging, hydroxide ions are oxidized to evolve oxygen.

Charge: $$4OH^- \rightarrow O_2 + 2H_2O + 4e^- \qquad (6.1)$$

Discharge: $$O_2 + 2H_2O + 4e^- \rightarrow 4OH^- \qquad (6.2)$$

The search for an air catalyst that can accomplish both oxygen reduction and oxygen evolution reactions for many cycles without degradation is crucial to the wide-spread feasibility of metal-air batteries. A number of different catalysts have been considered, predominantly noble metal catalysts such platinum and platinum alloys, and transition metal alloys such as perovskites and spinels [152, 153]. Oxygen reduction can occur via direct electron reduction, as described in equation (6.2), or can go through a pathway involving peroxide [154], when then reduces into hydroxide ions. The direct electron reduction process most commonly occurs on noble metal catalysts, while the peroxide pathway often occurs in transition metal oxides.. These transition metal oxides, which are considered low-cost alternatives, are typically mixed with high surface-area carbon to enhance conductivity [155, 156], and require carbon to support the catalytic reduction to hydroperoxide [157]. Carbon, however, is unstable at high potentials, and is subject to oxidation and subsequent degradation during the oxygen evolution reaction [158]. Therefore, to use transition metal oxides as bifunctional catalysts, carbon has to be eliminated from the electrode. One of the goals of this work was to characterize carbon-less nickel cobalt oxide spinels as a low-cost bifunctional catalyst. The other goal was to examine if thin coatings of noble metals could be used as bifunctional catalyst, gaining the advantage of these materials, while reducing the overall cost.

6.2 Catalyst Fabrication

The majority of the catalysts tested were prepared by sputtering. Sputtering is a thin film deposition technique that uses energetic ions, in this case argon ions, to bombard atoms or molecules from a target containing the source material and deposit them on a substrate [159]. Reactive gases can also be introduced during the sputtering chamber to form compound films, such as the spinel nickel cobalt oxide. The only sample that wasn't sputtered was a polycrystalline platinum electrode (99.99% pure, Pine Instruments) that was used as a control sample, against which other catalytic materials were measured, and also as a test electrode to determine the potential of the reference electrode used.

The noble metal catalysts studied in this project were predominantly platinum based. Thin film platinum samples were fabricated through sputtering directly onto glassy carbon electrodes. These samples were sputtered in a basic sputtering chamber, after pumping down the chamber to approximately 70 mTorr, for different amounts of time, forming films of approximately 100 nm, 50 nm, and 25 nm thick, respectively. The platinum ruthenium thin films were sputtered onto glassy carbon electrodes in a high vacuum chamber that was pumped down to less than 3×10^{-7} Torr. For this second sputtering process, the PtRu targets were first conditioned by sputtering for 1 minute with a power setting of 50 W, then sputtered onto the electrodes for 5 minutes, 2.5 minutes, and 1.25 minutes, respectively, all at a power setting of 50 W.

The spinel nickel cobalt oxide was deposited via reactive sputtering, that is, by flowing oxygen gas into the sputtering chamber in order to form oxide material from a $NiCo_2$ target. The ratios of oxygen and argon gas flowing into the sputtering chamber had an effect on the composition of the resulting material. Three samples of nickel cobalt oxides were formed, with 10%, 20%, and 30% oxygen in the overall gaseous mixture, respectively, with the total gas flow kept constant. During the sputtering process, the target was conditioned for 10 minutes with argon flow only, followed by oxygen being introduced into the system. All of the samples were sputtered for 10 minutes.

6.3 Rotating Disc Electrode Experiments for Catalytic Performance Evaluation

The catalytic materials described were tested for oxygen reduction reaction (ORR) and oxygen evolution reaction (OER) performance using a rotating disc electrode set-up. During the electrochemical operation of a metal-air battery, it is very difficult to separate out the catalytic activity of the electrodes from mass transport effects in the electrolyte, and other flooding or drying effects related to cell design [154]. The rotating disc electrode method is ideal for evaluating catalytic performance, since the convective behavior of the electrolyte is well-characterized in the steady state [160]. The purposes of these experiments were to evaluate materials for use as electrocatalysts. As such, the emphasis in oxygen reduction reaction evaluation was to compare the limiting currents of different materials. This limiting current is reached when the applied potential is sufficiently negative such that oxygen molecules that reach the electrode are immediately converted to hydroxide ions. Materials with higher magnitudes of limiting currents are more electrocatalytic in the oxygen reduction mode. Since the limiting current is also related to the rotation rate of the electrode, materials must be compared against each other at the same rotation rate. On the oxygen evolution side, the concern is the voltage versus reference at which the current begins to rise exponentially. The lower the voltage at which this occurs, the better the catalyst is at evolving oxygen.

The procedure for the rotating disc electrode experiments were derived from a protocol obtained from Professor S. R. Narayanan's group at the University of Southern California. The oxygen reduction experiments took place in an oxygen saturated environment. Oxygen gas was bubbled into the test solution for at least 30 minutes, and then blanketed over the solution during testing. An open circuit potential measurement and 25 cycles of cyclic voltammetry at a high sweep rate were performed in order to obtain a baseline measurement and stabilize the set-up. The actual ORR data presented were taken immediately after, as cyclic voltammograms at a rate of 2 mV/s for two cycles at each of the following rotation speeds: 2500 RPM, 1600 RPM, 900 RPM, and 400 RPM. The oxygen evolution reaction experiments took place in an argon-saturated solution. Argon gas was bubbled into the solution for at least 1 hour, and then blanketed over the solution during testing. Again, the open circuit potential was measured to obtain a baseline, followed by the performance of a slow sweep from 0 V to 0.65 V vs. Hg/HgO to obtain OER data. The results from ORR and OER measurements were compared against each other in an effort to find optimal catalytic materials for a bifunctional air electrode.

6.4 Catalytic Testing Results

6.4.1 Evaluation of Noble Metals

Platinum thin films with varying thicknesses were tested for oxygen reduction and evolution performance compared to bulk platinum. Figure 6.1 presents cyclic voltammograms (CVs) of the four samples, all taken at a rotating disc electrode speed of 1600 RPM.

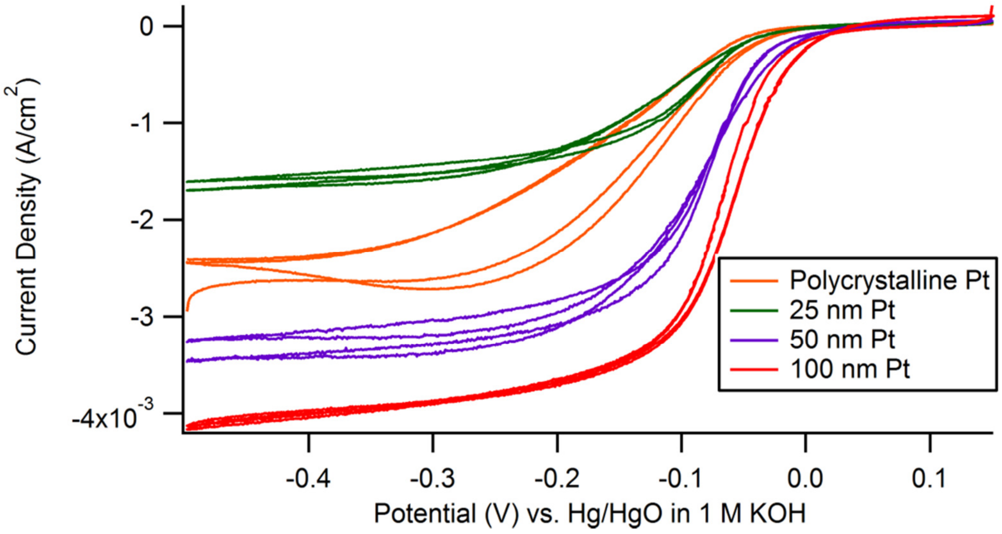

Figure 6.1: Oxygen reduction reactions of thin film platinum compared to bulk.

For oxygen reduction reactions, performance is characterized by the magnitude of the limiting current, which with the sign convention of the test cell, is negative. It appears that the 100 nm thick platinum thin film has the best performance, followed by the 50 nm thick platinum film, while the 25 nm film is similar to the polycrystalline sample. One possible reason for the favorable performance of thin films is that sputtering causes favorable growth of certain crystalline orientations that lead to higher activity. The particular crystalline structure of the specimen is yet undetermined, but can be characterized with x-ray diffraction. Similarly, all three thin films show enhanced performance in the oxygen evolution regime compared to the polycrystalline platinum. For oxygen evolution, performance is measured by the potential at which the curve begins to rise exponentially. As Figure 6.2 shows, the 100 nm platinum film begins to rise well before the other films do.

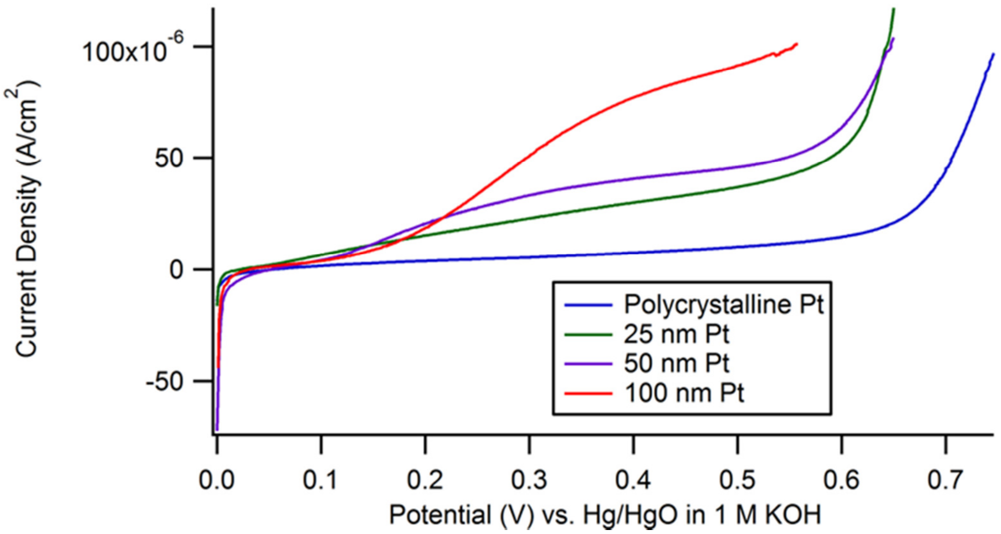

Figure 6.2: Oxygen evolution reactions of thin film platinum compared to bulk.

These results show that sputtered thin films of platinum can be viable catalysts for bifunctional electrodes, and films as thin as 100 nm can show strong catalytic behavior. Furthermore, due to favorable crystal growth, these thin films are superior to bulk platinum. However, a limitation of these thin films is their degradation over time, especially after use as oxygen evolution catalysts. In Figure 6.3, the ORR behavior of the 100 nm thin film platinum electrode is compared from its first use as an ORR catalyst to its behavior after a full sequence of ORR and OER experiments were performed.

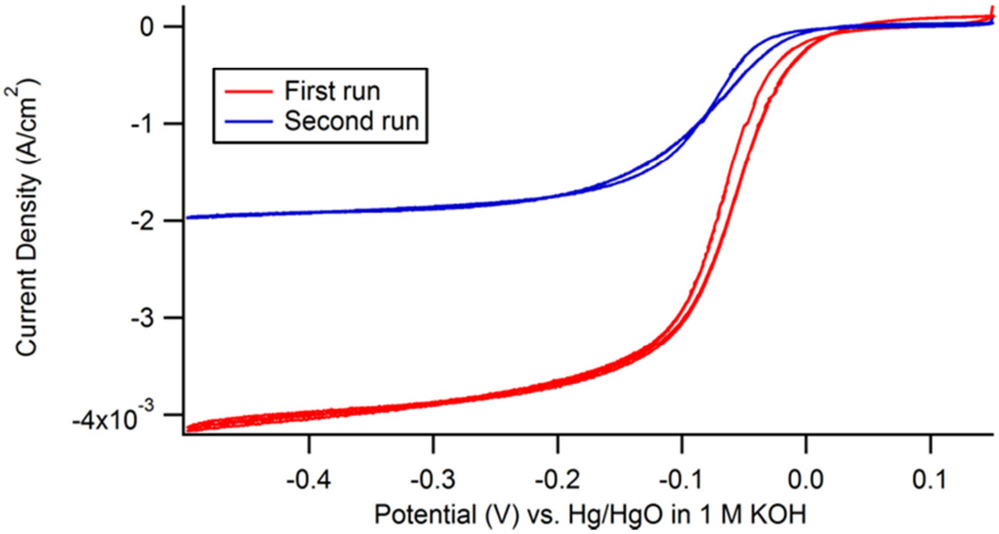

Figure 6.3: Oxygen reduction reaction curves for 100 nm thick platinum film, comparing initial behavior to behavior after ORR and OER experiments.

It is apparent that the electrode undergoes degradation over time and after use. This is a phenomenon that does not readily appear in polycrystalline platinum, and is a major drawback to the use of thin films in metal-air batteries.

Another noble metal system studied was a platinum ruthenium alloy. In Figure 6.4, the ORR performance of thin film PtRu is compared against polycrystalline platinum, with all measurements taken at a rotating speed of 1600 RPM.

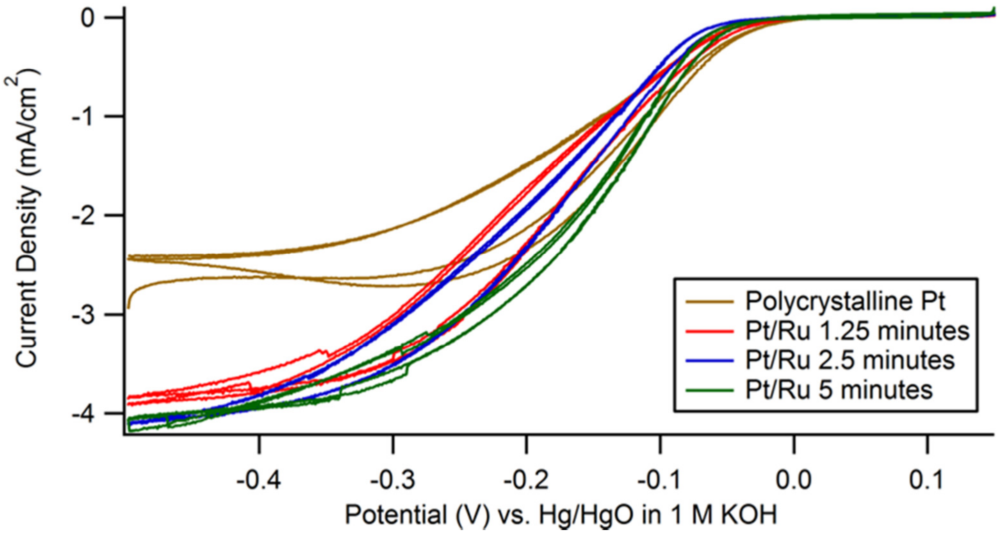

Figure 6.4: Oxygen reduction behavior of Pt/Ru alloy compared to polycrystalline platinum

Unlike thin film platinum, the thickness of the PtRu film does not affect its oxygen reduction performance. This is promising, indicating that very small amounts of this material can be used, reducing the overall cost. However, this is not the case for the oxygen evolution reaction, as shown in Figure 6.5, where thicker PtRu films have better oxygen evolution performance as compared to thinner films.

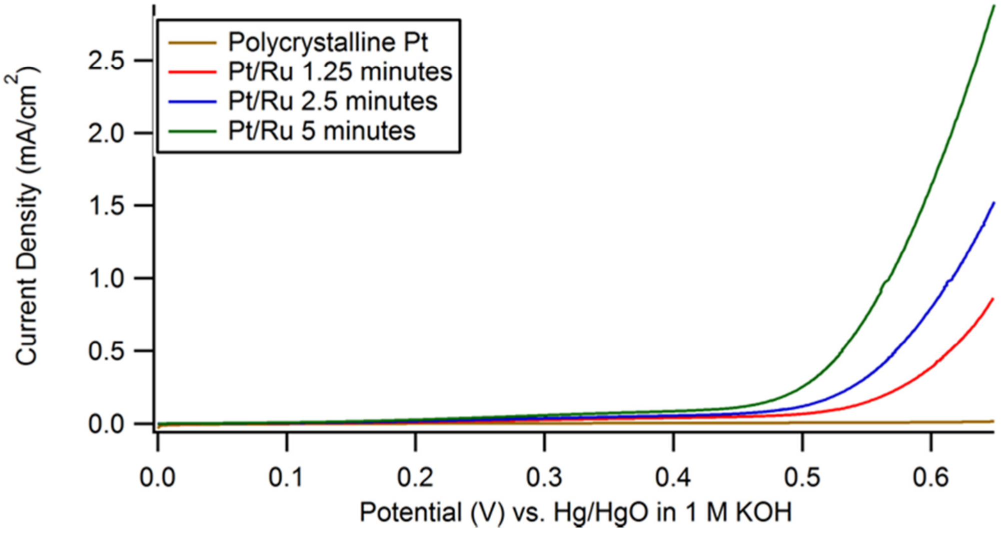

Figure 6.5: Oxygen evolution behavior of PtRu thin films compared to bulk platinum

From these results, it appears that platinum ruthenium alloys are strong candidates for bifunctional air catalysts, but that higher loadings are necessary for facilitating oxygen evolution reactions, which increases the cost of the overall system.

6.4.2 Evaluation of nickel cobalt oxides

In addition to investigating thin layers of expensive metals such as platinum, another branch of study was the pursuit of less expensive catalytic materials, focusing on sputtered spinel nickel cobalt oxide. It was hypothesized that altering the ratio of oxygen to argon in the sputtering environment can affect the crystal structure of the sputtered material and therefore the performance. In Figure 6.6, the different nickel cobalt oxide thin films are compared to polycrystalline platinum.

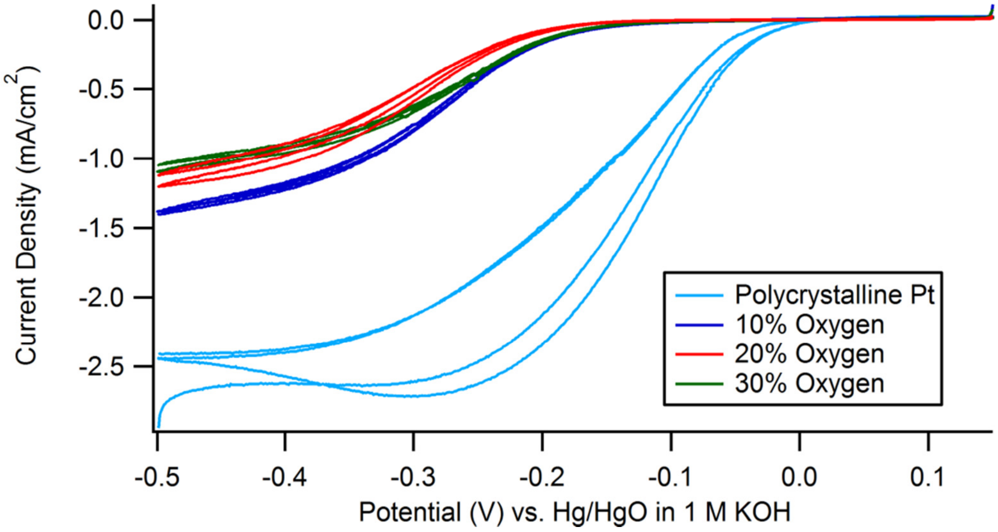

Figure 6.6: Oxygen reduction reaction behavior of sputtered nickel cobalt oxides, compared to polycrystalline Pt

The three thin films appear to have little variation, and all show poorer performance in oxygen reduction compared to polycrystalline platinum. The nickel cobalt oxide spinels are, however, within the same order of magnitude. On the oxygen evolution side, the performance of the nickel spinel oxides is much superior to that of polycrystalline platinum, as shown in Figure 6.7.

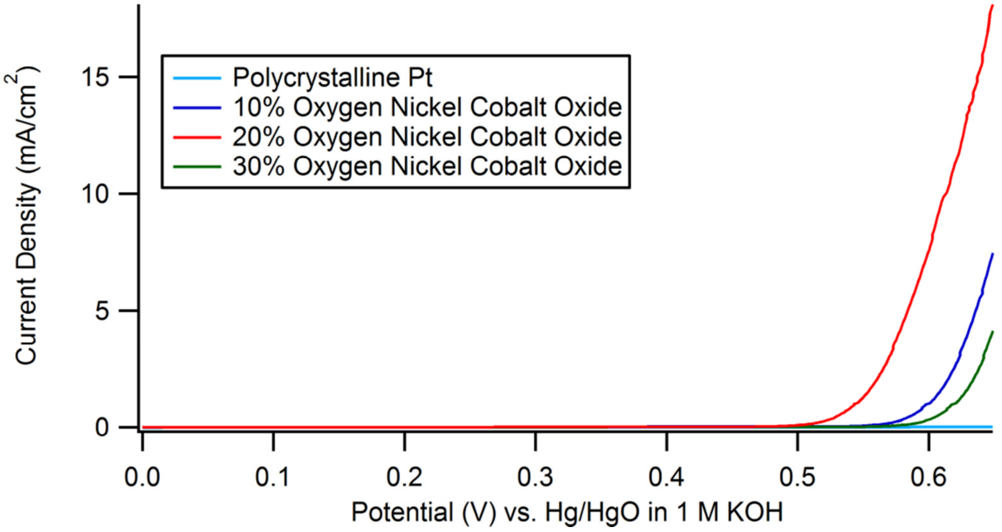

Figure 6.7: Performance of sputtered nickel cobalt oxides compared to polycrystalline platinum in oxygen evolution

Furthermore, in oxygen evolution experiments, there are more significant variations in performance among the three thin films, indicating that changing the sputtering environment does have an effect on the resulting performance. These results suggest that nickel cobalt oxide can be a lower cost alternative to noble metals for metal-air batteries, but that improvements would need to be made on the oxygen reduction side for realistic adoption.

6.5 Summary

This chapter covers some of the work performed over three internships at the Jet Propulsion Laboratory. All of the projects worked on involved metal-air battery technology, specifically iron-air and metal-hydride air batteries. For both of these systems, and other metal-air batteries in general, the theoretical energy densities cannot be realized without the development of a fully bifunctional air cathode. In this research project, thin coatings of noble metals were deposited via sputtering in order to determine if thin films exhibited sufficient catalytic activity compared to bulk. Evaluation of thin platinum films via rotating disc electrode experiments showed that coatings of 100 nm were superior to that of bulk platinum. Similarly, thin films of platinum ruthenium alloys were also strong electrocatalysts in both the oxygen evolution and oxygen reduction regimes. Alternatively, nickel cobalt oxide spinels were tested as lower-cost alternatives to the noble metal catalysts. These performed poorly in oxygen reduction mode, but were strong oxygen evolution catalysts. These materials have potential as bifunctional catalysts, but modifications would need to be made for wide-spread adoption.

7 Conclusions and Future Work

7.1 Conclusions

The work presented in this dissertation on nanoscale research into energy storage systems has encompassed synthesis and characterization. In Chapter 2, the initial research on fabricating nanostructured electrode materials for lithium ion batteries was discussed. Two different lithium iron phosphate ($LiFePO_4$) solutions were formulated for processing into electrospun fibers. Because the precursor solutions contain organic compounds, the final annealing steps for the fibers included controlled processes to convert the organic compounds to carbon, introducing conductive coatings within the synthesis process. This technique successfully produced thin porous $LiFePO_4$ fibers, but is limited in practical use by its multi-step, time-intensive, fabrication process.

The characterization portion of the dissertation is introduced in Chapter 3. Electrochemical strain microscopy (ESM) was a recently developed technique to study electromechanical coupling in energy storage materials. However, the measured strain responses are difficult to interpret, as they can have many different underlying mechanisms that contribute to the overall response. Chapter 3 describes a series of experiments that were devised to distinguish among these different mechanisms by measuring the intrinsic phase response, examining differences between linear and quadratic effects, and studying the results from voltage spectroscopy. These experiments can serve as a fundamental starting point in pinning down the underlying mechanism of a material.

In Chapter 4, the techniques of electrochemical strain microscopy are applied to inhomogeneous lithium iron phosphate thin films in order to correlate nanoscale response to morphology and macroscopic electrochemical properties. ESM was applied onto inhomogeneous $LiFePO_4$ films at different states of charge. Using this technique, the lithium ion motion of nanocrystalline $LiFePO_4$ was clearly demonstrated to be higher than that of microcrystalline $LiFePO_4$ within the same sample. Furthermore, by examining activity at different states of charge, it was demonstrated that ESM can probe the concentration of lithium ions by comparing amplitudes. These results were further confirmed using band excitation to probe lithium ion activity, and also examining the difference between first and second harmonic responses. There is a strong second harmonic response on lithium iron phosphate, but that is smaller than the first harmonic. This quadratic effect may be due to electrostatic or electrostrictive effects, or due to quadratic components of Vegard strain, which is predominantly linear. These techniques were also applied to study samarium doped ceria, a solid oxide fuel cell electrolyte, as described in Chapter 5. Responses from ESM on this material were determined to be due to concentration changes of small polarons, electrons and their associated lattice strain. The intrinsic phase of the material was measured, and its activation energy was estimated from amplitude measurements. Both of these results supported the theory that strains measured were the function of concentration changes of small polarons, rather than oxygen vacancies, as previously reported. Relaxation data for doped ceria was also enlightening, showing completely different relaxation behavior at different temperatures, different environmental conditions, and different heating times. These results suggest that the relaxation results are most likely due to the DC biases applied altering concentrations of surface adsorbates and defects.

Chapter 6 covers metal-air battery research performed over three summer internships at the Jet Propulsion Laboratory. Although the actual work performed encompassed a variety of topics, including the fabrication of metal-air batteries, the research discussed here focused on characterizing catalytic materials for the air electrode. The performance of secondary metal-air batteries is highly dependent on a successful bifunctional air catalyst, which has not been yet fully realized. The research described in this chapter characterized platinum and platinum ruthenium thin films using rotating disc electrode measurements as bifunctional catalysts, finding that these thin films perform better than their bulk counterparts. Although the noble metals are expensive, reducing the amount of material used can make them feasible for wide-spread adoption. The other system studied were nickel cobalt oxide thin films, which could be deposited by reactive sputtering. The ratio of oxygen to argon could be altered in the synthesis procedure, forming films with different crystalline morphologies, and had an effect on their catalytic performance. From these results, it appears that there are a few viable bifunctional catalysts possible, but that further work must be done to optimize these structures.

7.2 Future Work

Electrochemical strain microscopy has proven to be an exciting new technique that can examine local ion and electron motion at nanoscale. This technique has been applied to lithium ion battery electrodes and solid oxide fuel cell electrolytes, but has the potential of investigating many more materials beyond that. However, the mechanism behind the observed strain responses of these materials is unclear, and can have many different contributions. The future of this technique depends on the ability to truly separate out these different contributions. In particular, the contributions from electrostatic effects has not been completely analyzed, and experiments would have to be devised to determine how exactly these electrostatic effects affect measured results. Some preliminary work had also been done with voltage spectroscopy, but an unexamined aspect is the quadratic voltage spectroscopy, which is an interesting line of work to pursue. Using quadratic voltage spectroscopy, some of the electrostrictive behavior could be separated out from ferroelectric effects or electrochemical Vegard strain. Furthermore, almost all of the experiments carried out in this dissertation were performed in an open environment, in which the ambient temperature and humidity could not be determined or controlled. For future research into materials where the environmental conditions play a major factor, such as in doped ceria, experiments should be carried out in controlled environments with known temperature and humidity, and possibly in inert gas chambers. The technique of electrochemical strain microscopy is only in its infancy and can be a versatile and fundamental tool for materials characterization in the future.

References

1. Armand, M. and J.M. Tarascon, *Building better batteries.* Nature, 2008. **451**(7179): p. 652-657.

2. Dunn, B., H. Kamath, and J.M. Tarascon, *Electrical Energy Storage for the Grid: A Battery of Choices.* Science, 2011. **334**(6058): p. 928-935.

3. Bito, A. *Overview of the sodium-sulfur battery for the IEEE Stationary Battery Committee*. in *Power Engineering Society General Meeting, 2005. IEEE*. 2005.

4. Yang, B., et al., *Organo-sulfur molecules enable iron-based battery electrodes to meet the challenges of large-scale electrical energy storage.* Energy & Environmental Science, 2014. **7**(8): p. 2753-2763.

5. Khaligh, A. and Z.H. Li, *Battery, Ultracapacitor, Fuel Cell, and Hybrid Energy Storage Systems for Electric, Hybrid Electric, Fuel Cell, and Plug-In Hybrid Electric Vehicles: State of the Art.* Ieee Transactions on Vehicular Technology, 2010. **59**(6): p. 2806-2814.

6. Chalk, S.G. and J.E. Miller, *Key challenges and recent progress in batteries, fuel cells, and hydrogen storage for clean energy systems.* Journal of Power Sources, 2006. **159**(1): p. 73-80.

7. Thackeray, M.M., C. Wolverton, and E.D. Isaacs, *Electrical energy storage for transportation-approaching the limits of, and going beyond, lithium-ion batteries.* Energy & Environmental Science, 2012. **5**(7): p. 7854-7863.

8. Karden, E., et al., *Energy storage devices for future hybrid electric vehicles.* Journal of Power Sources, 2007. **168**(1 SPEC. ISS.): p. 2-11.

9. Scrosati, B., J. Hassoun, and Y.K. Sun, *Lithium-ion batteries. A look into the future.* Energy & Environmental Science, 2011. **4**(9): p. 3287-3295.

10. Snare, C.C. *From Child's Toy to ISS: Flywheels Hold the Power*. Office of Biological and Physical Research, 2003.

11. Ratnakumar, B.V., et al., *Lithium batteries for aerospace applications: 2003 Mars Exploration Rover.* Journal of Power Sources, 2003. **119**: p. 906-910.

12. Smart, M.C., et al., *Lithium-ion batteries for aerospace.* Ieee Aerospace and Electronic Systems Magazine, 2004. **19**(1): p. 18-25.

13. Smart, M.C., et al., *Life verification of large capacity Yardney Li-ion cells and batteries in support of NASA missions.* International Journal of Energy Research, 2010. **34**(2): p. 116-132.

14. Liu, C., et al., *Advanced Materials for Energy Storage.* Advanced Materials, 2010. **22**(8): p. E28-+.

15. Arico, A.S., et al., *Nanostructured materials for advanced energy conversion and storage devices.* Nature Materials, 2005. **4**(5): p. 366-377.

16. Bruce, P.G., B. Scrosati, and J.M. Tarascon, *Nanomaterials for rechargeable lithium batteries.* Angewandte Chemie, International Edition, 2008. **47**(16): p. 2930-2946.

17. Wang, Y. and G.Z. Cao, *Developments in nanostructured cathode materials for high-performance lithium-ion batteries.* Advanced Materials, 2008. **20**(12): p. 2251-2269.

18. Joo, S.H., et al., *Ordered nanoporous arrays of carbon supporting high dispersions of platinum nanoparticles.* Nature, 2001. **412**(6843): p. 169-172.

19. Zhong, C.J., et al., *Nanostructured catalysts in fuel cells.* Nanotechnology, 2010. **21**(6).

20. Chao, C.C., et al., *Improved Solid Oxide Fuel Cell Performance with Nanostructured Electrolytes.* Acs Nano, 2011. **5**(7): p. 5692-5696.

21. Maier, J., *Nanoionics: ion transport and electrochemical storage in confined systems.* Nature Materials, 2005. **4**(11): p. 805-815.

22. Maier, J., *Nanoionics: ionic charge carriers in small systems.* Physical Chemistry Chemical Physics, 2009. **11**(17): p. 3011-3022.

23. Andersson, A.M., et al., *Surface characterization of electrodes from high power lithium-ion batteries.* Journal of the Electrochemical Society, 2002. **149**(10): p. A1358-A1369.

24. Rom, I., et al., *Electron microscopical characterization of Sn/SnSb composite electrodes for lithium-ion batteries.* Solid State Ionics, 2001. **143**(3-4): p. 329-336.

25. Orsini, F., et al., *In situ Scanning Electron Microscopy (SEM) observation of interfaces within plastic lithium batteries.* Journal of Power Sources, 1998. **76**(1): p. 19-29.

26. Chen, D., et al., *In situ scanning electron microscopy on lithium-ion battery electrodes using an ionic liquid.* Journal of Power Sources, 2011. **196**(15): p. 6382-6387.

27. Chen, G., X. Song, and T.J. Richardson, *Electron microscopy study of the LiFePO[sub 4] to FePO[sub 4] phase transition.* Electrochemical and Solid-State Letters, 2006. **9**(6): p. A295-A298.

28. Huang, J.Y., et al., *In Situ Observation of the Electrochemical Lithiation of a Single SnO2 Nanowire Electrode.* Science, 2010. **330**(6010): p. 1515-1520.

29. Liu, X.H. and J.Y. Huang, *In situ TEM electrochemistry of anode materials in lithium ion batteries.* Energy & Environmental Science, 2011. **4**(10): p. 3844-3860.

30. Wang, C.M., et al., *In situ transmission electron microscopy and spectroscopy studies of interfaces in Li ion batteries: Challenges and opportunities.* Journal of Materials Research, 2010. **25**(8): p. 1541-1547.

31. Chen, Z.H., Z.H. Lu, and J.R. Dahn, *Staging phase transitions in LixCoO2.* Journal of the Electrochemical Society, 2002. **149**(12): p. A1604-A1609.

32. Courtney, I.A. and J.R. Dahn, *Electrochemical and in situ x-ray diffraction studies of the reaction of lithium with tin oxide composites.* Journal of the Electrochemical Society, 1997. **144**(6): p. 2045-2052.

33. Beaulieu, L.Y., et al., *A system for performing simultaneous in situ atomic force microscopy/optical microscopy measurements on electrode materials for lithium-ion batteries.* Review of Scientific Instruments, 2001. **72**(8): p. 3313-3319.

34. Beaulieu, L.Y., et al., *Reaction of Li with alloy thin films studied by in situ AFM.* Journal of the Electrochemical Society, 2003. **150**(11): p. A1457-A1464.

35. Beaulieu, L.Y., et al., *Colossal reversible volume changes in lithium alloys.* Electrochemical and Solid-State Letters, 2001. **4**(9): p. A137-A140.

36. Balke, N., et al., *Nanoscale mapping of ion diffusion in a lithium-ion battery cathode.* Nature Nanotechnology, 2010. **5**(10): p. 749-754.

37. Kalinin, S.V. and N. Balke, *Local Electrochemical Functionality in Energy Storage Materials and Devices by Scanning Probe Microscopies: Status and Perspectives.* Advanced Materials, 2010. **22**(35): p. E193-E209.

38. Scrosati, B., *Challenge of portable power.* Nature, 1995. **373**(6515): p. 557-558.

39. Aifantis, K.E., S.A. Hackney, and R.V. Kumar, *High Energy Density Lithium Batteries*2010, Weinheim: Wiley-VCH.

40. Agubra, V.A. and J.W. Fergus, *The formation and stability of the solid electrolyte interface on the graphite anode.* Journal of Power Sources, 2014. **268**: p. 153-162.

41. Verma, P., P. Maire, and P. Novák, *A review of the features and analyses of the solid electrolyte interphase in Li-ion batteries.* Electrochimica Acta, 2010. **55**(22): p. 6332-6341.

42. Scrosati, B. and J. Garche, *Lithium batteries: Status, prospects and future.* Journal of Power Sources, 2010. **195**(9): p. 2419-2430.

43. Xu, K., *Nonaqueous liquid electrolytes for lithium-based rechargeable batteries.* Chemical Reviews, 2004. **104**(10): p. 4303-4417.

44. Zhang, S.S., *A review on electrolyte additives for lithium-ion batteries.* Journal of Power Sources, 2006. **162**(2): p. 1379-1394.

45. Li, W., J.R. Dahn, and D.S. Wainwright, *RECHARGEABLE LITHIUM BATTERIES WITH AQUEOUS-ELECTROLYTES.* Science, 1994. **264**(5162): p. 1115-1118.

46. Luo, J.Y., et al., *Raising the cycling stability of aqueous lithium-ion batteries by eliminating oxygen in the electrolyte.* Nature Chemistry, 2010. **2**(9): p. 760-765.

47. Stephan, A.M., *Review on gel polymer electrolytes for lithium batteries.* European Polymer Journal, 2006. **42**(1): p. 21-42.

48. Song, J.Y., Y.Y. Wang, and C.C. Wan, *Review of gel-type polymer electrolytes for lithium-ion batteries.* Journal of Power Sources, 1999. **77**(2): p. 183-197.

49. Fergus, J.W., *Ceramic and polymeric solid electrolytes for lithium-ion batteries.* Journal of Power Sources, 2010. **195**(15): p. 4554-4569.

50. Quartarone, E. and P. Mustarelli, *Electrolytes for solid-state lithium rechargeable batteries: recent advances and perspectives.* Chemical Society Reviews, 2011. **40**(5): p. 2525-2540.

51. Deng, D., et al., *Green energy storage materials: Nanostructured TiO2 and Sn-based anodes for lithium-ion batteries.* Energy & Environmental Science, 2009. **2**(8): p. 818-837.

52. Su, X., et al., *Advanced titania nanostructures and composites for lithium ion battery.* Journal of Materials Science, 2012. **47**(6): p. 2519-2534.

53. Chen, J.S. and X.W. Lou, *SnO2-Based Nanomaterials: Synthesis and Application in Lithium-Ion Batteries.* Small, 2013. **9**(11): p. 1877-1893.

54. Szczech, J.R. and S. Jin, *Nanostructured silicon for high capacity lithium battery anodes.* Energy & Environmental Science, 2011. **4**(1): p. 56-72.

55. Whittingham, M.S., *Lithium batteries and cathode materials.* Chemical Reviews, 2004. **104**(10): p. 4271-4301.

56. Gummow, R.J., A. Dekock, and M.M. Thackeray, *IMPROVED CAPACITY RETENTION IN RECHARGEABLE 4V LITHIUM LITHIUM MANGANESE OXIDE (SPINEL) CELLS.* Solid State Ionics, 1994. **69**(1): p. 59-67.

57. Kang, K.S., et al., *Electrodes with high power and high capacity for rechargeable lithium batteries.* Science, 2006. **311**(5763): p. 977-980.

58. Wang, Y. and G.Z. Cao, *Synthesis and enhanced intercalation properties of nanostructured vanadium oxides.* Chemistry of Materials, 2006. **18**(12): p. 2787-2804.

59. Chung, S.Y., J.T. Bloking, and Y.M. Chiang, *Electronically conductive phospho-olivines as lithium storage electrodes.* Nature Materials, 2002. **1**(2): p. 123-128.

60. Yuan, L.-X., et al., *Development and challenges of LiFePO4 cathode material for lithium-ion batteries.* Energy & Environmental Science, 2011. **4**(2): p. 269-284.

61. O'Hayre, R., et al., *Fuel Cell Fundamentals*2006, Hoboken, New Jersey: John Wiley & Sons.

62. Ormerod, R.M., *Solid oxide fuel cells.* Chemical Society Reviews, 2003. **32**(1): p. 17-28.

63. Mori, M., et al., *Thermal expansion of nickel-zirconia anodes in solid oxide fuel cells during fabrication and operation.* Journal of the Electrochemical Society, 1998. **145**(4): p. 1374-1381.

64. Goodenough, J.B. and Y.H. Huang, *Alternative anode materials for solid oxide fuel cells.* Journal of Power Sources, 2007. **173**(1): p. 1-10.

65. Sun, C.W. and U. Stimming, *Recent anode advances in solid oxide fuel cells.* Journal of Power Sources, 2007. **171**(2): p. 247-260.

66. Stambouli, A.B. and E. Traversa, *Solid oxide fuel cells (SOFCs): a review of an environmentally clean and efficient source of energy.* Renewable & Sustainable Energy Reviews, 2002. **6**(5): p. 433-455.

67. Adler, S.B., *Factors governing oxygen reduction in solid oxide fuel cell cathodes.* Chemical Reviews, 2004. **104**(10): p. 4791-4843.

68. Fergus, J.W., *Electrolytes for solid oxide fuel cells.* Journal of Power Sources, 2006. **162**(1): p. 30-40.

69. Strickler, D.W. and W.G. Carlson, *Ionic Conductivity of Cubic Solid Solutions in the System CaO—Y2O3—ZrO2.* Journal of the American Ceramic Society, 1964. **47**(3): p. 122-127.

70. Dixon, J.M., et al., *ELECTRICAL RESISTIVITY OF STABILIZED ZIRCONIA AT ELEVATED TEMPERATURES.* Journal of the Electrochemical Society, 1963. **110**(4): p. 276-280.

71. Nomura, K., et al., *Aging and Raman scattering study of scandia and yttria doped zirconia.* Solid State Ionics, 2000. **132**(3-4): p. 235-239.

72. Yamamoto, O., et al., *ELECTRICAL-CONDUCTIVITY OF STABILIZED ZIRCONIA WITH YTTERBIA AND SCANDIA.* Solid State Ionics, 1995. **79**: p. 137-142.

73. Brandon, N.P., S. Skinner, and B.C.H. Steele, *Recent advances in materials for fuel cells.* Annual Review of Materials Research, 2003. **33**: p. 183-213.

74. Steele, B.C.H. and A. Heinzel, *Materials for fuel-cell technologies.* Nature, 2001. **414**(6861): p. 345-352.

75. Tschope, A., J.Y. Ying, and H.L. Tuller, *Catalytic redox activity and electrical conductivity of nanocrystalline non-stoichiometric cerium oxide.* Sensors and Actuators B-Chemical, 1996. **31**(1-2): p. 111-114.

76. Bonnell, D.A., et al., *Piezoresponse Force Microscopy: A Window into Electromechanical Behavior at the Nanoscale.* Mrs Bulletin, 2009. **34**(9): p. 648-657.

77. Gruverman, A. and S.V. Kalinin, *Piezoresponse force microscopy and recent advances in nanoscale studies of ferroelectrics.* Journal of Materials Science, 2006. **41**(1): p. 107-116.

78. Kalinin, S.V., A. Rar, and S. Jesse, *A decade of piezoresponse force microscopy: Progress, challenges, and opportunities.* Ieee Transactions on Ultrasonics Ferroelectrics and Frequency Control, 2006. **53**(12): p. 2226-2252.

79. Kim, M.G. and J. Cho, *Reversible and High-Capacity Nanostructured Electrode Materials for Li-Ion Batteries.* Advanced Functional Materials, 2009. **19**(10): p. 1497-1514.

80. Guo, Y.G., J.S. Hu, and L.J. Wan, *Nanostructured materials for electrochemical energy conversion and storage devices.* Advanced Materials, 2008. **20**(15): p. 2878-2887.

81. Okubo, M., et al., *Nanosize effect on high-rate Li-ion intercalation in LiCoO2 electrode.* Journal of the American Chemical Society, 2007. **129**(23): p. 7444-7452.

82. Delacourt, C., et al., *Size effects on carbon-free LiFePO4 powders.* Electrochemical and Solid-State Letters, 2006. **9**(7): p. A352-A355.

83. Franger, S., et al., *LiFePO[sub 4] Synthesis Routes for Enhanced Electrochemical Performance.* Electrochemical and Solid-State Letters, 2002. **5**(10): p. A231-A233.

84. Jansen, A.N., et al., *Development of a high-power lithium-ion battery.* Journal of Power Sources, 1999. **81**: p. 902-905.

85. Wang, Y.G., P. He, and H.S. Zhou, *Olivine LiFePO(4): development and future.* Energy & Environmental Science, 2011. **4**(3): p. 805-817.

86. Padhi, A.K., K.S. Nanjundaswamy, and J.B. Goodenough, *Phospho-olivines as positive-electrode materials for rechargeable lithium batteries.* Journal of the Electrochemical Society, 1997. **144**(4): p. 1188-1194.

87. Zhang, W.J., *Structure and performance of LiFePO4 cathode materials: A review.* Journal of Power Sources, 2011. **196**(6): p. 2962-2970.

88. Andersson, A.S., et al., *Thermal Stability of LiFePO[sub 4]-Based Cathodes.* Electrochemical and Solid-State Letters, 2000. **3**(2): p. 66-68.

89. Wang, J. and X. Sun, *Understanding and recent development of carbon coating on LiFePO4 cathode materials for lithium-ion batteries.* Energy & Environmental Science, 2012. **5**(1): p. 5163-5185.

90. Toprakci, O., et al., *Fabrication and electrochemical characteristics of electrospun LiFePO4/carbon composite fibers for lithium-ion batteries.* Journal of Power Sources, 2011. **196**(18): p. 7692-7699.

91. Li, D., J.T. McCann, and Y.N. Xia, *Electrospinning: A simple and versatile technique for producing ceramic nanofibers and nanotubes.* Journal of the American Ceramic Society, 2006. **89**(6): p. 1861-1869.

92. Li, D. and Y.N. Xia, *Electrospinning of nanofibers: Reinventing the wheel?* Advanced Materials, 2004. **16**(14): p. 1151-1170.

93. Miao, J.J., et al., *Electrospinning of Nanomaterials and Applications in Electronic Components and Devices.* Journal of Nanoscience and Nanotechnology, 2010. **10**(9): p. 5507-5519.

94. Yu, D.M., et al., *Mesoporous vanadium pentoxide nanofibers with significantly enhanced Li-ion storage properties by electrospinning.* Energy & Environmental Science, 2011. **4**(3): p. 858-861.

95. Kim, C., et al., *Fabrication of electrospinning-derived carbon nanofiber webs for the anode material of lithium-ion secondary batteries.* Advanced Functional Materials, 2006. **16**(18): p. 2393-2397.

96. Gong, X., et al., *Application of Electrospinning Technique in Power Lithium-Ion Batteries.* Progress in Chemistry, 2014. **26**(1): p. 41-47.

97. Wang, C., et al., *How to manipulate the electrospinning jet with controlled properties to obtain uniform fibers with the smallest diameter?-a brief discussion of solution electrospinning process.* Journal of Polymer Research, 2011. **18**(1): p. 111-123.

98. Wang, P.Q., et al., *Mesoporous carbon nanofibers with a high surface area electrospun from thermoplastic polyvinylpyrrolidone.* Nanoscale, 2012. **4**(22): p. 7199-7204.

99. Liu, Y., et al., *Lithium iron phosphate/carbon nanocomposite film cathodes for high energy lithium ion batteries.* Electrochimica Acta, 2011. **56**(5): p. 2559-2565.

100. Lin, L., et al., *X-ray diffraction study of LiFePO4 synthesized by hydrothermal method.* Rsc Advances, 2013. **3**(34): p. 14652-14660.

101. Kalinin, S.V. and D.A. Bonnell, *Imaging mechanism of piezoresponse force microscopy of ferroelectric surfaces.* Physical Review B, 2002. **65**(12).

102. Uchino, K., *Ferroelectric Devices*2000, Basel, Switzerland: Marcel Dekker, Inc.

103. Balke, N., et al., *Decoupling electrochemical reaction and diffusion processes in ionically-conductive solids on the nanometer scale.* Acs Nano, 2010. **4**(12): p. 7349-7357.

104. Balke, N., et al., *Real space mapping of Li-ion transport in amorphous Si anodes with nanometer resolution.* Nano Letters, 2010. **10**(9): p. 3420-3425.

105. Kumar, A., et al., *Measuring oxygen reduction/evolution reactions on the nanoscale.* Nature Chemistry, 2011. **3**(9): p. 707-713.

106. Arruda, T.M., et al., *Mapping Irreversible Electrochemical Processes on the Nanoscale: Ionic Phenomena in Li Ion Conductive Glass Ceramics.* Nano Letters, 2011. **11**(10): p. 4161-4167.

107. Kumar, A., et al., *Variable temperature electrochemical strain microscopy of Sm-doped ceria.* Nanotechnology, 2013. **24**(14).

108. Proksch, R., *Electrochemical Strain Microscopy of Silica Glasses.* arXiv:1312.6933, 2013.

109. Sekhon, J.S., L. Aggarwal, and G. Sheet, *Voltage induced local hysteretic phase switching in silicon.* Applied Physics Letters, 2014. **104**(16).

110. Jesse, S., B. Mirman, and S.V. Kalinin, *Resonance enhancement in piezoresponse force microscopy: Mapping electromechanical activity, contact stiffness, and Q factor.* Applied Physics Letters, 2006. **89**(2).

111. Rodriguez, B.J., et al., *Dual-frequency resonance-tracking atomic force microscopy.* Nanotechnology, 2007. **18**(47).

112. Gannepalli, A., et al., *Mapping nanoscale elasticity and dissipation using dual frequency contact resonance AFM (vol 22, 355705, 2011).* Nanotechnology, 2013. **24**(15).

113. Jesse, S. and S.V. Kalinin, *Band excitation in scanning probe microscopy: sines of change.* Journal of Physics D-Applied Physics, 2011. **44**(46).

114. Jesse, S., et al., *The band excitation method in scanning probe microscopy for rapid mapping of energy dissipation on the nanoscale.* Nanotechnology, 2007. **18**(43).

115. Scofield, J.H., *FREQUENCY-DOMAIN DESCRIPTION OF A LOCK-IN AMPLIFIER.* American Journal of Physics, 1994. **62**(2): p. 129-133.

116. Liu, Y., et al., *Thermal variation of piezoresponse in microscopically poled poly(vinylidene fluoride-trifluoroethylene) ferroelectric copolymers approaching Curie temperature.* Journal of Applied Physics, 2011. **110**(5): p. -.

117. Xie, S.H., et al., *Multiferroic CoFe2O4-Pb(Zr0.52Ti0.48)O-3 core-shell nanofibers and their magnetoelectric coupling.* Nanoscale, 2011. **3**(8): p. 3152-3158.

118. Heywang, W., K. Lubitz, and W. Wersing, *Piezoelectricity: Evolution and Future of a Technology*2008: Springer Science & Business Media.

119. Wagner, R., A. Raman, and R. Proksch, *Spatial spectrograms of vibrating atomic force microscopy cantilevers coupled to sample surfaces.* Applied Physics Letters, 2013. **103**(26).

120. Proksch, R., *In-situ Piezoresponse Force Microscopy Cantilever Shape Profiling.* arXiv:1409.0133, 2014.

121. Newnham, R.E., et al., *Electrostriction: Nonlinear electromechanical coupling in solid dielectrics.* Journal of Physical Chemistry B, 1997. **101**(48): p. 10141-10150.

122. Seeger, K. and W. Maurer, *Nonlinear electronic transport in TTF-TCNQ observed by microwave harmonic mixing.* Solid State Communications, 1978. **27**(5): p. 603-606.

123. Vasudevan, R.K., et al., *Higher order harmonic detection for exploring nonlinear interactions with nanoscale resolution.* Scientific Reports, 2013. **3**.

124. Kim, Y., et al., *Nonlinear Phenomena in Multiferroic Nanocapacitors: Joule Heating and Electromechanical Effects.* Acs Nano, 2011. **5**(11): p. 9104-9112.

125. Liu, Y., et al., *Biological Ferroelectricity Uncovered in Aortic Walls by Piezoresponse Force Microscopy.* Physical Review Letters, 2012. **108**(7): p. 078103.

126. Liu, Y., et al., *Engineering nanostructured electrodes away from equilibrium for lithium-ion batteries.* Journal of Materials Chemistry, 2011. **21**(27): p. 9969-9983.

127. Takahashi, M., et al., *Characterization of LiFePO4 as the cathode material for rechargeable lithium batteries.* Journal of Power Sources, 2001. **97-98**: p. 508-511.

128. Andersson, A.S. and J.O. Thomas, *The source of first-cycle capacity loss in LiFePO4.* Journal of Power Sources, 2001. **97-8**: p. 498-502.

129. Newman, J.S., *Electrochemical Systems*1991, Englewood Cliffs, NJ: Prentice Hall.

130. Steele, B.C.H., *Materials for IT-SOFC stacks 35 years R&D: the inevitability of gradualness?* Solid State Ionics, 2000. **134**(1-2): p. 3-20.

131. Dalslet, B., et al., *Assessment of doped ceria as electrolyte.* Journal of Solid State Electrochemistry, 2006. **10**(8): p. 547-561.

132. Sahibzada, M., et al., *Development of solid oxide fuel cells based on a Ce(Gd)O2-x electrolyte film for intermediate temperature operation.* Catalysis Today, 1997. **38**(4): p. 459-466.

133. Zha, S.W., C.R. Xia, and G.Y. Meng, *Effect of Gd (Sm) doping on properties of ceria electrolyte for solid oxide fuel cells.* Journal of Power Sources, 2003. **115**(1): p. 44-48.

134. Inaba, H. and H. Tagawa, *Ceria-based solid electrolytes - Review.* Solid State Ionics, 1996. **83**(1-2): p. 1-16.

135. Mogensen, M., N.M. Sammes, and G.A. Tompsett, *Physical, chemical and electrochemical properties of pure and doped ceria.* Solid State Ionics, 2000. **129**(1-4): p. 63-94.

136. Tschope, A., *Grain size-dependent electrical conductivity of polycrystalline cerium oxide II: Space charge model.* Solid State Ionics, 2001. **139**(3-4): p. 267-280.

137. Chiang, Y.M., E.B. Lavik, and D.A. Blom, *Defect thermodynamics and electrical properties of nanocrystalline oxides: Pure and doped CeO2.* Nanostructured Materials, 1997. **9**(1-8): p. 633-642.

138. Tuller, H.L., *Ionic conduction in nanocrystalline materials.* Solid State Ionics, 2000. **131**(1-2): p. 143-157.

139. Lu, Y., *Study of electrochemical performance of strontium doped lanthanum coablt oxides using electrochemical impedance spectroscopy and microelectrode array cell design*, in *Chemical Engineering*2007, University of Washington. p. 182.

140. Doria, S., et al., *Nanoscale mapping of oxygen vacancy kinetics in nanocrystalline Samarium doped ceria thin films.* Applied Physics Letters, 2013. **103**(17): p. -.

141. Marrocchelli, D., et al., *Understanding Chemical Expansion in Non-Stoichiometric Oxides: Ceria and Zirconia Case Studies.* Advanced Functional Materials, 2012. **22**(9): p. 1958-1965.

142. Chen, Q.N., S.B. Adler, and J. Li, *Imaging space charge regions in Sm-doped ceria using electrochemical strain microscopy.* Applied Physics Letters, 2014. **105**(In Press).

143. Tuller, H.L. and A.S. Nowick, *SMALL POLARON ELECTRON-TRANSPORT IN REDUCED CEO2 SINGLE-CRYSTALS.* Journal of Physics and Chemistry of Solids, 1977. **38**(8): p. 859-867.

144. Hamann, C.H., A. Hamnett, and W. Vielstich, *Electrochemistry*2007, Weinheim: Wiley-VCH.

145. Blurton, K.F. and A.F. Sammells, *Metal/air batteries: Their status and potential — a review.* Journal of Power Sources, 1979. **4**(4): p. 263-279.

146. Rahman, M.A., X.J. Wang, and C.E. Wen, *High Energy Density Metal-Air Batteries: A Review.* Journal of the Electrochemical Society, 2013. **160**(10): p. A1759-A1771.

147. Cheng, F.Y. and J. Chen, *Metal-air batteries: from oxygen reduction electrochemistry to cathode catalysts.* Chemical Society Reviews, 2012. **41**(6): p. 2172-2192.

148. Wadia, C., P. Albertus, and V. Srinivasan, *Resource constraints on the battery energy storage potential for grid and transportation applications.* Journal of Power Sources, 2011. **196**(3): p. 1593-1598.

149. Narayanan, S.R., et al., *Materials challenges and technical approaches for realizing inexpensive and robust iron-air batteries for large-scale energy storage.* Solid State Ionics, 2012. **216**: p. 105-109.

150. Chartouni, D., et al., *Air-metal hydride secondary battery with long cycle life.* Journal of Alloys and Compounds, 2002. **330**: p. 766-770.

151. Sakai, T., et al., *Air-metal hydride battery construction and evaluation.* Journal of the Electrochemical Society, 1995. **142**(12): p. 4040-4045.

152. Jorissen, L., *Bifunctional oxygen/air electrodes.* Journal of Power Sources, 2006. **155**(1): p. 23-32.

153. Reier, T., M. Oezaslan, and P. Strasser, *Electrocatalytic Oxygen Evolution Reaction (OER) on Ru, Ir, and Pt Catalysts: A Comparative Study of Nanoparticles and Bulk Materials.* ACS Catalysis, 2012. **2**(8): p. 1765-1772.

154. Vielstich, W., A. Lamm, and H.A. Gasteiger, *Handbook of Fuel Cells*. Vol. 2. 2003, England: John Wiley & Sons Ltd.

155. Muller, S., K. Striebel, and O. Haas, *LA0.6CA0.4COO3 - A STABLE AND POWERFUL CATALYST FOR BIFUNCTIONAL AIR ELECTRODES.* Electrochimica Acta, 1994. **39**(11-12): p. 1661-1668.

156. Weidenkaff, A., S.G. Ebbinghaus, and T. Lippert, *Ln(1-x)A(x)CoO(3) (Ln = Er, La; A = Ca, Sr)/carbon nanotube composite materials applied for rechargeable Zn/air batteries.* Chemistry of Materials, 2002. **14**(4): p. 1797-1805.

157. Malkhandi, S., et al., *Electrocatalytic Activity of Transition Metal Oxide-Carbon Composites for Oxygen Reduction in Alkaline Batteries and Fuel Cells.* Journal of the Electrochemical Society, 2013. **160**(9): p. F943-F952.

158. Maass, S., et al., *Carbon support oxidation in PEM fuel cell cathodes.* Journal of Power Sources, 2008. **176**(2): p. 444-451.

159. Cao, G. and Y. Wang, *Nanostructures and Nanomaterials: Synthesis, Properties, and Applications*. 2nd ed2011, Singapore: Wolrd Scientific Publishing Co. Pte. Ltd.

160. Bard, A.J. and L.R. Faulkner, *Electrochemical Methods*2001, New Jersey: John Wiley & Sons.

VITA

Education

University of Washington, Seattle
Ph.D. Mechanical Engineering, 2014

University of California, Los Angeles
M.S. Mechanical Engineering, 2010

University of California, Los Angeles
B.S. Mechanical Engineering, 2008

Experience

University of Washington, Multifunctional Materials Laboratory 9/2010 – 12/2014
Graduate Student Researcher

- Electrospun nanofibers for lithium ion battery electrodes, assembled electrodes into coin-cell batteries for testing, and fully characterized the material properties of the fibers along with the electrochemical properties of the batteries.
- Analyzed inhomogeneous lithium ion electrode thin films and solid oxide fuel cell electrolytes by electrochemical strain microscopy, a scanning probe microscopy technique involving bias-induced strain measurements at varying temperatures.
- Developed experimental procedures for determining the mechanisms of electrochemical coupling in strain-based scanning probe microscopy for dielectric, electrochemical, and ferroelectric materials.
- Created custom measurement techniques and data analysis algorithms for the scanning probe microscope using MATLAB and IGOR Pro.

Jet Propulsion Laboratory Summers 2012-2014
Space Technology Research Intern

- Participated in multiple metal-air battery projects, focusing on material processing and electrochemical testing.
- Fabricated nanostructured whiskers by thermal evaporation, and subsequently deposited catalytic material by reactive sputtering.
- Characterized noble metals and mixed oxides for air catalysts using a rotating disc electrode set-up.
- Assembled and performed electrochemical testing on full metal-air battery.

University of California, Los Angeles, Multifunctional Composites Laboratory
9/2008 – 6/2010
Graduate Research Assistant

- Performed stress analysis on thin film silicon solar cells adhered to carbon fiber composite structures.
- Sintered titanium dioxide nanoparticles using intense pulsed light for flexible dye-sensitized solar cells, and characterized the assembled cell.

Schlumberger **6-9/2008**

Mechanical Engineering Intern

- Designed and implemented improvements in the heat transfer within a calibration module for a surveying tool.

Applied Operations Research Inc. 6-9/ 2007

Summer Intern

- Wrote MATLAB and Unix Shell scripts to execute and analyze Navy transmission loss software for ocean bottom characterization.

University of California, Los Angeles, Heat Transfer Laboratory **12/2006 – 6/2007**

Undergraduate Lab Assistant

- Tested thermal conductivity of printed circuit boards for Teradyne, Inc, and calibrated the thermal conductivity measurement system.

Honors

NASA Space Technology Research Fellowship	2011-2014
UCLA Materials Creation Training Fellowship	2009-2010
UCLA Mechanical Engineering Fellowship	2008-2009
Tau Beta Pi	2007
UCLA Regents Scholarship	2004-2008

Publications

- *Q.N. Chen*, S. Adler, and J.Y. Li, “Imaging space charge regions in ceria using electrochemical strain microscopy.” *Accepted*, Applied Physics Letters.
- *Q.N. Chen*, Y. Ou, F.Y. Ma, and J.Y. Li, “Mechanisms of electrochemical coupling in strain based scanning probe microscopy.” Applied Physics Letters, 2014
- *Q.N. Chen*, Y.Y. Liu, Y.M. Liu, S.H. Xie, G.Z. Cao, and J.Y. Li, “Delineating local electromigration for nanoscale probing of lithium ion intercalation and extraction by electrochemical strain microscopy.” Applied Physics Letters, 2012.
- *Q.N. Chen*, F.Y. Ma, S.H. Xie, Y.M. Liu, R. Proksch, and J.Y. Li, “High sensitivity piezomagnetic force microscopy for quantitative probing of magnetic materials at the Nanoscale.” Nanoscale, 2013.
- Y.M. Liu, H.L. Cai, M. Zelisko, Y.J. Wang, J.L. Sun, F. Yan, F.Y. Ma, P.Q. Wang, *Q.N. Chen*, H.R. Zheng, X.J. Meng, P. Sharma, Y.H. Zhang, and J.Y. Li, “Ferroelastic switching of elastin.” Proceedings of the National Academy of Sciences of the United States of America, 2014.
- Y.M. Liu, Y.J. Wang, M.J. Chow, *Q.N. Chen*, F.Y. Ma, Y.H. Zhang, and J.Y. Li, “Glucose suppressed biological ferroelectricity in aortic elastin.” Physical Review Letters, 2013.
- P.Q. Wang, D. Zhang, F.Y. Ma, Y. Ou, *Q.N. Chen*, S.H. Xie, and J.Y. Li, “Mesoporous carbon nanofibers with a high surface area electrospun from thermoplastic polyvinylpyrrolidone.” Nanoscale, 2012.
- Y.M. Liu, Y.H. Zhang, M.J. Chow, *Q.N. Chen*, and J.Y. Li, “Biological ferroelectricity uncovered in aortic walls by piezoresponse force microscopy.” Physical Review Letters, 2012.

- S.H. Xie, A. Gannepalli, *Q.N. Chen*, Y.M Liu, Y.C. Zhou, R. Proksch, and J.Y. Li, "High resolution quantitative piezoresponse force microscopy of BiFeO3 nanofibers with dramatically enhanced sensitivity." Nanoscale, 2012